Doctoral Dissertation

Study on electromagnetic-wave control in conductive periodic structures and its applications for devices

Go Itami

Department of Electronic Systems Engineering,

The University of Shiga Prefecture

Supervisor: Professor Osamu Sakai

November 2019

Contents

Chapter 1

Introduction

1.1 Basic Theorem and Technologies in Electromagnetics

1.1.1 Electromagnetic theory and metamaterial

Electromagnetic waves are the waves with spatial oscillations of electric fields and magnetic fields reciprocally. The two fields have different physical features each other and by using them based on the core technologies of electric and electronic circuits and photonics, various electromagnetic applications such as communication technology, sensing/imaging methods, electric power transmission systems, and computers, have been created for several decades. It goes without saying that these applications are essential for our daily life.

The basis which supports the various applications is an electromagnetic control theory. Therefore, considering the scientific features of electromagnetic waves, constructing optimal theoretical models for each use case is required for the creation of valuable electromagnetic applications. The waves have various types of propagation modes, and the modes are determined by the electric and magnetic responses of the targeted media and the boundary conditions. In general, when constructing the propagation models theoretically, the ratio between the scale of targeted spaces and the wavelength is considered. If plane waves are assumed, the waves are described as a wave vector whose components are the sinusoidal waves with a specific amplitude and the phase which is a function of the wavenumber and the angular frequency. That is, the waves are expressed as the

3D-oscillation condition that the electric field, magnetic field, and the wave vectors are orthogonal to each other.

When the wavelength is much smaller than the scale of the targeted space, the waves are considered to "propagate" and we generally treat the condition as far fields. Here, the propagation model is expressed theoretically using the phenomena such as transmission, reflection, and refraction. Thus, the behaviors of the waves are determined by the electric constants such as permittivity and permeability of the propagating space and the targeted media. Thus, the wave characteristics can be obtained by solving the wave equations including the boundary conditions. This theoretical model is often applied to the propagating waves with a relatively short wavelength in a range from microwaves to optical waves. And for example, the propagation model is essential for the theoretical discussion in wireless communication environments and design of optical lens [1–4]. And such waves with the high frequency are often used as a signal carrier since they propagate easily and have the potential of having a large amount of information. On the other hand, when the wavelength is much larger than the scale of the targeted space, the waves are considered to be "localized" and we generally treat the condition as near fields. In this time, for example, the electromagnetic behaviors are expressed as equivalent circuits with lumped elements such as an inductor and a capacitor, using impedances that indicate the amplitude ratio between a voltage and a current at a specific point [5, 6]. Therefore, the characteristic-value of the fields can be obtained by solving the equation of the lumped elements. The theoretical model is often used for the waves with a relatively long wavelength in a range from kHz waves to MHz waves and is essential for the applications such as a design of a power supply and a power generator [7, 8]. The waves of the frequency band are often used as power since they can be outputted easily and transmitted with low losses.

However, a subwavelength region which is in a range between near field and far field is attracted in recent years, and novel physical phenomena are discovered and their potentials of industrial applications are being pioneered in the region.

Studies about artificial media with peculiar electromagnetic features that cannot be reconstructed by using natural materials, in subwavelength regions, have been re-

ported. These media can be realized by a periodic arrangement of a unit cell composed of conductive or dielectric subwavelength structures and they are generally called "metamaterials" [9–11].

From a theoretical point of view, treating a unit cell in the media as a microscopic resonator, the equivalent circuit of the unit cell is tuned by controlling structural parameters of the unit cell to resonate at optimal frequencies. Here, the electromagnetic features of the periodic structure as a macroscopic artificial media can be controlled by the lumped parameters of the equivalent circuit. Therefore, designing the unit cell as a resonator with an equivalent circuit approach in a near field region and treating the periodic structure of the unit cell as a macroscopic medium in a far-field region, its local and global electromagnetic behaviors can be controlled desirably. The functional media have been researched and expected to realize the innovative applications for an artificial lens, a sensing system, and an antenna design in microwave bands [12–14].

For example, in the optical and THz wavebands, the interesting phenomenon that a periodic structure of subwavelength apertures exhibit an extraordinary transmission characteristics (EOT) was confirmed by Ebbesen et al. [15], and it develops the field of plasmonics which has a potential of various plasmonic and photonic applications such as band-pass filters, high sensitive measurement systems, and coherent lasers [16–18].

Also in microwave bands, by using similar techniques, a spatial filter which selects transmitted or reflected waves of only limited frequency bands can be realized and it is called frequency selective surfaces (FSS) [19]. Since FSSs are two-dimensional structures, their electromagnetic profiles are provided as boundaries with frequency responses.Therefore, their frequency responses follow to Babinet's principle which means that the complementary structure shows the inverted transmission characteristics of the original structure, due to the duality of electric and magnetic fields [20–24]. This point is different from the case of the above effective media with a suitable thickness.

FSS has been applied to reflectarrays, radomes, and electromagnetic absorbers [25–27]. And, the studies of using metamaterials as transmission lines or functional media with band-gap effects have been reported. These structures of microwave bands are called electromagnetic band-gap structures (EBG) and also called photonic crystals (PC) in

optical wavebands, and they have been used for electromagnetic absorbers, super directivity antennae, and laser [28–30].

Although these techniques are mainly based on designs of only permittivity-controllable media except for EBG, the fact is known that the medium showing a negative refractive index (NRI) can be realized by controlling permittivity and permeability at the same time [31–33]. The functional media has the potential of applying to perfect lens, invisibility cloaks since they can reverse the propagating direction of refracted waves in them. Metamaterials cannot be used for only resonator-applications but also non-resonating applications by giving them gradations of impedances in each unit cell. For example, this technique realizes a functional reflector that controls the propagation direction of the reflected waves, and it is called "metasurface" as one of metamaterials [34–36]. The classification of metamaterial is shown in Fig. 1.1.

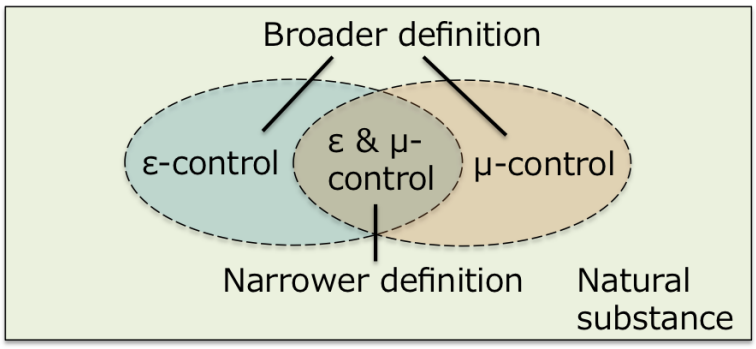

Figure 1.1: The classification of metamaterial.

1.1.2 Surface waves

Electromagnetic waves in far-field region are often described by using the phenomena of transparent and reflection, however in a microscopic view, the waves generate scattered waves at the boundaries and they are synthesized and form the two waves with spatial oscillations by following to Huygens' principle.

For example, assuming that electromagnetic waves are totally reflected at the boundary formed by a prism and air, the fact is known that the near field which has only time oscillations and does not propagate is formed at the boundary. This wave is called an evanescent wave [37, 38] and has a specific dispersion relation different from light lines.

On the other hand, assuming that electromagnetic waves are reflected at the boundary between a conductive surface and air, free electrons on the conductor surface are induced by external electric fields and if the boundary satisfies the specific condition, the free electrons are coupled to external fields and show collective oscillations as compressional waves. The waves are known as "surface plasmon polaritons (SPP)" [39–41]. Since the resonant frequencies of SPPs are varied according to the boundary condition, SPPs are applied to biomedical or chemical sensors that detect existences or contents of specific biologicals or material chemical substances [42, 43]. SPP is one of the surface waves and surface waves include such as a wave propagating on the boundary between plasma and vacuum [44, 45]. Although wave numbers (or phase velocity) of incident waves and spatial oscillations of free electrons must be matched to excite SPP modes, they can not be coupled at normal boundary conditions because the wavenumber of the incident wave in free space and that of free electrons are different. However, when evanescent waves excited by total reflection at a boundary such as between a prism and air are used, the wavenumbers of the incident waves and the oscillations of free electrons can be coupled and SPPs are excited. Therefore, SPPs can be excited only if a specific boundary condition is provided and electromagnetic waves of an optical wave band which has sufficient energy to excite free electron-oscillations.

In recent years, a similar phenomenon is confirmed at lower frequency bands such as terahertz and millimeter-wave bands by using subwavelength conductive periodic structures. This phenomenon is called spoof surface plasmon polariton (SSPP) [46–52], and SSPP is one of metamateirials and has a potential of being applied to a microwave lens, super directivity antennae, and sensing technology in the above frequency bands [12, 29, 53]. In the phenomenon, as well as SPPs, concentrated electric field distributions are collectively oscillated instead of free electrons by being coupled to the optimal incident wave at specific boundary conditions between conductive periodic structures and air. The different point from the case of SPP is the controllability of the resonant frequency, and it can be varied by changing its structural parameters such as the size of holes or cavities, the period of unit cells, and its thickness [54, 55]. The fact indicates that the effective permittivity of the periodic structure can be controlled by changing

its structural parameters, and an SSPP structure has the potential of realizing novel applications such as suppression or control of unintentional near fields and simple sensing methods in microwave bands.

1.1.3 Electromagnetic scattering in metamaterials

Based on the electromagnetic theorem, electromagnetic propagation phenomenon can be described by dividing into the local phenomena of transmission, reflection, and scattering in a macroscopic viewpoint. However, instantaneous electric and magnetic fields of the waves at a specific point are rigorously obtained by solving the Maxwell equation, and deriving the stationary states of the spatial addition of the local fields correspond to the above macroscopic description. In other words, basically any local and temporal electromagnetic field can be expressed as scattered waves (except incident waves). Assuming elastic scattering which conserves total energies before and after scattering, the scattering phenomenon can be divided into the two types, Rayleigh scattering, and Mie scattering, depending on the ratio of the sizes between a targeted scatterer and a wavelength.

When the wavelength is much larger than the size of a scatterer, the case corresponds to the Rayleigh scattering phenomenon [56, 57], and in the case, spatial distributions of the scattered waves mainly depend on the wavelength and almost not depend on the propagation direction. On the other hand, when the wavelength is about the same size as the scatterer, the case corresponds to the Mie scattering phenomenon [58, 59], and in the case, the spatial distributions mainly depend on the propagation direction and almost not depend on the wavelength.

Based on the above, in a subwavelength region that corresponds to the region between the two regions, The spatial distributions of the scattered waves have a possibility of responding to both a wavelength and a propagation direction of an incident wave, through the scatterer. If such a scatterer can existed in the region, the combination information of a wavelength and a propagation direction of an incident wave can be obtained by measuring and analyzing the spatial distribution of the scattered waves. However, the formation of standing waves by using only the scattering near fields is required to

confirm such feasibility. On the other hand, subwavelength periodic structures such as PCs in the optical region and EBG structures in microwave band are known to be used for suppressing propagation waves since they form periodic boundary conditions those limits propagation modes. And as there is a key point that they can be treated as macroscopic effective media controlling the wave vectors in a wide wavelength range by their structural parameters.

1.1.4 Frequency selective surfaces

As one of the representative metamaterial-technologies in the field of antennas and propagation, there is an FSS. FSS is a spatial filter which reflects or let waves transparent at only specific frequency bands. As basic structures of FSSs, for example, there are a ring-type FSS and a slot-type FSS [60, 61]. FSS is a 2D periodic structure of conductive and dielectric unit cells that function as an impedance surface with resonant frequencies. Therefore, its frequency characteristics are designed by using an equivalent circuit model, and the characteristics of transmission and reflection are generally discussed by using the factors of S_{21} and S_{11} of a scattering matrix [62].

When using FSSs in practical, the characteristics are mainly designed as a band-stop filter or a band-pass filter. For example, a band-stop filter can be designed by forming a series resonant circuit in the unit cell, namely, currents strongly flow on the surface at a resonant frequency and function as a conductor, then incident waves of the resonant frequency reflect. On the other hand, a band-pass filter is designed by forming a parallel-resonant circuit in the unit cell, namely, currents almost never flow on the surface at a resonant frequency, then incident waves of the resonant frequency transmit.

Although FSSs can be designed properly based on the operating principle, it is difficult to guaranteed its performance at any oblique incidence because the frequency characteristics of FSSs are changed by an incident angle [63–65]. The undesired phenomenon is caused by variances of a tangential component of an incident wave vector, and the method to overcome this problem has been studied. For example, there are effective approaches such as miniaturization of the unit cell and stratification of FSSs.

And as other technical issues of FSSs, multiband FSSs-designs [66, 67], and tuning

method of resonant frequencies [68–72] exist. It is a general method that plural resonant circuits are integrated in a unit cell for functioning at multiple frequencies, however since the space is limited, the efficient methods such as forming capacitances between layers of FSSs, multiple arrangement of single band-stop FSSs resonating at different frequencies, and using self-similar resonators (called a fractal structure) in a unit cell to excite resonances of different frequencies. Thus to deal with multi-band design, many effective methods according to each user have been proposed.

On the other hand, tuning methods have been particularly studied in recent years due to its fabrication difficulty. And the most famous tuning method is controlling a resonant frequency by inserting active elements such as varactor diodes in FSS-unit cells. As other methods for tunable FSSs without using external power supplies, there are conventional approaches of tuning the resonant modes by bending the structure like origami and changing capacitances in unit cells by controlling the pressures of liquid-like conductors such as mercury.

1.2 Technical Issues and Approaches

1.2.1 Skin depth engineering

Device design technology is essential for the latest communication systems with high speed and large capacities. The main carriers of their signal transmissions are optical waves and electric waves, and circuit integrations are required for efficient signal transmissions. In the above transmission systems, planar lightwave circuit (PLC) [73,74] and monolithic microwave integrated circuit (MMIC) [75, 76] are used as their core technologies. In the technologies, various analog/digital electronic devices are used for high speed and broadband signal transmissions [77–79], and the transmission lines of the two waves are combined efficiently to reduce the propagation losses of these carriers. However, as the transmission systems become more miniaturized and complicated, the losses are inevitably increased and communication qualities are become deteriorated by such as cross talks, nonlinear effects caused by being broadened a bandwidth of the signals, and instability of the ground of the system.

To prevent the mutual interferences between the different signals and unintentional signal leakages, for example, multiple reflection effects are introduced to the systems by applying diffraction gratings or subwavelength periodic structures to the transmission lines [80]. The method forms destructive interferences by synthesizing wavefronts of the leaked signals, however, if the entire circuits become more integrated, their near fields can be technical issues because of the circuit-miniaturization.

In order to overcome the potential problems, the studies about controlling the skin depth of the near fields have been developed, and they are called skin depth engineering [81–83]. In the studies, nearfields from the transmission lines are suppressed by applying the best combination of the used materials to the circuits. However, there is no versatile method to estimate the skin depth of near fields quantitatively to be applicable for any high-speed circuit systems, although there are the methods that can be applied to the individual circuit in the conventional studies.

Here, the propagation on the boundary between a subwavelength periodic structure and air can be described by an SSPP theory proposed by Pendry [54] and using it, the resonant frequency can be estimated by the structural parameters, and the skin depth also can be estimated by the resonant frequency. Furthermore, SSPP sturucture can be used for the waves of any frequencies, and the fact indicates that the skin depth of the near fields leaked from both optical waves and electric waves can be estimated and suppressed by changing the scale of an SSPP structure and controlling its structural parameters.

1.2.2 Biomedical diagnoses and sensing methods

Electromagnetic-wave sensing technologies can be applicable for a biomedical diagnosis as one of the representative application targets. For example, computed tomography (CT) [84] and magnetic resonance imaging (MRI) [85] are industrially-prevalent imaging methods and although these methods can be useful for cancer detections effectively, they also have technical and industrial issues such as being destructive, their cost and sizes, safety, and convenience. Therefore, non-destructive and simple methods for biomedical diagnosis have been studied in recent years. For example, there are applications of in-

verse scattering analysis to the diagnosis in microwave bands, the imaging method with high resolution using terahertz and optical imaging [86–88].

In the case of methods at microwave-bands, the signals are easily amplified and its devices are fabricated at relatively low cost than the methods of higher frequency bands. However, since the wavelength is larger than measuring targets, there is a technical issue of declines of signal-to-noise ratio causing the deterioration of diagnostic abilities and low resolutions. Furthermore, if waves at 2.45 GHz which is released as an industry science and medical (ISM) band are used to the methods, the energy is absorbed easily by water in living bodies, and dielectric responses of the target may not be obtained properly.

In the case of methods at terahertz wave bands, there are merits of a good transparency in biomedical materials and high resolutions, and since the waves have a feature of exciting intermolecular vibrations and lattice vibrations (phonon), there is a possibility that the more information can be obtained than the case of using only permittivity responses. However, the costs of devices such as a signal generator and signal processing systems are higher than the case of microwave bands, and their fabrication is also difficult.

In the case of methods at optical wavebands, since the wavelength is much smaller than that of other lower frequency bands, the method has a potential of highest resolutions. On the other hand, since the waves have almost no transparency in biomedical materials, the diagnosis of depth directions is difficult and the fabrication cost is relatively higher than the cases of lower frequency bands. Scanning near field optical microscopy (SNOM) is one of the methods at optical wavebands [89], and in the microscopy, the resolution exceeded the limitation of wavelength is realized by reinforcing near field effects. Therefore, it is a good example in the viewpoint of using evanescent waves. Since a skin depth of an evanescent wave is considered to be about a wavelength of an incident wave, the more information of the depth direction can be obtained as the wavelength is longer.

Here, if we use a millimeter wave which can have both a relatively high resolution and a large skin depth as the wave for scanning, diagnosis of the depth direction can be much easier than conventional methods because devices of millimeter-wave band can be fabricated easily and the costs are relatively lower than those of higher frequency

bands and the signal processing is almost not required when using the near fields for the diagnosis. From the above, SSPPs of millimeter-wave bands can be useful for the novel diagnosis method which is considered to solve the industrial and technical issues of the conventional methods. The novel method is considered to be a simple and low-cost diagnosis as a pre-inspection of detailed examinations at hospitals such as CT and PET [84, 90].

1.2.3 Approaches for supporting advanced wireless communication environments

Wireless communication technologies have been rapidly developed variously in recent years. As for license bands, the fourth-generation wireless communication system (4G) which enables us to share mass data not only documents and audio data but also video through the internet prevailed, and the fifth-generation wireless communication system (5G) which has a potential of sharing more massive data such as 3D data for virtual reality (VR) and augmented reality (AR) is being put to practical use. Apart from these communication systems, satellite communication systems such as a global positioning system (GPS) and broadcasting systems are also used. Therefore, wireless communication environments became more complicated since the waves used for various communication systems with different frequency bands are being mixed in the same space. Namely, in order to keep the wireless environments stable conditions for supporting these advanced wireless communication systems, it is necessary to operate frequency and spatial resources effectively.

And in a viewpoint of electromagnetic environments, they also include unintentional electromagnetic emanations from various devices. Therefore, it is also necessary to design reliable environments in terms of electromagnetic compatibility (EMC) [91, 92]. Although it is important to design the complex wireless communication environments with the consideration of EMC design in advance, the practical systems are required to construct advanced environments that are considered to coexistence with the existing systems in order to realize sustainable and continuous developments of the systems. In other words, versatile and immediate techniques to deal with problems such as elec-

tromagnetic interferences and malfunctions of communication devices are essential in practical developments. For example, if the method identifying unnecessary-radiation sources in broadband and the method to separate or cut off electromagnetic waves locally in terms of frequency and space can be applied, the above problems causing deterioration of communication qualities can be solved instantaneously.

Here, the former method is called direction-of-arrival estimation (DOA) method and has been actively studied so far. For example, the method using phase differences of detected signals using array antennae and the imaging method of two-dimensional spatial distributions of signal intensities using EBG structures as electromagnetic absorbers are already existed [93, 94]. However, since the advanced environments require more frequency bands and spaces, the above methods are essential to be miniaturized and improved in terms of the applicable bandwidth. Here, if the subwavelength periodic structure of scatterers are used for a DOA method, the size can be miniaturized and the applicable bandwidth can broaden since the structure can be treated as an effective medium since the operating principle is different from the conventional method such as an array antenna which uses each element as an individual signal detector. The method has a potential of extracting combination information of frequencies and incident angles of targeted waves by detecting the spatial distributions of the scattering patterns based on only amplitude information since the structure can form standing distributions by the boundary between the effective medium and air.

On the other hand, the latter method is mainly based on shielding techniques, and the electromagnetic shield has been studied so far. As the conventional methods, a perforated conductor plate that cut off waves by magnetic dipole effects, a transparent conductive shield film, and an electromagnetic absorber using such as an EBG structure have been proposed [95]. However, these methods are focused on only a point of their shielding effects such as applicable bandwidths and transparencies of the untargeted waves in use are not considered. Therefore, the advanced method which only cuts off the targeted wave effectively is required for supporting the complex electromagnetic environments. As an applicable technique, there is an FSS whose reflection frequency characteristics can be controlled. However, FSSs can be used only in the case that frequency bands of

the targeted waves are known in advance.

Although tunable FSSs which can be controlled the operating frequency bands also exist, they require active elements in them and an external power supply for controlling the capacitances of the elements or the alternative method without an external power supply is a fabrication of a three-dimensional complicated FSS of whose operating frequency bands is controlled by bending.

These tunable FSSs are essential to be improved for the use in practice in terms of simplicity and mass productivity. Here, if the metamaterial design principle is applied, there is a possibility that the adjustable FSS can be realized with a simplified design whose operating frequency bands can be controlled without using an external power supply, by shifting the layers of the thin FSS to control the capacitances of each unit cell. This is because the miniaturized FSS according to the metamaterial design principle can be treated as a simplified equivalent circuit model using only lumped elements even though the FSS has a multilayered structure.

1.3 Structure of this Thesis

In this thesis, electromagnetic behaviors in subwavelength periodic structures are examined and their applications for various devices are reported, based on the theoretical concept of metamaterials. Specifically, as followed to the outline shown in Fig. 1.2, first electromagnetic controls of propagation conditions in two-dimensional subwavelength periodic structures are discussed, next, the advanced technologies of SSPP, FSS, and artificial medium based on the discussion are applied to high-frequency devices for skin depth engineering, biomedical diagnosis, and wireless communication.

In the study of the electromagnetic controls of propagation conditions in two-dimensional periodic structures, the change of the propagation characteristics in accordance with the thickness of the structures are discussed by using a metal hole array (MHA) which is a representative structures of an SSPP, and a metal plate array (MPA) which is a complementary structure of an MHA. When the structures are treated as boundaries, it is known that the propagation characteristics follow to Babinet ' s principle that the

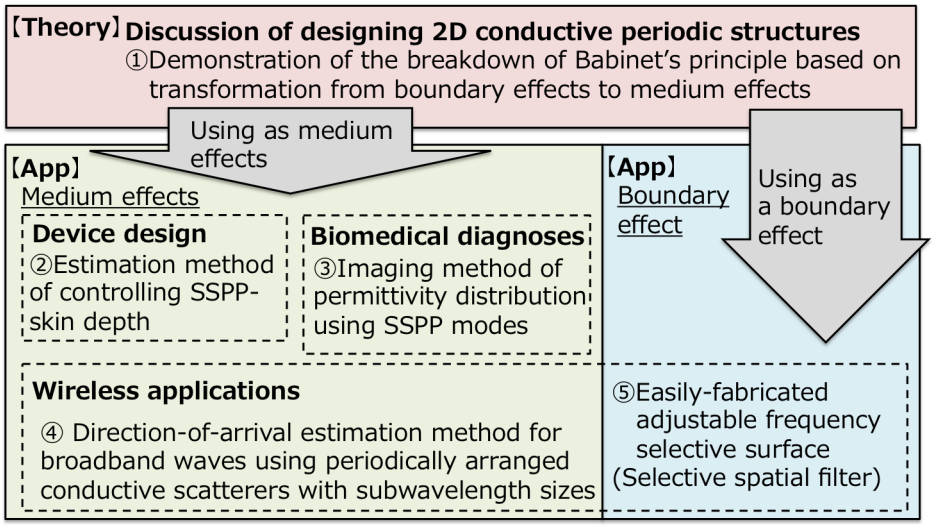

Figure 1.2: The outline of this thesis.

complementary structure shows the inverted transmission characteristics of the original structure. On the other hand, treating the structures as effective media with a sufficient thickness, SSPP modes should be formed on the structures and the fact indicates that both structures show band-pass characteristics, therefore, if the thickness is varied properly the breakdown of Babinet ' s principle can be seen at a specific condition. First a theory of SSPP generation on the structures is introduced and the breakdown of Babinet ' s principle is discussed theoretically. Next, the changes in transmission characteristics in the two structures in accordance with their thickness are confirmed analytically and experimentally. By using these results, the breakdown of Babinet ' s principle is demonstrated.

As a first application, a theoretical estimation method of skin depth of SSPPs in millimeter or terahertz wavebands for suppressing near fields around transmission lines is proposed and examined theoretically and experimentally. Specifically, the theoretical value of a skin depth of an SSPP is derived and the values at different frequencies are compared with the experimental values.

Second, a novel imaging method for a simple biomedical diagnosis focusing on a dynamic control of SSPP modes on an MHA is proposed and examined analytically and experimentally. Specifically, after examining the feasibility of detecting dielectric responses on an MHA by an active control of local fields of SSPP modes intensified by

a needle-like conductor, two-dimensional imaging experiments of conductive, dielectric and biomedical samples by using the method are conducted.

As wireless applications, a broadband and miniaturized devices for DOA estimations and a simplified adjustable FSS whose resonant frequency can be controlled in broadband, are proposed and examined.

As a DOA device, the subwavelength periodic structure of conductive scatterers (SPCS) for formations of scattering patterns of 2 - 6 GHz is designed and fabricated. By using the structure, the spatial distributions of the patterns at various frequencies and incident angles are analyzed and detected experimentally.

And a three-layered FSS which shows various resonant frequencies in accordance with its stacked conditions is designed and fabricated. The capacitances formed between the adjacent layers can be varied by shifting the layers each other, and the resonant frequency can be controlled using the designed value of the capacitances. This operating principle and the angular dependencies in the various cases are examined analytically and experimentally by analyzing and measuring the transmission characteristics.

In Chapter 2, the study of the electromagnetic controls of propagation conditions in two-dimensional periodic structures is reported. In Chapter 3, the estimation method of the skin depth of SSPPs is explained. In Chapter 4, an imaging method for a simple biomedical diagnosis is described. In Chapters 5 and 6, the studies of the broadband and miniaturized DOA device and the adjustable FSS for wireless applications are introduced. Finally, the studies are summarized in the conclusion.

References

[1] T. Mavridis, J. Sarrazin, L. Petrillo, P. D. Doncker and A. B. Delaï, IEEE Trans. Antennas. Wireless Propag. Lett. **14**, 20 (2015).

[2] L. C. Fernandes and A. J. M. Soares, IEEE Trans. Antennas. Wireless Propag. Lett. **9**, 24 (2010).

[3] G. Ren, T. G. Nguyen and A. Mitchell, IEEE Photon. Technol. Lett. **26**, 1438 (2014).

[4] T. Fukushima, T. Yokota and T. Sakamoto, J. Lightwave Technol. **15**, 1938 (1997).

[5] Y. Wu, Y. Hao, J. Liu and K. Kang, IEEE Microw. Wireless Compon. Lett. **27**, 651 (2017).

[6] Y. C. Chang, P. Y. Wang, D. C. Chang and S. S. H. Hsu, IEEE Trans. Microwave Theory Tech. **67**, 1652 (2019).

[7] K. K. Tse, H. S. Chung and S. Y. R. Hui, IEEE Trans. Ind. Electron. **46**, 91 (1999).

[8] C. Buttay, H. Morel, B. Allard, P. Lefranc and O. Brevet, IEEE Trans. Power Electron. **21**, 613 (2006).

[9] J. B. Pendry, Phys. Rev. Lett. **85**, 3966 (2000).

[10] R. A. Shalby, D. R. Smith and S. Schultz, Science **292**, 77 (2001).

[11] L. Zhang, Y. Zhang, L. He, H. Li, and H. Chen, Phys. Rev. E **74**, 056615 (2006).

[12] D. E. Brocker, J. P. Turpin, P. L. Wrener and D. H. Werner, IEEE Trans. Antennas. Wireless Propag. Lett. **13**, 1787 (2014).

[13] A. Keshavarz and Z. Vafapour, IEEE Trans. Sens. J. **19**, 1519 (2019).

[14] H. F. Ma, B. G. Cai, T. X. Zhang, Y. Yang, W. Xiang and T. J. Cui, IEEE Trans. Antennas. Propag. **61**, 2561 (2013).

[15] T. W. Ebbesen, H. J. Lezac, H. F. Ghaemi, T. Thio, and P. A. Wolff, Nature (London) **391**, 667 (1998).

[16] S. Li, H. Liu, Q. Sun and N. Huang, IEEE Photon. Technol. Lett. **27**, 752 (2015).

[17] R. Yahiaoui, A. C. Strikwerda and P. U. Jepsen, IEEE Trans. Sens. J. **16**, 2484 (2016).

[18] M. Rezaei, P. Rasekh and R. Safian, IEEE Photon. Technol. Lett. **27**, 2288 (2015).

[19] B. A. Munk, *Frequency-Selective Surfaces: Theory and Design* (Wiley, 2000).

[20] F. Falcone, T. Lopetegi, M. A. G. Laso, J. D. Baena, J. Bonache, M. Beruete, R. marques, F. Martin, and M. Sorolla, Phys. Rev. Lett. **93**, 197401 (2004).

[21] J. Persons, E. Hendry, C. P. Burrows, B. Auguie, J. R. Sambles, and W. L. Barnes, Phys. Rev. B **79**, 073412 (2009).

[22] L. Zhang, T. Koschly, and C. M. Soukoulis, Phys. Rev. B **87**, 045101 (2013).

[23] G. Pelosi, and S. Selleri, IEEE Antennas Propag. Magazine **59**, 144 (2017).

[24] A. Bitzer, A. Ortner, H. Merbold, T. Feurer, and M. Walther, Opt. Exp. **19**, 2537 (2011).

[25] S. M. Amin, M. H. Abadi, K. Ghaemi, and N. Behdad, IEEE Trans. Antennas Propag. **63**, 534 (2015).

[26] J. H. Kim, H. J. Chun, I. P. Hong, Y. J. Kim, and Y. B. Park, IEEE Trans. Antennas. Wireless Propag. Lett. **13**, 868 (2014).

[27] K. Zhang, W. Jiang, and S. Gong, IEEE Trans. Antennas. Wireless Propag. Lett. **16**, 2856 (2017).

[28] J. M. Bell and M. F. Iskander, IEEE Trans. Antennas. Wireless Propag. Lett. **7**, 573 (2008).

[29] S. Arslanagić and R. W. Ziolkowski, Phys. Rev. B **120**, 237401 (2018).

[30] Y. Kurosaka, S. Iwahashi, Y. Liang, K. Sakai, E. Miyai, W. Kunishi, D. Ohnishi and S. Noda, Nat. Photonics **4**, 447 (2010).

[31] A. Sanada, C. Caloz, and T. Itoh, IEEE Trans. Microwave Theory Tech. **52**, 1252 (2004).

[32] G. V. Eleftheriades, A. K. Iyer, and P. C. Kremer, IEEE Trans. Microwave Theory Tech. **50**, 2702 (2002).

[33] J. T. Costa, and M. G. Silveirinha, Phys. Rev. B **84**, 155131 (2011).

[34] P. Y. Chen and A. Alú, Phys. Rev. B **84**, 205110 (2011).

[35] D. R. Smith, J. J. Mock, A. F. Starr and D. Schurig, Phys. Rev. E **71**, 036609 (2005).

[36] W. Yang, S. Chen, W. Che, Q. Xue and Q. Meng, IEEE Trans. Antennas Propag. **66**, 4918 (2018).

[37] A. Alú and N. Engheta, IEEE Trans. Antennas. Wireless Propag. Lett. **4**, 417 (2005).

[38] J. Dai, S. A. Dyakov, S. I. Bozhevolnyi and M. Yan, Phys. Rev. B **94**, 125431 (2016).

[39] O. Kostiucenko, J. Fiutowski, T. Kawalec, V. Bordo, H. G. Rubahn, and L. Jozefowski, Opt. Commun. **331**, 77 (2014).

[40] Z. Yang, D. Gu, and Y. Gao, Opt. Commun. **329**, 180 (2014).

[41] J. Katyal and R. K. Soni, Plasmonics **9**, 1171 (2014).

[42] J. N. Anker, W. P. Hall, O. Lyandres, N. C. Shah, J. Zhao and R. P. V. Duyne, Nat. Mater. **7**, 442 (2008).

[43] L. E. Kreno, K. K. Leong, O. K. Farha, M. Allendorf, R. P. V. Duyne and J. T. Hupp, Chem. Rev. **112**, 1105 (2012).

[44] H. Sugai, I. Ghanashev, and M. Nagatsu, Plasma Sources Sci. Technol. **7**, 192 (1998).

[45] M. Moisan, A. Shivarova, and A. W. Travelpiece, Plasma Phys. **24**, 1331 (1982).

[46] F. Miyamaru, M. Kamijyo, N. Hanaoka, and M. W. Takeda, App. Phys. Lett. **100**, 081112 (2012).

[47] F. Miyamaru, S. Hayashi, C. Otani, K. Kawase, Y. Ogawa, H. Yoshida, and E. Kato, Opt. Lett. **31**, 1118 (2006).

[48] F. Miyamaru and M. Hangyo, App. Phys. Lett. **84**, 2742 (2004).

[49] F. Miyamaru, M. Tanaka, and M. Hangyo, Phys. Rev. B **74**, 153416 (2006).

[50] S. Bhattacharya and K. Shah, Opt. Commun. **328**, 102 (2014).

[51] Y. Wu, M. Li, G. Yan, L. Deng, Y. Liu, and Z. Ghassemlooy, AIP Adv. **6**, 105110 (2016).

[52] H. T. Chen, H. Lu, A. K. Azad, R. D. Averitt, A. C. Gossard, S. A. Trugman, J. F. O'Hara, and A. J. Taylor, Opt. Express **16**, 7643 (2008).

[53] F. F. Qin, J. J. Xiao, Z. Z. Liu and Q. Zhang, IEEE Trans. Microwave Theory Tech. **64**, 1186 (2016).

[54] J. B. Pendry, L. M. Moreno, and F. J. G. Vidal, Science **305**, 847 (2004).

[55] F. J. G. Vidal, L. M. Moreno, and J. B. Pendry, J. Opt. A: Pure Appl. Opt. **7**, S97 (2005).

[56] K. Tsujikawa, K. Tajima and M. Ohashi, J. Lightwave Technol. **18**, 1528 (2000).

[57] J. A. Lazaro, C. Arellano, V. Polo and J. Prat, IEEE Photon. Technol. Lett. **19**, 64 (2007).

[58] Y. L. Geng and C. W. Qiu, IEEE Trans. Antennas Propag. **59**, 4364 (2011).

[59] G. Liu, Y. Liu, K. Li, P. Hao, P. Zhang and M. Xuan, IEEE Photon. Technol. Lett. **24**, 24 (2012).

[60] S. Ghosh and K. V. Srivastava, IEEE Trans. Antennas. Wireless Propag. Lett. **14**, 511 (2015).

[61] G. H. Dadashzadeh, M. H. Amini and A. R. Mallahzadeh, J. Commun. Eng. **3**, 23 (2014).

[62] K. Sarabandi and N. Behdad, IEEE Trans. Antennas Propag. **55**, 1239 (2007).

[63] G. Itami, Y. Toriumi, and J. Kato, Proc. Asia-Pacific Microw. Conf. (APMC), Kyoto, Japan, Nov. (2018).

[64] S. N. Azemi, K. Ghorbani, and W. S. T. Rowe, IEEE Microw. Wireless Compon. Lett. **25**, 454 (2015).

[65] C. N. Chiu and K. P. Chang, IEEE Trans. Antennas. Wireless Propag. Lett. **8**, 1175 (2009).

[66] S. Khan and T. F. Eibert, IEEE Trans. Antennas Propag. **66**, 4042 (2018).

[67] S. Zhang, Y. Yin, J. Fan, X. Yang, B. Li and W. Liu, IEEE Trans. Antennas. Wireless Propag. Lett. **11**, 240 (2012).

[68] F. Bayatpur and K. Sarabandi, IEEE Trans. Antennas Propag. **57**, 1433 (2009).

[69] X. Zeng, L. Zhang, G. Wan, B. Hu, B. Huang, and J. Shen, Proc. Int. Symp. Antennas Propag. EM Theory (ISAPE), Gulin, China, Oct. (2016).

[70] A. Tennant and B. Chambers, IEEE Microw. Wireless Compon. Lett. **14**, 46 (2004).

[71] M. Li, B. Yiu, and N. Behdad, IEEE Microw. Wireless Compon. Lett. **20**, 423 (2010).

[72] K. Fuchi, J. Tang, B. Crowgey, A. R. Diaz, E. J. Rothwell, and R. O. Ouedraogo, IEEE Trans. Antennas. Wireless Propag. Lett. **11**, 473 (2012).

[73] B. S. Rho and J. W. Lim, IEEE Photon. Technol. Lett. **18**, 1867 (2006).

[74] J. Ito, H. Tsuda, IEEE Photon. Technol. Lett. **27**, 786 (2009).

[75] S. Beer, H. Gulan, C. Rusch and T. Zwick, IEEE Trans. Antennas Propag. **61**, 1564 (2013).

[76] Z. Briqech, A. R. Sebak and T. A. Denidni, IEEE Trans. Antennas. Wireless Propag. Lett. **12**, 1224 (2013).

[77] H. Yamazaki, M. Nagatani, H. Wakita, Y. Ogiso, M. Nakamura, M. Ida, H. Nosaka, T. Hashimoto, Y. Miyamoto, J. Lightwave Technol. **37**, 1772 (2019).

[78] S. Nishihara, S. Kimura, T. Yoshida, M. Nakamura, J. Terada, K. Nishimura, K. Kishine, K. Kato, Y. Ohmoto, N. Yoshimoto, T. Imai and M. Tsubokawa, J. Lightwave Technol. **26**, 99 (2008).

[79] K. Kishine, H. Inaba, H. Inoue, M. Nakamura, A. Tsuchiya, H. Katsurai and H. Onodera, IEEE Trans. Circuits Syst. **62**, 1288 (2015).

[80] X. Feng, H. Y. Tam and P. K. A. Wai, IEEE Photon. Technol. Lett. **18**, 1088 (2006).

[81] S. Jahani and Z. Jacob, Nature Nanotechnol. **11**, 23 (2016).

[82] A. Vora, J. Gwamuri, A. Kulkami, J. M. Pearce, and D. O. Guney, Sci. Rep. **4**, 4901 (2014).

[83] T. Li, H. Liu, F. M. Wang, Z. G. Dong, and N. Zhu, Opt. Express **14**, 11155 (2006).

[84] S. B. Haim, V. L. Murthy, C. Breault, R. Allie, A. Sitek, N. Roth, J. Fantony, S. C. Moore, M. A. Park, and M. Kijewski, J. Nucl. Med. **54**, 873 (2013).

[85] T. S. Sorensen, D. Atkinson, T. Schaeffter and M. S. hansen, IEEE Trans. Med. Imag. **28**, 1974 (2009).

[86] P. Paul, F. G. Guimaráes and J. P. Webb, IEEE Trans. Magn. **45**, 1514 (2009).

[87] T. Jyo, H. Hamada, D. Kitayama, M. Yaita and H. Nosaka, IEEE Trans. Terahertz. Sci. Technol. **8**, 278 (2018).

[88] V. Ntziachristos, Nat. Methods **7**, 603 (2010).

[89] A. E. Klein, N. Janunts, M. Steinert, A. Tunnermann, and T. Pertsch, Nano Lett. **14**, 5010 (2014).

[90] C. C. Meltzer, J. C. Prlce, C. A. Mathis, P. J. Greer, M. N. Cantwell, P. R. Houck, B. H. Mulsant, D. B. Loprestl, and S. T. Dekosky, Am. J. Psychiatry **156**, 1871 (1999).

[91] G. Manzi, M. Feliziani, P. A. Beeckman and N. V. Dijk, IEEE Trans. Electromagn. Compat. **51**, 382 (2009).

[92] M. Ardavan, C. W. Trueman and K. A. Schmitt, IEEE Trans. Electromagn. Compat. **57**, 69 (2015).

[93] R. Mueller and R. Lorch, Proc. 2015 9th Eur. Conf. Antennas Propag. (EuCAP), Lisbon, Portogal, April (2015).

[94] S. Yagitani, K. Katsuda, M. Nojima, Y. Yoshimura, and H. Sugiura, IEICE Trans. Commun. **E94-B**, 2306 (2011).

[95] D. A. Lampasi, A. Tamburrano, S. Bellini, M. Tului, A. Albolino and M. S. Sarto, IEEE Trans. Electromagn. Compat. **56**, 352 (2014).

Chapter 2

Analysis and Observation of the Breakdown of Babinet's Principle in Complementary Spoof Surface Plasmon Polariton Structures

2.1 Introduction

The behavior of electromagnetic waves interacting with objects is broadly classified into two cases. For wavelengths significantly larger than the object, the wave's electric fields are treated as near fields and electromagnetic behavior is expressed as a scattering phenomenon. For wavelengths much smaller than the object the wave's electric fields are treated as far fields and the electromagnetic behavior is expressed as propagating waves, either transmitted or reflected. However, when the wavelength is of the same order as the object size, the scattering phenomena become more complex. In this case, if such objects are perforated periodically, they can be provide an interesting medium with properties, otherwise not attainable with naturally occurring materials, such as a negative refractive index (NRI) [1–6]. In general, these artificial structures are called metamaterials.

In 2000, Pendry showed theoretically the concept of a perfect lens with a negative

refractive index (NRI) medium [1], and in 2001, Shelby *et al.* verified the possibility of an NRI experimentally by using the two artificial resonators for negative permeability and permittivity media [2]. Their studies demonstrated the feasibility of metamaterials, and accelerated the advances in the field in recent years [1–3, 7–12]. In such studies, a split ring resonator (SRR) is often used as a negative permeability medium for NRI realizations. And the complementary split ring resonator (CSRR) is also known as the resonator for negative permittivity realization, based on Babinet's principle [12–16]. In these two resonators, the essential difference in their resonance is based on the following electromagnetic radiation mechanisms: SRR radiates the topologically overlaid waves from the infinitesimal electric dipoles, and CSRR radiates them from the infinitesimal magnetic dipoles. Based on this principle, the SRR and CSRR show band-stop and band-pass characteristics if they are used as planar spatial filters.

A frequency selective surface (FSS) is also a spatial filter which ha a two-dimensional structure with a unit cell and resonators, and is a metamaterial in a broader definition of the term [11, 17–22]. Its operating principle is often expressed by using an equivalent circuit model. For example, a patch-type FSS and a slot-type FSS respectively show band-stop and band-pass characteristics, since they have series and parallel resonant circuits in their boundaries. Therefore, an FSS's operation principle is also consistent with Babinet's principle. On the other hand, a spoof surface plasmon polariton (SSPP) is also a feature of metamaterials [23–35]. It is the collective oscillation of electric fields like a surface wave in the microwave-frequency range. A metal hole array (MHA), which is a two dimensional conductive structure with periodic perforations, is often used for SSPP excitations [24–29]. When SSPP modes are excited on the surface, transmittance is up to 100 percent (extraordinary transmission) [36, 37] in an optimal frequency band, since the modes of both sides are coupled to each other.

From a different point of view, an MHA can be considered a spatial filter with band-pass effects. According to the SSPP theorem proposed by Pendry *et al.*. [23,29], an MHA can be a macroscopic medium with a controllable permittivity of Drude-type frequency response, as is derived by solving a wave equation with microscopic boundary conditions such as waveguide modes taken into consideration. In the theorem, the boundary condi-

tions are not limited to specific conditions [13, 31, 33]. For example, a metal plate array (MPA), which is the complementary structure of an MHA, should also be an SSPP-structure with band-pass effects.

However, an MPA is inversely treated as a band-stop FSS when it is a very thin structure. Although conventional studies have discussed clarifications of the relationship between SSPP modes and the structural parameters or the boundary conditions, the relevant part of an SSPP theory in terms of structural thickness in structure has not been discussed in detail. In other words, an MPA has the potential to provide evidence of the breakdown of Babinet's principle.

In this study, an example of such a breakdown of Babinet's principle is demonstrated by using an MPA and an MHA thicknesses nearly the size of the interacting wavelength. First, changes in the relationships between electromagnetic behavior at the boundary conditions and the transmission or reflection properties of the two complementary structures, with the variations in their thickness, are discussed theoretically and analytically. The theoretical wave propagation model and the analytical study of MPAs indicated the possibility of a Babinet's principle exception. And experimental results verified the theoretical assumption and analytical results using fabricated MPAs and MHAs with their wavelength-size thickness. This fact gives us more detailed physical insight into electromagnetic wave-propagations, and is useful for designing spatial filters, antennas and artificial lenses [20, 38–41].

In Section 2.2, SSPP mode generation on an MPA is discussed by introducing a theoretical wave propagation model, and the effective relative permittivity and the dispersion relation are derived. In Section 2.3, the changes in transmission and reflection properties and the angular dependencies of transmission characteristics of MPAs and MHAs are examined by varying their thickness analytically with the use of an electromagnetic simulator (HFSS, Ansys). In Section 2.4, the transmission characteristics of the two structures in their thin and thick cases are examined experimentally. Finally, we summarize our study, which theoretically and experimentally demonstrates the breakdown of Babinet's principle.

2.2 Basis of Spoof Surface plasmon Polaritons Generations on A Metal Plate Array

In this study, the breakdown of Babinet's principle is discussed based on the physical insights of SSPP mode generation and FSS's operating principles (equivalent circuit model) [17–19, 21]. The phenomenon can be observed in an MPA by increasing its thickness, since the theoretical model of electromagnetic behavior on the boundary is changed from the latter to the former. If the MPA is a thin structure like a surface, its frequency characteristics can be expressed by using its equivalent circuit model, which shows a series resonant circuit in the admittance of an MPA. Also, if the MPA is a thick structure, its frequency characteristics can be expressed by using the SSPP theory proposed by Pendry *et al.* [23, 29], as shown in Fig. 2.1.

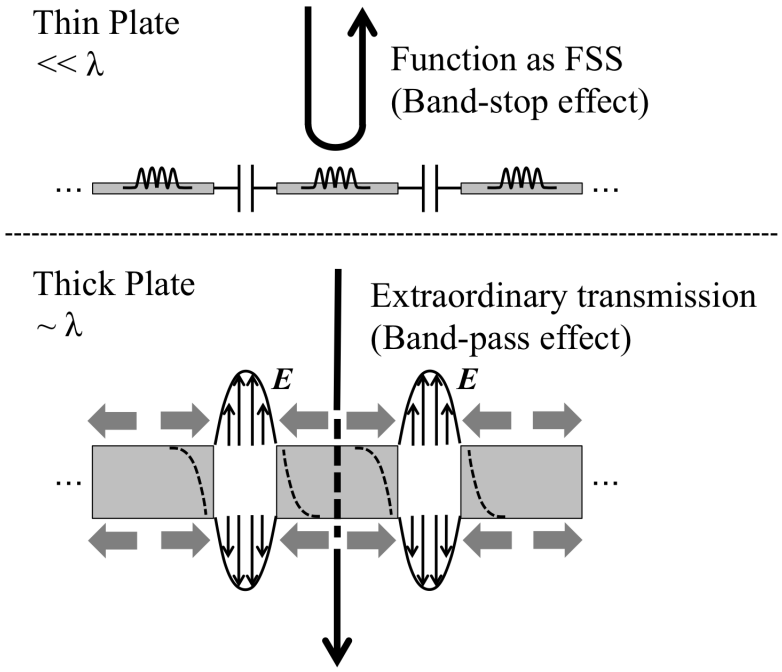

Figure 2.1: Physical concept of changing a propagation model in accordance with the boundary shift from an FSS-boundary to an SSPP-boundary in the case of a metal plate array.

Therefore, as well as SSPP mode generation on an MHA, an MPA can also generate SSPP modes on itself. The theoretical derivation can be described using the same

framework. Here, TM-polarized waves entered an MPA at an oblique incidence as shown in Fig. 2.2, and each conductive plate in the MPA is assumed to be a perfect electric conductor. In this case, since an incident magnetic field $\boldsymbol{H}$ has only a y-component, the vector is expressed as $\boldsymbol{H} = [0, H_y, 0]$. And the incident electric field vector must also have only x- and z-components, and $\boldsymbol{E} = [E_x, 0, E_z]$. The conductive plates are arranged two-dimensionally with a period d, and the size of each plate is $a \times a$, with depth w. It is assumed that the values of a, d and w are of the same order as the incident wavelength, and a unit cell is defined as a space $d \times d$ so as to satisfy the condition that an conductive plate is centered in it, as shown in Fig. 2.3. Assuming the propagation is from Region 1 to Region 2 in Fig. 2.2, the waves should propagate with parallel plate-waveguide modes around the boundary $z = 0$. Note that the permittivity and permeability in Region 1 are $\epsilon = \epsilon_0, \mu = \mu_0$, respectively and the two values in Region 2 are also expressed as $\epsilon = \epsilon_\mathrm{r}\epsilon_0, \mu = \mu_\mathrm{r}\mu_0$. Here ϵ_r and μ_r are effective relative permittivity and permeability in Region 2; those also represent the macroscopic electromagnetic profiles of an MPA.

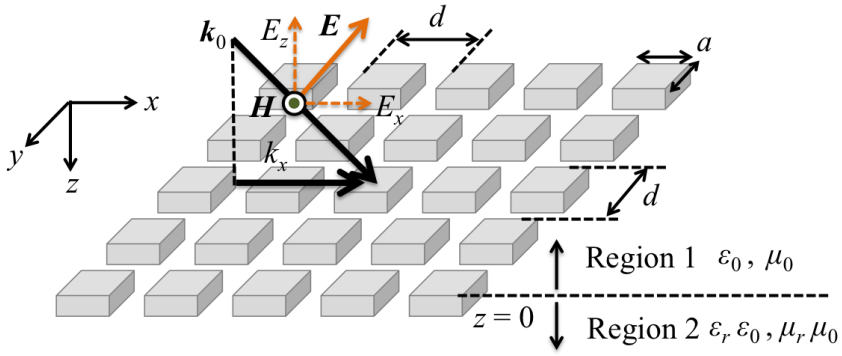

Figure 2.2: Schematic view of electromagnetic propagation on a metal plate array.

Considering the boundary conditions, energy flow around the boundary, and an SSPP generation condition, macroscopic permittivity and permeability of an MPA are obtained, and an SSPP-dispersion relation in an MPA can be derived by using the two parameters. In the derivations, it is specified that $\mathrm{j} = \sqrt{-1}$ and it is assumed that the incident wave is a plane wave; therefore the time operator is expressed as $\partial/\partial t = \mathrm{j}\omega$. Here, the x- and z-components of the incident electric field E_x and E_z in Region 1 are

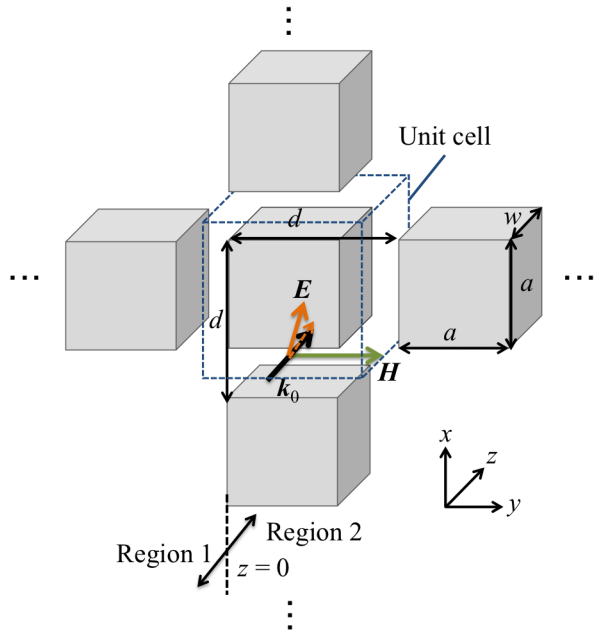

Figure 2.3: Microscopic view of the propagation on a metal plate array per unit cell.

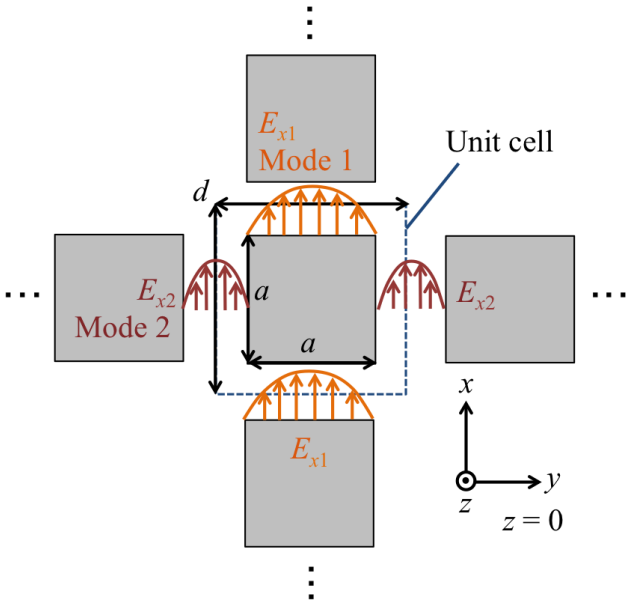

Figure 2.4: Electric distributions on a metal plate array following the microscopic boundary conditions.

expressed as

$$E_x = E_{x0} \exp \mathrm{j}(k_x x + k_z z), \tag{2.1}$$

$$E_z = E_{z0} \exp \mathrm{j}(k_x x - k_z z). \tag{2.2}$$

In the above expressions, the time vibrational term $\exp(\mathrm{j}\omega t)$ is omitted for simplicity. Note that E_{x0} and E_{z0} are the amplitudes values of E_x and E_z, and that k_x and k_z are the x- and z-components of the incident wave vector $\boldsymbol{k}$. On the other hand, considering the propagation modes inside an MPA, the waves should have parallel-plate waveguide modes. Here, if the incident wavelength satisfies $\lambda << a$, the fundamental waveguide mode is dominant [23, 29]. And in a unit cell of an MPA, the propagation modes can be classified into the two modes: Mode 1 and Mode 2, as shown in Fig. 2.4. Thus, the x-components of the electric field E_x can take the two forms

$$E_{x1} = E_0 \sin(\frac{\pi y}{a}) \exp(-\beta_1 z), \tag{2.3}$$

$$\beta_1 = \sqrt{(\frac{\pi}{a})^2 - \omega^2 \epsilon_0 \mu_0} \tag{2.4}$$

$$E_{x2} = E_0 \sin(\frac{\pi y}{d-a}) \exp(-\beta_2 z), \tag{2.5}$$

$$\beta_2 = \sqrt{(\frac{\pi}{d-a})^2 - \omega^2 \epsilon_0 \mu_0}. \tag{2.6}$$

Here, β_1 and β_2 are propagation constants, and E_{x1} and E_{x2} show the electric field E_x of the two waveguide modes Mode 1 and Mode 2, respectively. These modes are excited on an MPA per unit cell as shown in Fig. 2.4. When an MPA is treated as a macroscopic medium, the average electric field intensity per unit cell can be derived as

$$\begin{aligned}\overline{E_0} &= E_0\frac{1}{d^2}[(d-a)\int_0^a \sin(\frac{\pi y}{a})dy + a\int_0^{d-a}\sin(\frac{\pi y}{d-a})dy] \\ &= \frac{4a(d-a)}{\pi d^2}E_0\end{aligned} \tag{2.7}$$

Where $\overline{E_0}$ is the average electric field intensity. Considering an energy flow across the boundary $z = 0$, the inflow from the upper side and the outflow to lower side must take the same value. Here, if an MPA is treated as a microscopic structure or macroscopic uniform medium, the energy flow can be expressed in two ways, that is

$$\begin{aligned}(\boldsymbol{E}\times\boldsymbol{H})_{z,\mathrm{micro}} &= \frac{-k_z E_0^2}{\omega\mu_0}\frac{1}{d^2}[(d-a)\int_0^a \sin^2(\frac{\pi y}{a})dy + a\int_0^{d-a}\sin^2(\frac{\pi y}{d-a})dy] \\ &= \frac{-k_z}{\omega\mu_0}{E_0}^2\frac{a(d-a)}{d^2},\end{aligned} \tag{2.8}$$

$$(\boldsymbol{E}\times\boldsymbol{H})_{z,\mathrm{macro}} = \frac{-k_z}{\omega\mu_\mathrm{r}\mu_0}\overline{E_0}^2 = \frac{-k_z}{\omega\mu_\mathrm{r}\mu_0}{E_0}^2\frac{16a^2(d-a)^2}{\pi^2 d^4}. \tag{2.9}$$

And considering the equation $(\boldsymbol{E}\times\boldsymbol{H})_{z,\mathrm{micro}} = (\boldsymbol{E}\times\boldsymbol{H})_{z,\mathrm{macro}}$, the macroscopic relative permeability μ_r is obtained as

$$\mu_\mathrm{r} = \frac{16a(d-a)}{\pi^2 d^2}. \tag{2.10}$$

The macroscopic relative permittivity ϵ_r also can be obtained by considering the propagation constant, as well as the energy flow. If treating an MPA as a macroscopic medium, the waves in Region 2 cannot propagate in x- and y-directions. Therefore, the incident wave vector in the macroscopic medium should have only a z-component. In other words, the wave vector $\boldsymbol{k'}$ can be expressed as $\boldsymbol{k'}$=$[0, 0, k'_z]$, and k'_z is

$$k'_z = \sqrt{\epsilon_\mathrm{r}\mu_\mathrm{r}}k_0. \tag{2.11}$$

Here, k_0 is the wavenumber in free space, and it satisfies $k_0 = \omega\sqrt{\epsilon_0\mu_0}$. As shown in the Eqs. (2.3) - (2.6), there are two fundamental modes inside an MPA, so the macroscopic relative permittivity ϵ_{r} can be expressed by the following equation by using the two relative permittivities $\epsilon_{\mathrm{r}1}$ and $\epsilon_{\mathrm{r}2}$, yielding

$$\epsilon_{\mathrm{r}} = \frac{a\epsilon_{\mathrm{r}1} + (d-a)\epsilon_{\mathrm{r}2}}{d}. \tag{2.12}$$

Note that these values correspond to the behaviors of the electric fields of E_{x1} and E_{x2}, respectively. And considering the propagation constants inside an MPA from the viewpoints of treating it as a microscopic and a macroscopic medium, the values of $\epsilon_{\mathrm{r}1}$ and $\epsilon_{\mathrm{r}2}$ can be derived with the use of the expressions (2.4), (2.6) and (2.11) by forming the following equation,

$$(k_{zi} =)\sqrt{\epsilon_{\mathrm{r}i}\mu_{\mathrm{r}i}}k_0 = \beta_i, i = 1, 2. \tag{2.13}$$

Then, by substituting (2.4) and (2.6) into (2.13), the values of $\epsilon_{\mathrm{r}1}$ and $\epsilon_{\mathrm{r}2}$ are obtained as

$$\epsilon_{\mathrm{r}i} = \frac{\pi^2 d^2}{16a(d-a)}[1 - \frac{(\pi c_0)^2}{A_i\omega^2}], \quad A_i = \begin{cases} a & i = 1 \\ d-a & i = 2 \end{cases}. \tag{2.14}$$

Note that Eq. (2.10) is used in the above derivation, and c_0 is the velocity of light in free space. Therefore, by using the expressions (2.10), (2.12) and (2.14), the macroscopic relative permittivity ϵ_{r} is obtained as

$$\epsilon_{\mathrm{r}} = \frac{\pi^2 d^2}{16a(d-a)}[1 - \frac{{\omega_{\mathrm{p}}}^2}{A_i\omega^2}], \quad \omega_{\mathrm{p}} = \frac{\pi c_0}{\sqrt{a(d-a)}}. \tag{2.15}$$

Here, ω_{p} is the cut-off frequency of an MPA. As shown in Eq. (2.15), an MPA also has a relative permittivity with the same frequency response as an MHA [23]. This

frequency-responsive dielectric medium is known as a Drude model, which implies the oscillation of free electrons in a good conductor. Therefore, the fact indicates that electric field vibrations in an MPA simulate plasmonic oscillations, so an MPA is also considered to be an SSPP-structure as well as an MHA. Based on the above discussion, the dispersion relation in an MPA is derived by assuming a surface wave formation on the boundary of an MPA, treated as a macroscopic medium. Since TM-polarized incident waves have only a y-component in the model, an amplitude with a z-dependency of H_y on the boundary between Region 1 and Region 2 can be expressed by the following formula with attenuation characteristics in each condition,

$$h(z) = \begin{cases} h_1 \exp(K_1 z) & z < 0 \\ h_2 \exp(-K_2 z) & z \geq 0 \end{cases}. \tag{2.16}$$

Here h_1 and h_2 are amplitudes of $h(z)$, and K_1 and K_2 are macroscopic propagation constants on the boundary. And by considering the wave equation of H_y, K_1 and K_2 can be derived as $K_1 = \sqrt{k_x'^2 - \omega^2 \epsilon_0 \mu_0}$, $K_2 = \sqrt{-\omega^2 \epsilon_\mathrm{r} \mu_\mathrm{r} \epsilon_0 \mu_0}$. In this derivation, it should be noticed that, since the waves cannot propagate in the x-direction when an MPA is treated as a macroscopic medium, the x-component of the wavenumber in Region 2 must be zero. And considering the boundary condition between Region 1 and Region 2, both tangential components of the magnetic field take the same value at $z = 0$, and the same is true for the electric field. That is

$$K_1 = -\frac{K_2}{\epsilon_\mathrm{r}}, \quad h_1 = h_2. \tag{2.17}$$

Eq. (2.17) is often called the generation condition of a surface plasmon polariton. With the use of the above definitions of K_1 and K_2 and expression (2.15), an SSPP-dispersion relation in an MPA is obtained by squaring Eq. (2.17),

$$k_{||}{}^2 c_0{}^2 = \omega^2 + \frac{\omega^4}{\omega_{\mathrm{p}}^2 - \omega^2} \frac{256a^2(d-a)^2}{\pi^4 d^4}. \tag{2.18}$$

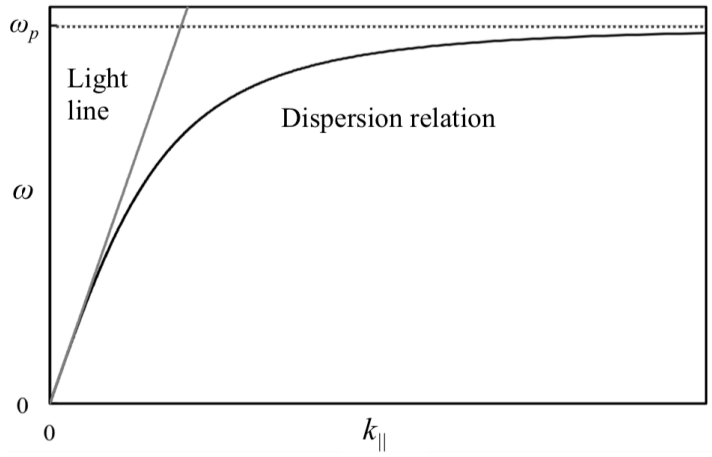

Figure 2.5: Ideal SSPP-dispersion relation in metal plate array.

Note that k'_x is replaced by $k_{||}$ in the derivation of Eq. (2.18). The curve is shown in Fig. 2.5, and it confirms the similarity of this curve and that of an MHA [23, 29]. Therefore, an MPA is considered to be formed SSPP-modes and shows the phenomenon of an extraordinary transmission as well as an MHA. Here, it is also known that this curve does not intersect with a light line since lattice scattering effects are not taken into account for the curve. If the effects are introduced into the curve, the wavenumber of $k_{||}$ in it has to be replaced with

$$k'_{||} = k_{||} \pm n|\boldsymbol{G}_x| \pm m|\boldsymbol{G}_y|, \quad |\boldsymbol{G}_x| = |\boldsymbol{G}_y| = \frac{\pi}{d}. \tag{2.19}$$

Note that $k'_{||}$ is the wavenumber of an SSPP with scattering effects, n and m are positive integers, and $\boldsymbol{G}_x$ and $\boldsymbol{G}_y$ are the reciprocal lattice vectors in the x-direction and y-directions, respectively. The SSPP-dispersion relation in an MPA with the scattering effects is shown in Fig. 2.6, which shows that the curve intersects a light line at several points. SSPP-modes are formed at those points, and the frequencies are considered to be resonant frequencies of SSPPs. The dispersion relation also shows that the MPA

has band-pass effects caused by extraordinary transmission as in the case of an MHA. Thus, an MPA acts as a band-pass filter if it is thick enough to be regarded as an SSPP-structure, and also acts as a band-stop filter, if the MPA is thin enough to be regarded as a kind of FSS. The above discussion supports the possibility that an MPA can be changed from a band-stop filter to a band-pass filter as its thickness is increased. This indicates that the breakdown of Babinet's principle, since an MHA shows band-pass effects regardless of its thickness and an MPA is a complementary structure to an MHA.

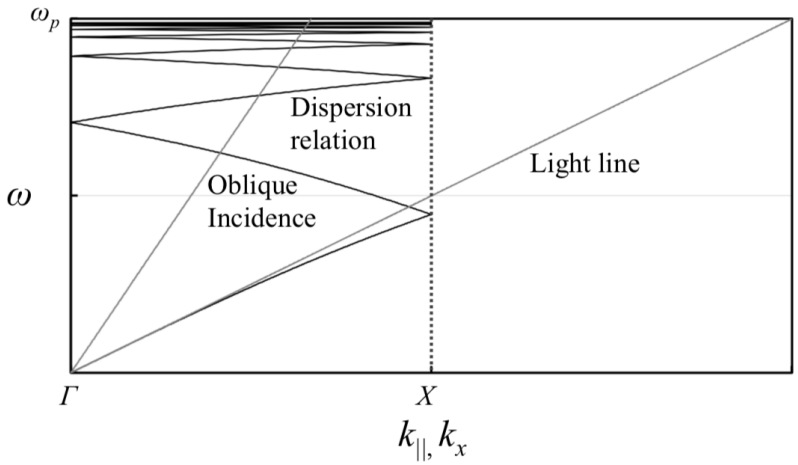

Figure 2.6: An actual SSPP-dispersion relation in a metal plate array and light line at normal incidence and oblique incidence.

2.3 Analytical Comparison of Metal Plate Array and Metal Hole Array in Frequency Dependencies

In this section, the breakdown of Babinet's principle is confirmed by using MPAs and MHAs in electromagnetic numerical analyses. According to the discussion in the previous section, the two complementary structures, MPAs and MHAs should show different tendencies in their electromagnetic profiles such as transmittance of incident waves if their thicknesses are varied sufficiently. That is, an MPA should shows a change from band-stop effects to band-pass effects as its thickness increases; on the other hand, an MHA should consistently show band-pass effects regardless of its thickness. To examine the above conclusions, the two models of an MPA and an MHA are provided as shown in

Fig. 2.7. Note that the size of the MPA's unit cell is $a \times a \times w$ and the MPA unit cell is two-dimensionally arranged infinitely with a period d, and an MHA's holes are centered in an unit cell with of size of $a \times a \times w$, and the MHA unit cell is two-dimensionally arranged infinitely with a period d. Waves of 60 - 100 GHz are introduced in the two models in a y-z direction, which has an incident angle θ. Transmission characteristics of the two models are analyzed with variations of their thickness w in a range of 0.01 mm - 3 mm. Here, the analyses are conducted by using an electromagnetic simulator (HFSS R19, Ansys, Canonsburg, PA, USA) and the values of a and d are fixed as (a, d) = (2 mm, 3 mm) in the analyses. The transmittance results for the MPA and the MHA are shown in Figs. 2.8 and 2.9, respectively.

The results in Fig. 2.8 confirm the change of transmission characteristics in the MPA from band-stop effects to band-pass effects. In the cases of 0.01 mm and 0.1 mm, the results show that the MPA possesses band-stop effects because the structure is much thinner than the incident wavelengths, and the MPA is considered to act as an FSS. On the other hand, in the case of 1 mm and 3 mm, the MPA possesses band-pass effects since the MPA has a thickness similar to the incident wavelengths and is considered to act as an SSPP-structure. The results also show the shift of resonant frequencies in all the cases, with the reason considered to be related to the change of propagation models. Specifically, the shift in the two thick cases is larger than that in the thin cases, although the ratio of the increase in thickness in the thick cases is smaller than that in the thin cases, thus indicating that the frequency-shift is sensitive to the ratio of the thickness and the wavelength. From the discussion, the facts support the above assumption, since the shift is related to the MPA-thickness.

On the other hand, the results in Fig. 2.9 confirm that the MHA consistently shows the same transmission characteristics, with band-pass effects in all the cases. In the thin cases of 0.01 mm and 0.1 mm, the MHA shows band-pass effects, as it is considered to act as an FSS with parallel resonant circuits [19,21]. Also, in the thick cases of 1 mm and 3 mm, the MHA shows band-pass effects, as it is considered to act as an SSPP-structure. Specifically, the result in the thick case of 3 mm shows almost perfect transmittance in the two bands, while other results do not show this phenomenon. The reason is

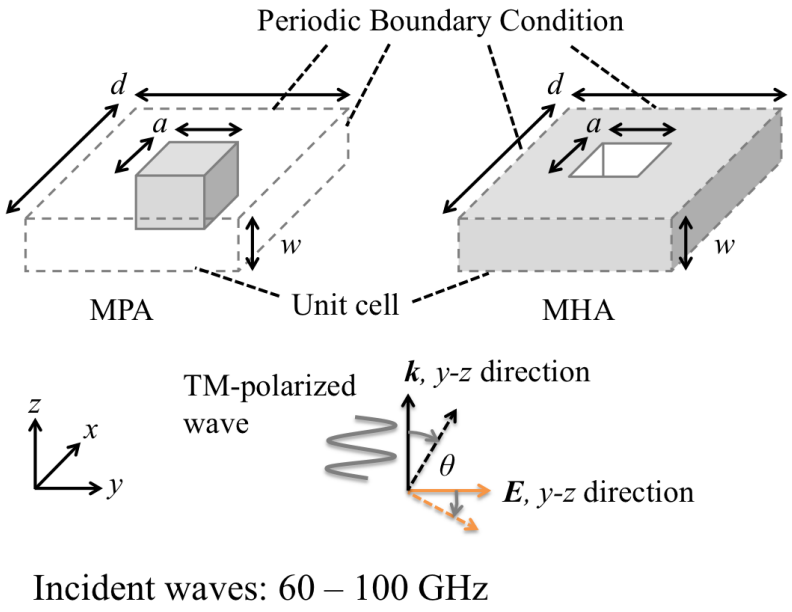

Figure 2.7: Analytical model of metal plate array and metal hole array for comparing their transmittances.

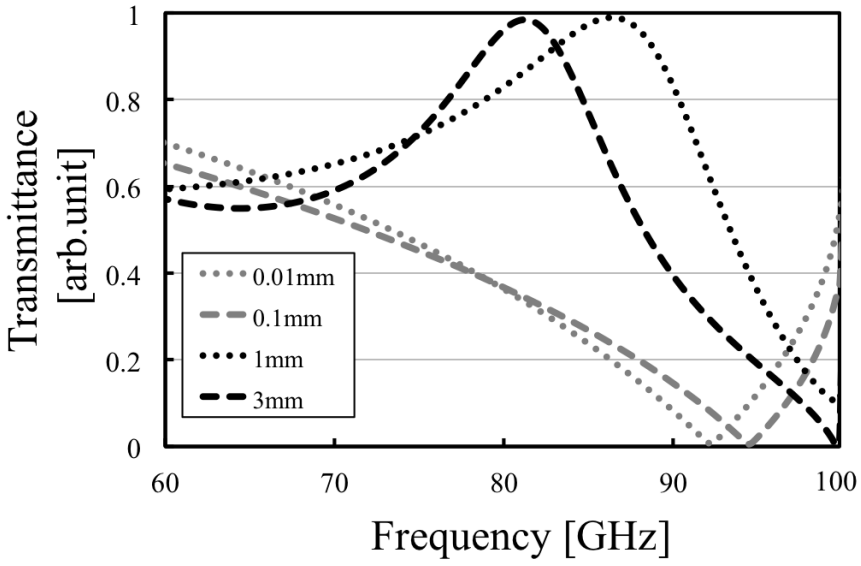

Figure 2.8: Thickness dependency of transmission characteristics in the case of the metal plate array.

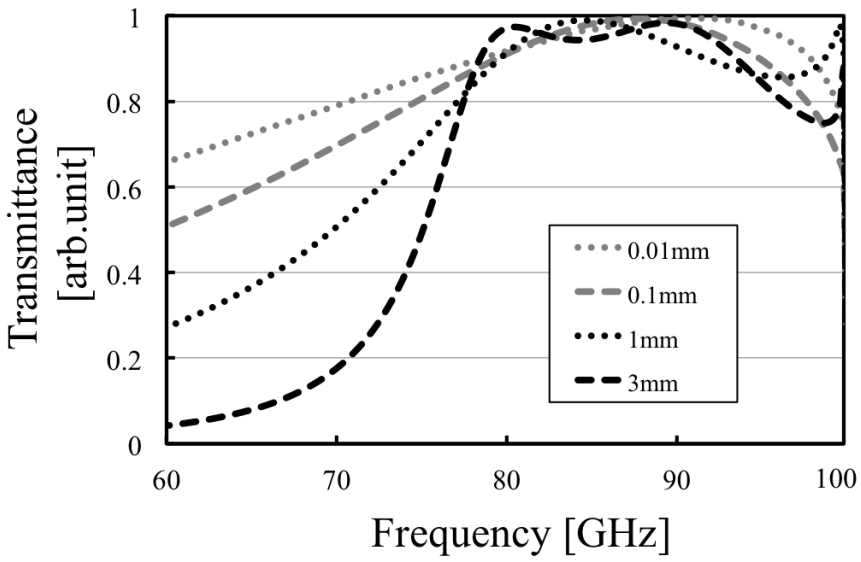

Figure 2.9: Thickness dependency of transmission characteristics in the case of the metal hole array.

considered to be related to the change of the propagation model in the MHA because if it acts as an FSS, its geometric configuration cannot have such characteristics in the adjacent frequency bands. In contrast, if it acts as an SSPP-structure, its geometric configuration can possess such characteristics in the adjacent frequency bands because the intersection of the light line and the SSPP-dispersion relation appears at multiple points, which indicate resonant conditions. Although these points are not certain to be appeared in real events, the SSPP structure has the potential of having multiple resonant frequencies. From the discussions, the facts support the above assumption since the thin cases do not have multiple resonant frequencies and one of the thick cases shows multiple resonances.

Next, the angular dependency of their transmission characteristics is investigated by varying values of θ and their thickness, in the thin (0.01 mm)and thick (3 mm) cases. The results in the four cases are shown in Figs. 2.10 - 2.13, respectively.

In Figs. 2.10 and 2.11, the two results confirm that both MPAs have several band-gap modes that vary in accordance with incident angles. However, the behavior of these modes differs; for example, there is no frequency distribution of the transmittance between the adjacent band gaps in the thin case (Fig. 2.10). On the other hand, there

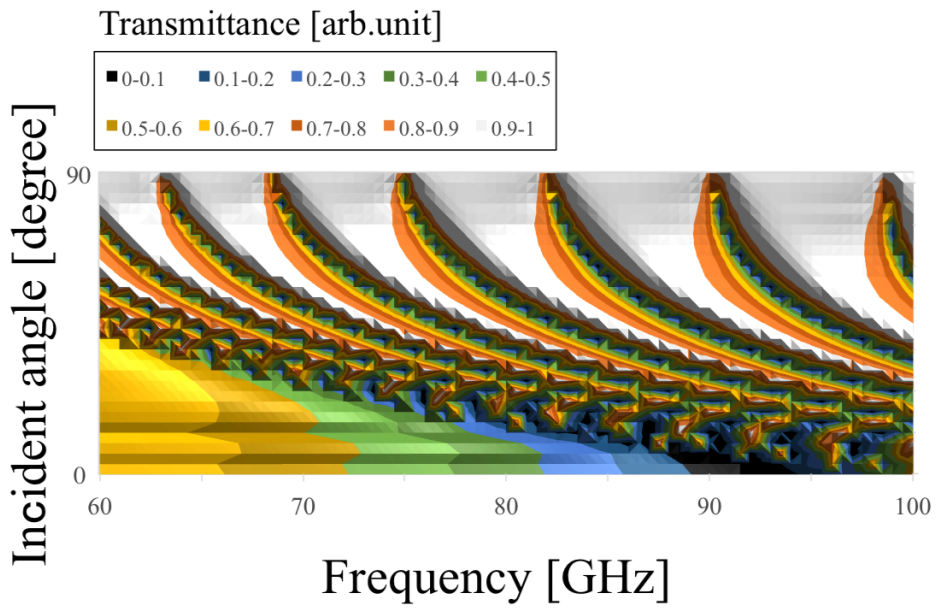

Figure 2.10: Angular dependency of transmission characteristics in the case of the metal plate array with a thickness of 0.01 mm.

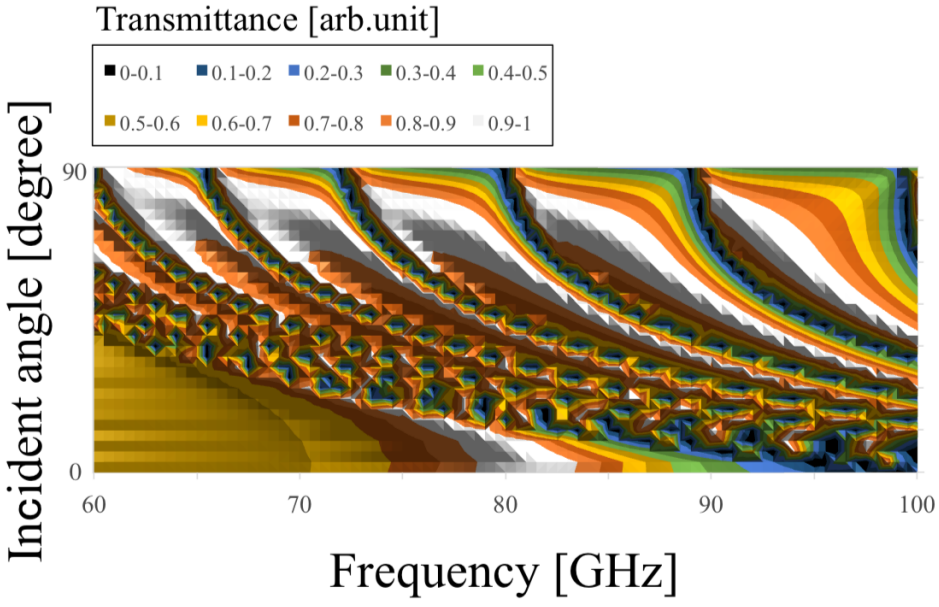

Figure 2.11: Angular dependency of transmission characteristics in the case of the metal plate array with a thickness of 3 mm.

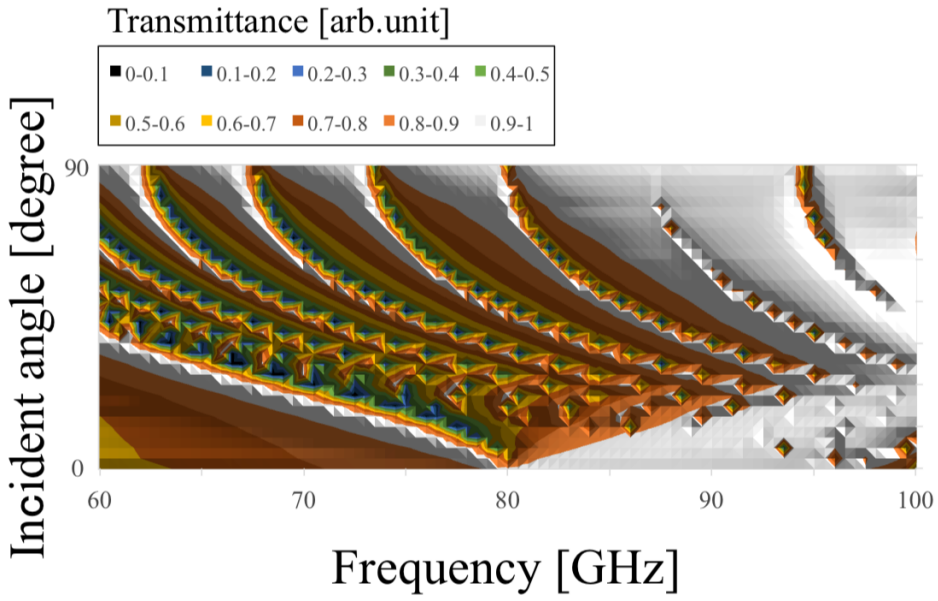

Figure 2.12: Angular dependency of transmission characteristics in the case of the metal hole array with a thickness of 0.01 mm.

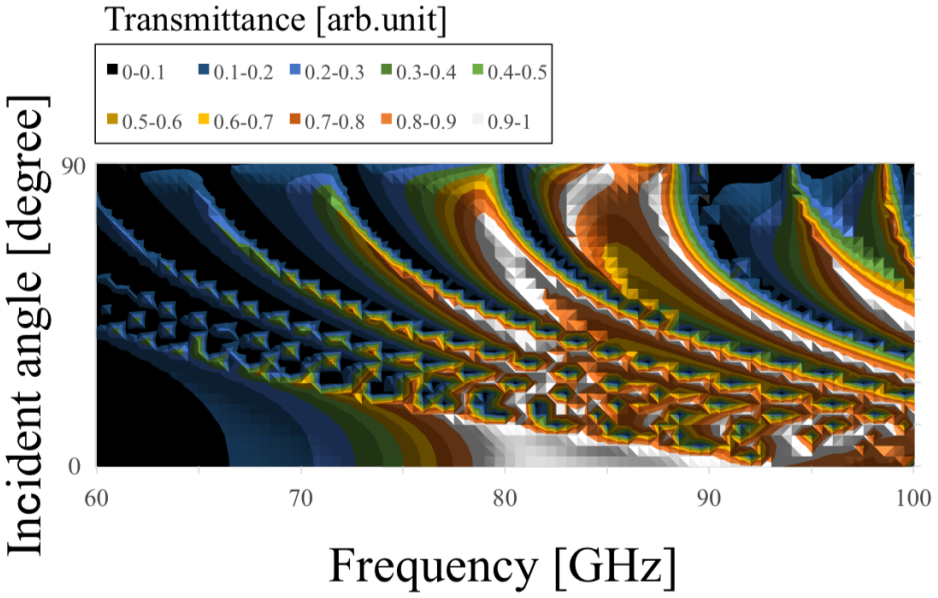

Figure 2.13: Angular dependency of transmission characteristics in the case of the metal hole array with a thickness of 3 mm.

are frequency distributions of the transmittance between the adjacent band gaps in the thick case (Fig. 2.11). These facts indicate different propagation modes in the two cases. Furthermore, comparing the two frequency characteristics at around 90 degrees, it is found that there are strong transmission regions in the thin cases although there are almost no strong transmission regions in the thick case. The reason is considered to be that in the thin case, propagation waves treat the MPA as a boundary so that transmission waves are formed by each scattered wave from each unit cell though incident waves have no vertical components of the wave vector. In contrast, in the thick case, since propagation waves treat the MPA as periodically arranged waveguides, transmission waves are considered effectively not to be formed, as incident waves hardly have any vertical components of their wave vector.

In Figs. 2.12 and 2.13, as well as the results for the MPAs, these results also confirm the difference of frequency distribution of the transmittance between the adjacent modes of the two angular dependencies. This fact shows the difference of the propagation modes between the thin case (Fig. 2.12) and thick case (Fig. 2.13). However, it can be seen that the modes in the thick case are band-pass modes, while the modes in the thin case are band-gap modes. This result shows the characteristics of propagation modes in a square waveguide which has limited higher-order modes, although a parallel plate waveguide has unlimited higher modes. In other words, the difference of the modes between the thick MPA and the thick MHA is originates in the difference of transmission-band percentage in the entire frequency band. In the discussions, the differences of the propagation modes between the thin and thick cases in both structures are confirmed for the two structures. These results indicate that the modes in the thin cases are determined by the boundary with frequency responses and that those in the thick cases are supported by the waveguide modes of MPAs and MHAs.

2.4 Experimental Demonstration of The Breakdown of Babinet's Principle Using Metal Plate Arrays and Metal Hole Arrays

To experimentally validate the situations described in Section II experimentally, the measurement system shown in Fig. 2.14 was used. In this system, MPAs and MHAs, the pair of complimentary SSPP structures, are used as samples to show the breakdown of Babinet's principle by comparing the transmission characteristics of the complementary structures. The experimental setup is very similar to that in our previous report [34,35], which is briefly reviewed below. The horn antennae are used as a transmitter and a receiver. The transmitted signals, the frequencies of which vary continuously from 60 GHz to 95 GHz continuously in time are detected by the oscilloscope as a time waveform which shows the frequency characteristics of the transmitted waves. By comparing the measured results in the cases with and without the sample, the transmission characteristics are obtained.

The samples used in the experiments are shown in Fig. 2.15. Samples of (a) and (b) are the thin and thick MPAs on PET substrates, and the conducive parts of sample (a) are silver ink which is printed on the substrate. The thickness of the ink and the substrate are 1.3 μm and 0.125 mm. The unit cell of the conductor parts is a square (2 mm $\times$ 2 mm) with a period of 3 mm. The unit cell of (b) has rectangular-shaped copper conductors (2 mm $\times$ 2 mm $\times$ 3 mm) that are arranged two-dimensionally with a period 3 mm, and the frame is made of the silver ink. Samples (c) and (d) are the thin and thick MHAs; (c) is also made of the silver ink, and its unit cell has a square aperture (2 mm $\times$ 2 mm) with a period of 3mm. Sample (d) is made of a stainless steel 3 mm thick, and its unit cell has a square aperture (2 mm $\times$ 2 mm) with period 3 mm. The experimental results with these MPAs and the MHAs are shown in Figs. 2.16 and 2.17, respectively.

In Fig. 2.16, the result confirms the difference of the transmission characteristics between the thin and thick MPAs. Consideration together with the analytical results shown in Fig. 2.8 shows that the thin MPA has a band-stop effect around 88 GHz, which

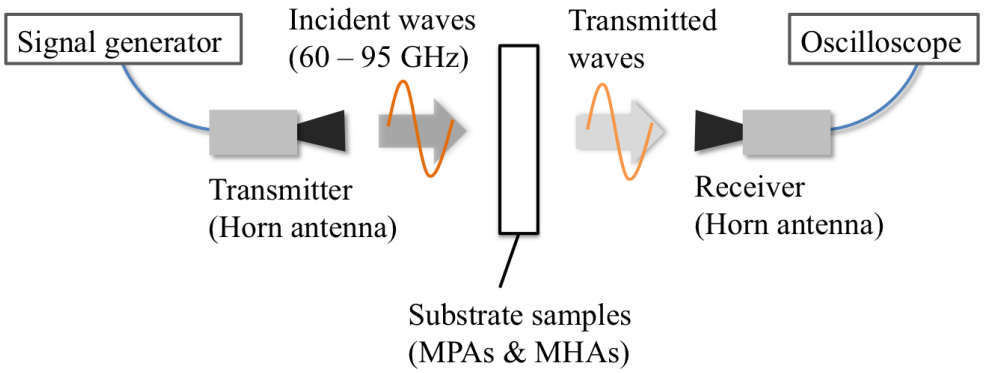

Figure 2.14: Measurement system.

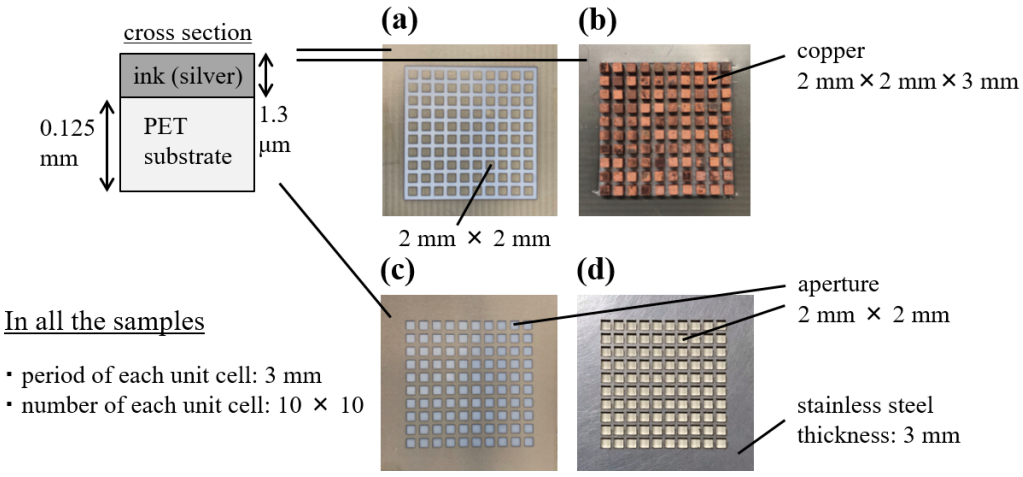

Figure 2.15: Experimental samples of MPAs and MHAs; (a) a sample of MPA with a thickness of 1.3 μm made of silver ink, (b) a sample of MPA with a thickness of 3 mm made of copper blocks, (c) a sample of MHA with a thickness of 1.3 μm made of silver ink, (d) a sample of MHA with a thickness of 3 mm made of stainless steel.

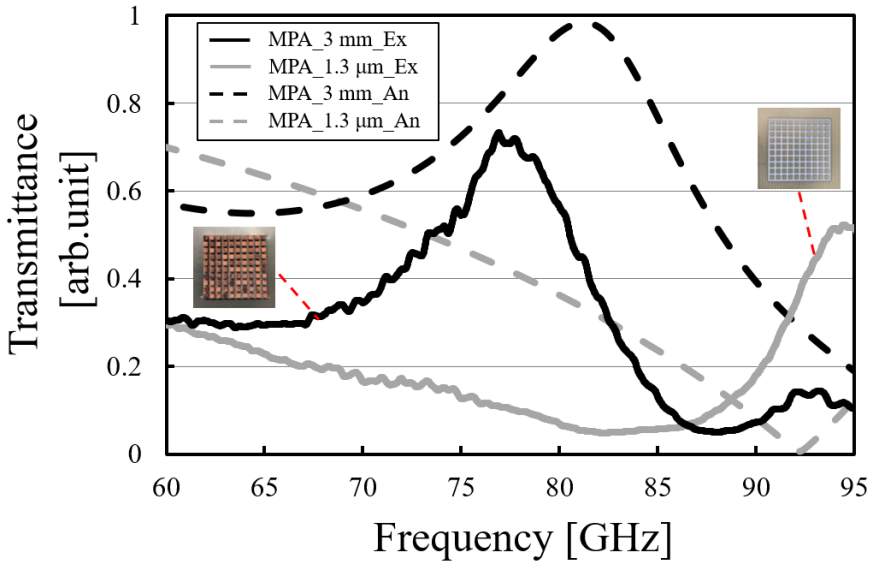

Figure 2.16: Thickness dependency of transmission characteristics in the thin and thick cases of the metal plate array (solid lines), compared to the corresponding analytical results (dotted lines).

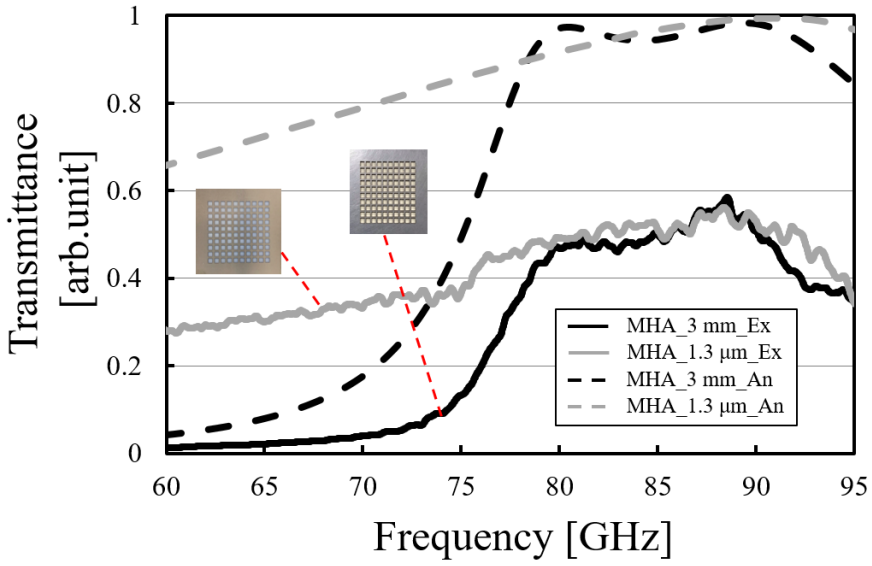

Figure 2.17: Thickness dependency of transmission characteristics in the thin and thick cases of the metal hole array (solid lines), compared to the corresponding analytical results (dotted lines).

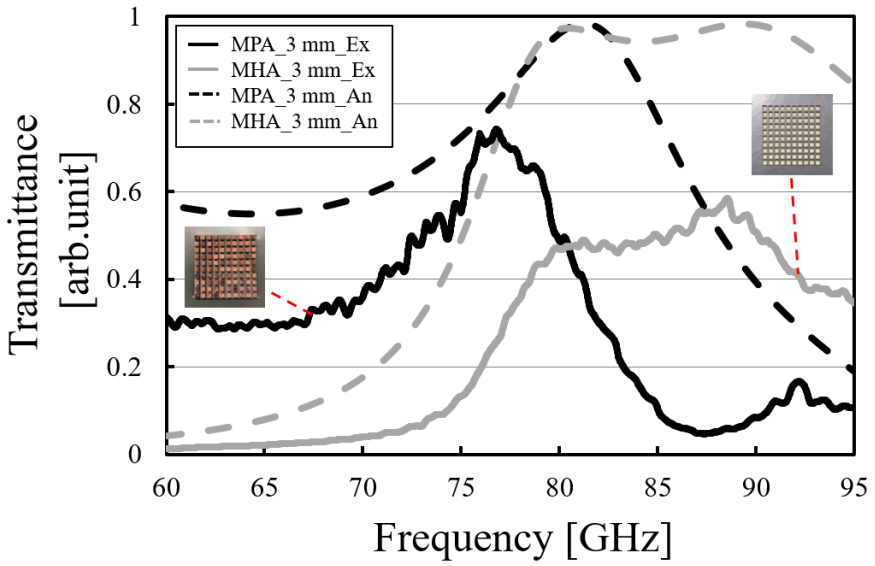

Figure 2.18: Experimental demonstration of the breakdown of Babinet's principle using the complimentary structures (MPAs and MHAs) with a wavelength-size thickness.

originates in a functional impedance surface based on its equivalent circuit model. In contrast, the thick MPA has a band-pass effect around 77 GHz caused by the excitation of the SSPP modes. Furthermore, since the two samples were fabricated by using the PET substrates, which have a higher relative permittivity, the experimental resonant frequencies are considered to be slightly lower than those of the analytical results, and the same can be said for their values of transmittance. However, the experimental results are consistent with the corresponding analytical results from the viewpoint of the tendency of the frequency responses. In Fig. 2.17, as opposed to the MPA cases, the results shows the invariance of the transmission characteristics with the band-pass effect between the thin and thick MHAs around 88 GHz in both cases. And they are also consistent with the corresponding analytical results from the viewpoint of the tendency of the frequency responses. Also, as well as the above MPA cases, the resonant frequency and the transmittance of the thin case are considered to be lower than those of the analytical results due to the effect of the PET substrates. The transmittance of the thick case is considered to be lower than that of the analytical results because of the loss due to the thick conductive substrate. Since the result of the thin case shows a band-pass effect, considered together with the above MPA results, this fact also supports the

idea that the two thin models can be considered to be based on the impedance surface theory with lumped elements, and they follow Babinet's principle. Also, as well as the above discussion of the thin case, the fact that the results of the two thick cases confirm band-pass effects also supports the idea that the two thick structures excite the resonant modes originating from each SSPP mode.

Finally, the breakdown of Babinet's principle is demonstrated by the analytical and experimental results of the thick cases in Fig. 2.18. The results confirm that the complimentary structures (with the same 3 mm thickness) show the same transmission characteristics of band-pass effects. If the results are in accordance with the principle, the MPA results and the MHA results must respectively show opposite characteristics, such as band-pass and band-stop effects. This study provides the new physical insight that the principle, based on the symmetry of the physical behaviors of electric fields and magnetic fields, can be applied to the electromagnetic structure only when the complimentary structures used can be treated as boundaries.

2.5 Conclusions

The breakdown of Babinet's principle was discussed and examined with the use of complementary SSPP structures, MPAs and MHAs. First, SSPP mode formation on an MPA was introduced by theoretically deriving the effective relative permittivity with a Drude-type frequency response and the SSPP dispersion relation on an MPA following Pendry's theory of SSPPs in the case of an MHA.

In the electromagnetic numerical analyses, the thickness dependencies of the transmission characteristics in the case of MPAs and MHAs were discussed. The analytical results confirmed that the characteristics of the MPA changed from band-stop to band-pass as its thickness increased. On the other hand, with MHAs, all the cases showed band-pass features regardless of thickness. From the angular dependencies of the MPAs and the MHAs, the their resonant mechanisms in the thin and thick cases were considered to be based on an impedance surface model with lumped elements used for frequency selective surfaces (FSSs) and the SSPP theory, respectively.

In the experiments, thin and thick models of MPAs and MHAs with the same size as

the analytical models were provided and their transmission characteristics investigated. The results also showed the same tendencies as the analytical results. Finally, the breakdown of Babinet's principle was demonstrated experimentally by using the thick models of the MPA and the MHA, and this fact gives us the new physical insight that the principle can be applied to the electromagnetic structure only on the premise that the complimentary structures used can be treated as boundaries.

References

[1] J. B. Pendry, Phys. Rev. Lett. **85**, 3966 (2000).

[2] R. A. Shalby, D. R. Smith and S. Schultz, Science **292**, 77 (2001).

[3] L. Zhang, Y. Zhang, L. He, H. Li, and H. Chen, Phys. Rev. E **74**, 056615 (2006).

[4] A. Sanada, C. Caloz, and T. Itoh, IEEE Trans. Microwave Theory Tech. **52**, 1252 (2004).

[5] G. V. Eleftheriades, A. K. Iyer, and P. C. Kremer, IEEE Trans. Microwave Theory Tech. **50**, 2702 (2002).

[6] J. T. Costa, and M. G. Silveirinha, Phys. Rev. B **84**, 155131 (2011).

[7] B. I. Popa, and S. A. Commer, Phys. Rev. B **85**, 205101 (2012).

[8] S. Tomita, K. Sawada, S. Nagai, A. Sanada, N. Hisamoto, and T. Ueda, Phys. Rev. B **96**, 165425 (2017).

[9] H. Tao, A. C. Strikwerda, K. Fan, W. J. Padilla, X. Zhang, and R. D. Averitt, Phys. Rev. Lett. **103**, 147401 (2009).

[10] I. V. Shadrivov, P. V. Kapitanova, S. I. Maslovski, and Y. S. Kivshav, Phys. Rev. Lett. **109**, 083902 (2012).

[11] F. Bayatpur, and K. Sarabandi, IEEE Trans. Microwave Theory Tech. **56**, 2742 (2008).

[12] F. Falcone, T. Lopetegi, M. A. G. Laso, J. D. Baena, J. Bonache, M. Beruete, R. marques, F. Martin, and M. Sorolla, Phys. Rev. Lett. **93**, 197401 (2004).

[13] J. Persons, E. Hendry, C. P. Burrows, B. Auguie, J. R. Sambles, and W. L. Barnes, Phys. Rev. B **79**, 073412 (2009).

[14] L. Zhang, T. Koschly, and C. M. Soukoulis, Phys. Rev. B **87**, 045101 (2013).

[15] G. Pelosi, and S. Selleri, IEEE Antennas Propag. Magazine **59**, 144 (2017).

[16] A. Bitzer, A. Ortner, H. Merbold, T. Feurer, and M. Walther, Opt. Exp. **19**, 2537 (2011).

[17] F. Mesa, R. R. Berral, F. Medina, IEEE Mirow. Magazine **19**, 44 (2018).

[18] M. Z. Joozdani, and M. K. Amirhosseini, IEEE Trans. Antennas Propag. **65**, 705 (2017).

[19] K. Sarabandi, and N. Behdad, IEEE Trans. Antennas Propag. **55**, 1239 (2007).

[20] M. Yan, S. Qu, J. Wang, J. Zhang, H. Zhou, H. Chen, and L. Zhang, IEEE Antennas Wireless Propag. Lett. **13**, 895 (2014).

[21] B. A. Munk, $FrequencySelectiveSurfaces : TheoryandDesign$ (Wiley, New York, 2000).

[22] G. Itami, Y. Toriumi, and J. Kato, IEEE Trans. Antennas Propag. **67**, 7407 (2019).

[23] J. B. Pendry, L. M. Moreno, and F. J. G. Vidal, Science **305**, 847 (2004).

[24] F. Miyamaru and M. Hangyo, Phys. Rev. **71**, 165408 (2005).

[25] F. Miyamaru, S. Hayashi C. Otani, and K. Kawase, Opt. Lett. **31**, 1118 (2006).

[26] F. Miyamaru, M. Kamijyo, N. Hanaoka, and M. W. Takeda, App. Phys. Lett. **100**, 081112 (2012).

[27] F. Miyamaru and M. Hangyo, App. Phys. Lett. **84**, 2742 (2004).

[28] F. Miyamaru, M. Tanaka, and M. Hangyo, Phys. Rev. B **74**, 153416 (2006).

[29] F. J. G. Vidal, L. M. Moreno, and J. B. Pendry, J. Opt. A: Pure Appl. Opt. **7**, S97 (2005).

[30] J. Y. Yin, D. Bao, J. Ren, H. C. Zhang, B. C. Pan, Y. Fan, and T. J. Cui, IEEE Antennas Wireless Propag. Lett. **16**, 597 (2017).

[31] S. J. Berry, T. Campbell, A. P. Hibbins, and J. R. Sambles, App. Phys. Lett. **100**, 101107 (2012).

[32] S. A. Maier, S. R. Andrews, L. M. Moreno, and F. J. G. Vidal, Phys. Rev. Lett. **97**, 178605 (2006).

[33] M. J. Lockyear, A. P. Hibbins, and J. R. Sambles, Phys. Rev. Lett. **102**, 073901 (2009).

[34] G. Itami, O. Sakai, and Y. Harada, Electronics **8**, 239 (2019).

[35] G. Itami and O. Sakai, J. Appl. Phys. **125**, 213101 (2019).

[36] T. W. Ebbesen, H. J. Lezac, H. F. Ghaemi, T. Thio, and P. A. Wolff, Nature (London) **391**, 667 (1998).

[37] F. Medina, F. Mesa, R. Marques, IEEE Trans. Microwave Theory Tech. **56**, 3108 (2008).

[38] H. F. Ma, B. G. Cai, T. X. Zhang, Y. Yang, W. Xiang, and T. J. Cui, IEEE Trans. Antennas Propag. **61**, 2561 (2013).

[39] Y. Han, Y. Li, H. Ma, J. Wang, D. Feng, S. Qu, and J. Zhang, IEEE Trans. Antennas Propag. **65**, 1187 (2017).

[40] P. Yan, and A. Alu, Phys. Rev. B **82**, 235405 (2010).

[41] D. R. Smith, J. J. Mock, A. F. starr, and D. Schurig, Phys. Rev. E **71**, 063609 (2005).

Chapter 3

Symmetrical estimation method for skin depth control of spoof surface plasmon polaritons using dispersed waves from a metallic hole array

3.1 Introduction

Electromagnetic surface waves can propagate on the interface between two media with permittivities of the opposite sign, such as a plasma–dielectric interface [1–5] or a metal–air or metal–dielectric interface. [6–12] In this phenomenon, the electric fields of the waves are localized in the interface and attenuate exponentially with distance. Surface waves can propagate only on such boundaries, since these waves are supported by oscillations of free electrons.

It is well known that in the case of a metal–air interface, such waves (surface plasmon polaritons, SPPs) can be excited on the metal surface in the optical range. Recently, however, a similar wave propagation phenomenon has been predicted in the microwave range under certain conditions [13] and has been investigated in a number of studies

using metals with a periodic structure. [14–24] This wave phenomenon is called a spoof surface plasmon polariton (SSPP), [25–32] and its propagation characteristics are similar to those of an SPP. Among the structures for which SSPP modes can be excited are metallic hole arrays (MHAs), which are conductive plates with two-dimensional periodic structures of sub-wavelength holes and which are members of a wider class of so-called metamaterials. [25–27, 33–35]

MHAs have a macroscopic negative permittivity, as can be shown analytically by an integration technique devised specifically for metamaterials. If it is assumed that metals are perfect conductors at frequencies lower than the infrared, the resonant frequencies of MHAs and the wave propagation ranges can be controlled by varying the spatial periodicity and size of the holes. Extraordinary transmission rates of up to 100% have been observed in MHAs, and it has been found that dynamic tuning of the frequency of this extraordinary transmission is possible. [33, 34, 36, 37]

One of the key issues in optical wave propagation, namely, controllability of skin depth, has recently attracted much attention [38–40] owing to its importance for the design of plasmonic devices, as well as its relevance to the spatial resolution of optical instruments. [7] It is possible to regulate the skin depth by forming a waveguide-like cladding structure that induces anisotropy in the boundary between dielectric substrates, allowing the skin depth of evanescent waves to be decreased outside the core region. [38]

As well as the waveguide properties of these spatial configurations, SSPP modes exhibit anisotropic features and field leakage behavior similar to that of the skin depth, and the electric fields of these modes exhibit exponential attenuation with respect to structural parameters. [30] The relation between the structural parameters of MHAs and the skin depth of the SSPP modes that they generate has been investigated both theoretically and analytically. It has also been shown that the skin depths of SSPP modes have values of order of the wavelength. [30, 31, 41] According to numerical simulations, SSPP modes are generated symmetrically on both sides of an MHA interface when waves are incident from free space at an appropriate frequency, [41] as shown in Fig. 3.1, a feature that is not shared by cladding structures. However, there is as yet no experimental evidence for such symmetric field patterns.

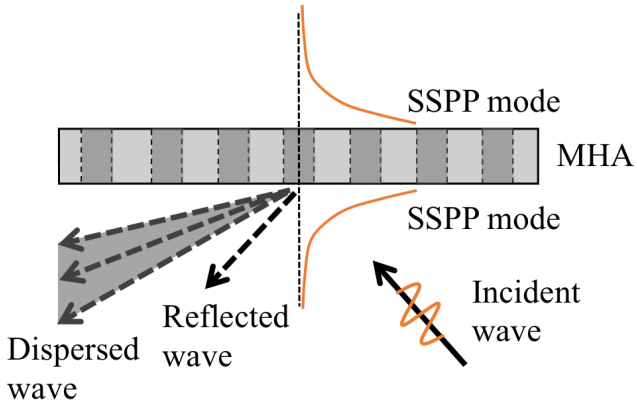

Figure 3.1: Symmetrical generation of SSPP modes on an MHA.

In this study, we propose a symmetrical estimation method for SSPP skin depth that furthermore allows determination of the electromagnetic properties of dielectric media on an MHA using the estimated skin depth. Since an SSPP is supported by the surface morphology of the periodic microstructure of an MHA, the electric fields have near-field components, but there should also be components of the propagating wave that are localized on the interface owing to the macroscopic spatial properties of the SSPP.

We report here an experimental study of the profiles of macroscopic electric fields on the surface of an MHA on which SSPPs propagate. By detecting signals reflected from a movable flat metal plate above the MHA, we obtain data on the scattering of millimeter waves obliquely incident on the MHA, and from this data we are able to determine the excitation frequencies of the SSPPs. We confirm the existence of dispersed waves on the incident side. Using these dispersed waves, the skin depths of the electric fields of SSPP waves can be measured experimentally, and we find that our measurements of the skin depth agree well with their theoretical values, indicating that the proposed method can be used for the investigation of unknown materials on a surface.

The remainder of this paper is organized as follows. In Sec. 3.2, we give a theoretical description of the generation of SSPPs by an MHA using the Maxwell equations and the dispersion relation for SSPPs given by Pendry *et al.*, [25] and we also propose a theoretical expression for the skin depth of the SSPP around the MHA. In Sec. 3.3, from the results of experiments using millimeter waves, the MHA, and a movable flat metal plate, we describe the characteristics of the MHA during SSPP excitation and the

detection of wave scattering signals related to the SSPPs around the MHA. In Sec. 3.4, we present our conclusions.

3.2 Theoretical Derivation of Skin Depth in SSPPs

To describe SSPP generation in a metallic sub-wavelength-hole array, we begin by introducing the electromagnetic model that describes the MHA and electromagnetic waves in the millimeter-wave range. In this model (Fig. 3.2), the MHA is regarded as a uniform effective medium whose effective permittivity responds to the frequency of incident waves. Millimeter waves incident at an appropriate frequency lead to a concentration of electric fields in and around an MHA with a square array (with period d) of square holes (with cross section $a \times b$ and depth w). Resonance of the waveguide modes inside the sub-wavelength holes and the incident wave modes generates a surface mode on the MHA.

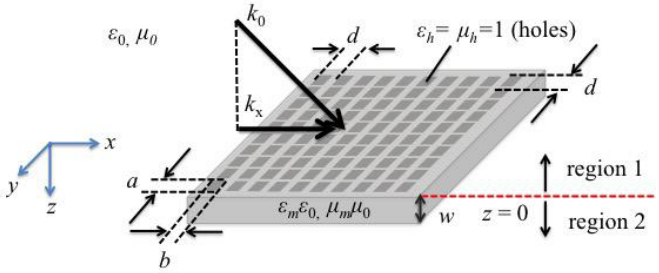

Figure 3.2: Schematic of the theoretical model for generation of SSPPs on an MHA.

First, we define the expression for the electric and magnetic fields in two regions: in the incident vacuum region (region 1) and inside the holes (region 2). We assume that the permittivity and permeability in these two regions are those of the vacuum, ϵ_0 and μ_0. In region 2, since the holes are not filled with dielectric material, the permittivity and permeability in a hole again correspond to those of vacuum, so their relative permittivity and permeability are $\epsilon_h = \mu_h = 1$. As described above, we regard the MHA as a uniform effective medium with macroscopic relative permittivity ϵ_m and macroscopic relative permeability μ_m based on the theoretical expressions of Pendry *et al.* [25] The relative

permittivity ϵ_m and relative permeability μ_m in region 2 have the following forms:

$$\epsilon_m = \frac{\pi^2 d^2}{8ab}\left(1 - \frac{\omega_p^2}{\omega^2}\right), \tag{3.1}$$

$$\omega_p = \frac{\pi c}{a}, \tag{3.2}$$

$$\mu_m = \frac{8ab}{\pi^2 d^2}. \tag{3.3}$$

The dispersion relation of the SSPPs is

$$k_{||}^2 c_0^2 = \omega^2 + \frac{\omega^4}{\omega_p^2 - \omega^2}\left(\frac{64a^2b^2}{\pi^4 d^4}\right), \tag{3.4}$$

where ω is the frequency of the incident waves, ω_p is the cutoff frequency of the holes in the MHA, and $k_{||}$ is the wavenumber of the SSPP. The x component of the permittivity tensor and the y component of the permeability tensor are related to the effective relative permittivity ϵ_m and effective relative permeability μ_m by $\epsilon_x = \epsilon_m \epsilon_0$ and $\mu_y = \mu_m \mu_0$, respectively. For simplicity, we assume that the material of the MHA is a perfect electrical conductor and that the fields have a time dependence $\sim \exp(\mathrm{j}\omega t)$, where $\mathrm{j} = \sqrt{-1}$. The dispersion relation of the SSPPs is shown in Fig. 3.3(a).

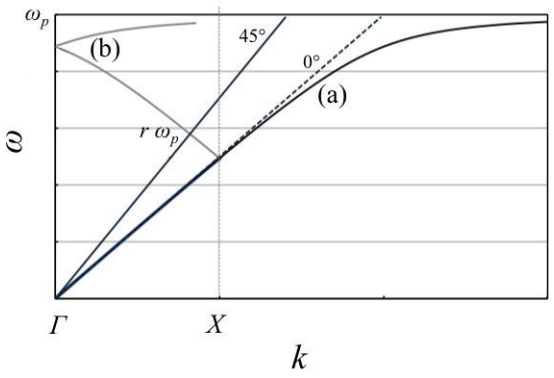

Figure 3.3: Dispersion relation: (a) SSPPs; (b) SSPPs in the case of lattice scattering, with account taken of spatial periodicity.

When ω is very close to ω_p, the group velocity of the SSPPs is almost 0, and localized waves are generated. However, since the curve does not intersect with a light line, no lattice scattering is found in Fig. 3.3(a). Therefore, the actual curve of the SSPPs is

different from the theoretical one. Hence, we introduce the effects of spatial periodicity into Eq. (3.4) via

$$\boldsymbol{k}_{\text{sspp}} = \boldsymbol{k}'_{||} = \boldsymbol{k}_{||} - i\boldsymbol{G}_x - j\boldsymbol{G}_y, \tag{3.5}$$

$$|\boldsymbol{G}_x| = |\boldsymbol{G}_y| = \frac{\pi}{d}, \tag{3.6}$$

where k_x is the x component of the wave vector of the electromagnetic wave, i and j are integers, and $\boldsymbol{G}_x$ and $\boldsymbol{G}_y$ are the reciprocal vectors of the square lattice in the x and y directions. In this study, we consider the two lowest scattering effects for the cases $(i, j) = (\pm 1, 0)$ and $(i, j) = (0, \pm 1)$, which correspond to the first Brillouin zone. The curve in Fig. 3.3(b) shows the dispersion relation with account taken of spatial periodicity. An SSPP occurs on the MHA at the point where the light line crosses the curve in Fig. 3.3(b).

The wave equation describing a magnetic field in a dielectric medium is

$$\nabla^2 \boldsymbol{H} = \epsilon_i \mu_i \frac{\partial^2 \boldsymbol{H}}{\partial t^2}, \tag{3.7}$$

where, in the present case,

$$(\epsilon_i, \mu_i) = \begin{cases} (\epsilon_0, \mu_0) & (z < 0), \\ (\epsilon_m \epsilon_0, \mu_m \mu_0) & (z \geq 0). \end{cases} \tag{3.8}$$

We consider TM-polarized incidence in Fig. 3.2, [26] with the magnetic field vector given by $\boldsymbol{H} = H_y[0, 1, 0]$. The y component H_y then satisfies

$$\left(\frac{\partial^2}{\partial x^2} + \frac{\partial^2}{\partial z^2}\right) H_y = -\omega^2 \epsilon_i \mu_i H_y. \tag{3.9}$$

Since the SSPPs are localized on the surface of the MHA, they propagate along the x direction (as defined by the incident TM-polarized waves [26]), attenuating at an exponential rate in the z direction. Therefore, H_y can be expressed as

$$H_y = h(z) \exp[\mathrm{j}(k_x x - \omega t)], \tag{3.10}$$

where $h(z)$ is the magnetic field amplitude, which depends on z, and k_x is the x component of the wave vector. Substituting Eq. (3.10) into Eq. (3.9), we obtain the following equation for $h(z)$:

$$\frac{\partial^2}{\partial z^2}h(z) = (k_x^2 - \omega^2\epsilon_i\mu_i)h(z). \tag{3.11}$$

In region 2 ($z \geq 0$), as z increases, the amplitude $h(z)$ decreases exponentially, and therefore the propagation constant of the wave in the z direction is purely imaginary. Since there are holes in region 2, the waves do not propagate in the x direction when each of the holes and the surrounding area are treated as a unit cell of a macroscopic medium. Therefore, $k_x = 0$ in region 2, and

$$\begin{aligned} h(z) &= h_2 \exp(-\beta_2 z), \\ \beta_2 &= \sqrt{-\omega^2\epsilon_m\mu_m\epsilon_0\mu_0}\,, \end{aligned} \tag{3.12}$$

where h_2 is a constant. From Eq. (3.12), we define the skin depth of the SSPP as $L = 1/\beta_2$. Since millimeter waves generally have millimeter-order skin depths, we have confirmed the order of the skin depth of the SSPP mode from these theoretical expressions. As described above, when the curve of the SSPP dispersion relation and the light line at any incident angle intersect, SSPPs will occur on the MHA at those points. In other words, the resonant frequency follows a light line. The skin depth L can be determined from the cutoff frequency ω_p, resonant frequency ω_{SSPP}, and light velocity c as follows:

$$\begin{aligned} L = \frac{1}{\beta_2} &= \frac{1}{\sqrt{-\omega_{\mathrm{SSPP}}^2\epsilon_m\mu_m\epsilon_0\mu_0}} \\ &= \frac{1}{\sqrt{-\left(1-\dfrac{\omega_p^2}{\omega_{\mathrm{SSPP}}^2}\right)\dfrac{\omega_{\mathrm{SSPP}}^2}{c^2}}} \\ &= \frac{c}{\sqrt{\omega_p^2-\omega_{\mathrm{SSPP}}^2}}, \end{aligned} \tag{3.13}$$

where ω_{SSPP} is the SSPP resonance frequency. Therefore, since ω_{SSPP} depends on the incident angle of the electromagnetic waves, so does L. If an SSPP mode in an MHA occurs at a point of intersection of the SSPP dispersion relation and a light line of any

incident angle up to the first folding in Fig. 3.3, then the resonant frequency is in the range $r \simeq 0.5$–0.8, with the exact value depending on the particular case. Note that the variable r here takes the role of a fitting parameter that varies from 0 to 1. From Eq. (3.13), the skin depth L takes values in the range $1.15c/\omega_p$ to $1.66c/\omega_p$. These values are obviously of the same order of magnitude as the incident wavelength. It is also found that the skin depth varies with the SSPP frequency as shown in Fig. 3.4. Note that the skin depth curve depends on the structural parameters of the MHA, since these determine the cutoff frequency.

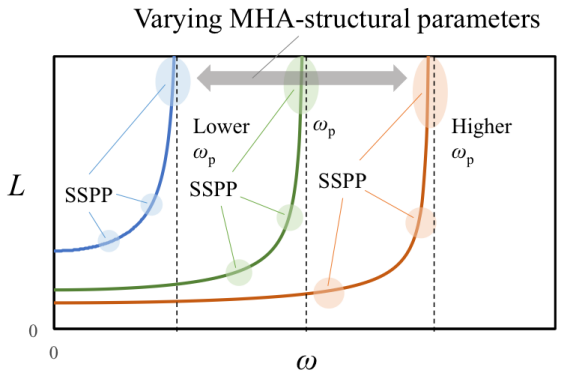

Figure 3.4: Relationship between skin depth and angular frequency of SSPP modes on an MHA.

3.3 Experimental Observation of SSPPs

3.3.1 Experimental setup

In this subsection, we describe the experimental system for investigating SSPPs on an MHA shown in Fig. 3.5. We use the MHA shown in Fig. 3.2 (in our experiments, $a = 1.5$ mm, $b = 2$ mm, $d = 3$ mm, and $w = 4$ mm), a conductive board made of phosphor bronze, transmitter and receiver antennae, a signal generator, and an oscilloscope. Waves of frequency 75–110 GHz arrive at the MHA with an incident angle θ_i from a transmitter antenna, and the reflected and dispersed waves are received at a detection angle θ_d. First, using the system without the conductive board, we investigated the SSPP frequency by detecting the signals of the reflected and dispersed waves. Then, with the conductive board in place, we used the reflected and dispersed waves to confirm the presence of

an electromagnetic field distribution with exponential attenuation around the SSPP frequency.

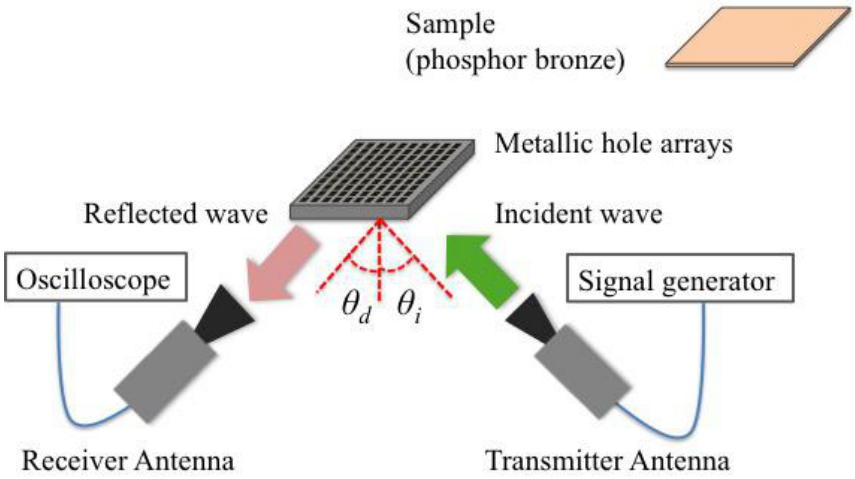

Figure 3.5: Experimental system for SSPPs on an MHA.

3.3.2 Detection of frequency spectra

We detected the reflected and dispersed signals from the MHA using a receiver antenna. The incident angle $\theta_i = 45°$, and we varied the detection angle θ_d from 35° to 45°. Note that since the turnover region from 45° to 55° can be considered to be equivalent to this range of θ_d for symmetrical radiation patterns of a reflector or an antenna, only one side was chosen for measurement. The experimental results are shown in Fig. 3.6.

We can roughly divide the wave signals into two types: reflected and dispersed. The former are detected around 45° and the latter from 39° to 43°. It can be seen that the frequency dependences of the two types of signals are remarkably different. Specifically, when the frequency exceeded about 103–105 GHz, the reflected wave intensity decreased rapidly, whereas the dispersed wave intensity increased rapidly. Thus, the propagation mode on the MHA changes at a frequency of about 103–105 GHz. Also, at this frequency, since the intensities of both reflected and dispersed waves are locally decreased, it can be assumed that there is an increase in the transmitted wave intensity and that this is due to the extraordinary transmittance that is characteristic of SSPPs.

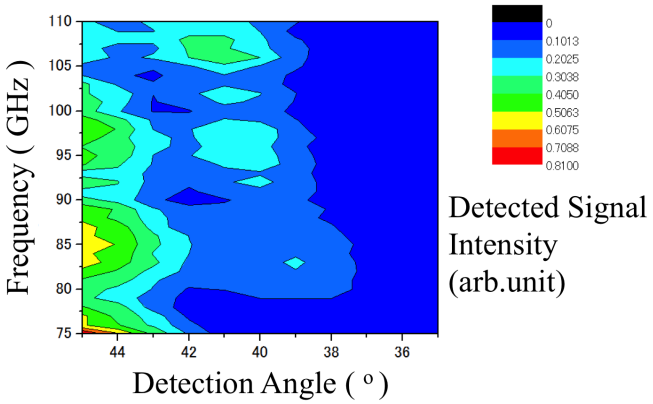

Figure 3.6: Dependence of reflected and dispersed signal intensity on detection angle.

3.3.3 Measurement of skin depth

Next we conducted a experiment to determine the sample-height dependence using our experimental system and the conductive board described in Sec. 3.3.1. As shown in Fig. 3.7, with TM incidence of electromagnetic waves of frequency 95–108 GHz, we varied the height of the board from 0.02 mm to 3 mm and detected the reflected and dispersed wave signals at the detection angles corresponding to each frequency. We detected reflected wave signals at 45° for all the frequencies used in this experiment. The experimental results are shown in Figs. 3.8–3.12.

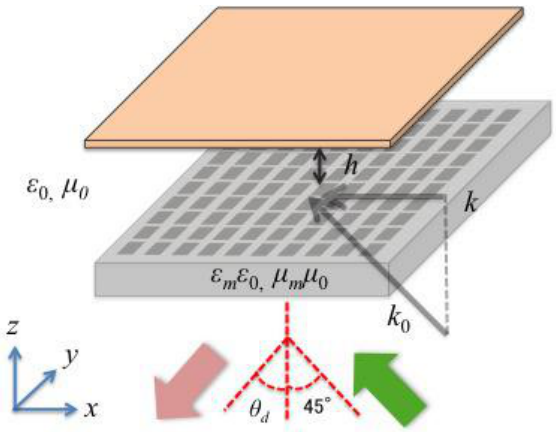

Figure 3.7: Schematic of experiment on sample-height dependence.

In Fig. 3.8, the 104 GHz and 108 GHz signals show attenuation characteristics at 0.02–0.5 mm. However, these signals differ in their electromagnetic characteristics. Since

the 108 GHz signals have a local maximum at 1 mm, and the 108 GHz detection intensities at 0.26 mm and 3.0 mm were nearly the same, it can be seen that the dependence has a periodicity at 108 GHz. This periodicity is related to the wavelength, since the wavelength at 108 GHz (2.8 mm) also nearly corresponds to the difference between 0.26 mm and 3.0 mm (2.74 mm). The periodicity is related to the wavelength generated by the transmitted waves of the waveguides in the MHA. Therefore, waves of 108 GHz are not considered to be related to the SSPP modes, although they exhibit similar attenuation characteristics. In addition, the 95 GHz signals have different attenuation characteristics from the 104 GHz waves.

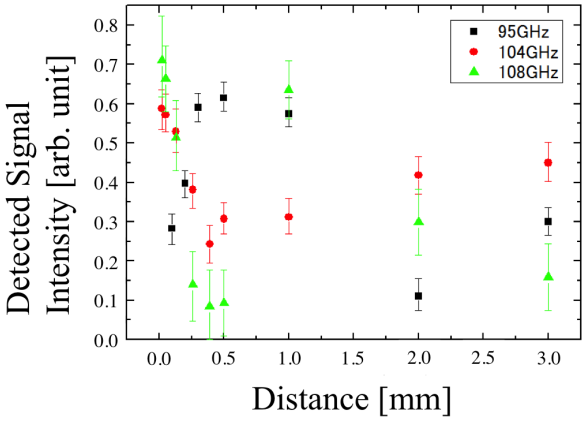

Figure 3.8: Sample-height dependence of dispersed wave signals at frequencies 95 GHz, 104 GHz, and 108 GHz at detection angles of 40°, 39.5°, and 42°, respectively.

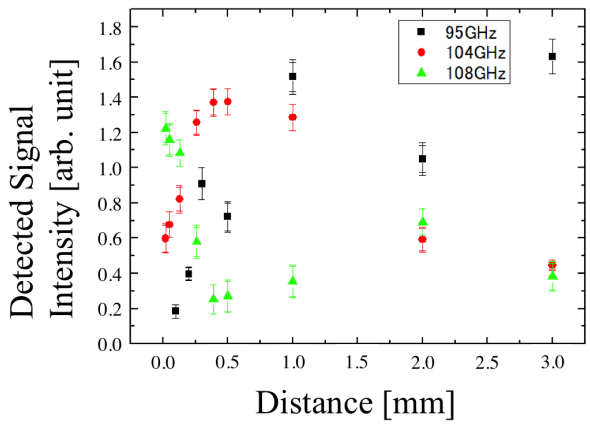

Figure 3.9: Sample-height dependence of reflected wave signals at frequencies 95, 104, and 108 GHz.

In Fig. 3.9, the 95 GHz signals resemble those in Fig. 3.8, so these signals can be considered to be propagating waves, which are not related to SSPP modes. The 108 GHz signals in Fig. 3.9 also have a periodicity related to their wavelength, like the signals in Fig. 3.8. Since the 108 GHz signals in Figs. 3.8 and 3.9 are similar, the dispersed wave signals at this frequency are not related to the SSPPs that are generated around the MHA. On the other hand, the 104 GHz signals in Fig. 3.9 are clearly different from the signals in Fig. 3.8, since the 104 GHz signals in the former do not exhibit attenuation characteristics.

From the above discussion, it can be seen that the dispersed wave signals at 104 GHz have the potential to reveal the skin depth of SSPP modes. Specifically, we have confirmed that the 104 GHz waves exhibit attenuation characteristics at 0.02–0.5 mm in the case of the dispersed wave detection, and this attenuation seems to be exponential. At 0.02 mm, the detected signal intensity at 104 GHz is approximately 0.6, and at 0.5 mm, it is approximately 0.3. Therefore, the dependence at 104 GHz can be considered to have a millimeter-order skin depth.

For further understanding of these matters, we compared the dependence at 104 GHz with those at the nearby frequencies of 103.5 GHz and 104.5 GHz in Figs. 3.10–3.12, from which it can be seen that the 103.5 GHz and 104.5 GHz waves also exhibit exponential attenuation characteristics like those of the 104 GHz waves. In Figs. 3.10–3.12, a curve is fitted to the experimental values, using a least squares method, with a yellow dotted line indicating the fitting area in each case. The experimental values of the skin depth at 103.5 GHz, 104 GHz, and 104.5 GHz are 0.283 mm, 0.422 mm, and 0.265 mm, respectively. We also compared the theoretical values of the skin depth at these frequencies using Eq. (3.13). These theoretical values are 0.327 mm, 0.328 mm, and 0.329 mm, respectively, and are in good agreement with the experimental values, with an average error of 20.5%. Note that in the calculations, we assumed that coupling occurred around the point by the first folding; in this study, we confirmed $r = 0.58$ in Fig. 3.3. A comparison of the experimental and theoretical dependences of skin depth on angular frequency is shown in Fig. 3.13, where the red circle indicates the correspondence between experimental measurements and the theoretical curve in this study. The errors

can be categorized as statistical errors, since errors in signal transmission in electronic devices in the millimeter-wave or optical ranges are almost of the same order in terms of dB level.

A similar analysis was conducted by Miramaru and Hangyo, [41] who showed that the skin depth of the electric field at the edge of a circular hole was 0.37 mm for incident electromagnetic waves at 260–270 GHz. Since their analysis focused on the edge of a thin MHA with circular holes, the relationships between the incident wave and the skin depth that they found were slightly different from our experimental results. However, their analysis supports the validity of our experiments and analysis in the sense that the skin depth of the SSPPs around the MHA is of submillimeter magnitude when the frequency of the incident waves is in the sub-terahertz range.

The scheme for skin-depth estimation described here is applicable to other configurations that have recently been reported. For instance, at microwave frequencies, an SSPP mode can propagate along a transmission line composed of a bow-tie cell array. [32] To determine the skin depth of this SSPP mode, one can install a similar movable conductive board above the transmission line and then detect dispersed waves using a tiny monopole antenna placed on the side of the line. For light propagating along a dielectric waveguide, [42] skin depths of sub-wavelength order have been found in the light confinement configuration, and these can be measured by installing a scattering object near the waveguide. In this case, if space is available near the waveguide, a scattering metallic probe [43] can be installed instead of a conductive board. With such a modified scheme, the dispersed wave signals around the SSPP frequency provide information about SSPPs on an MHA.

3.4 Conclusions

We have presented a theoretical analysis of the skin depth of SSPP waves around an MHA based on considering the latter as an electromagnetically uniform medium. From the results of experiments using an MHA and a conductive board, we have determined the SSPP frequency, and, by detecting reflected and dispersed wave signals at specific frequencies, we have clarified the differences between the two types of wave. We have also

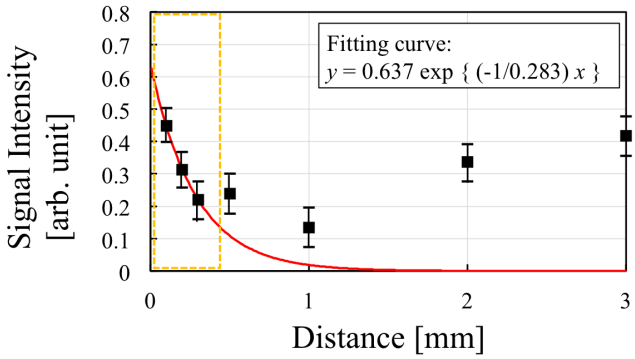

Figure 3.10: Sample-height dependence of dispersed wave signals at 103.5 GHz and a detection angle of 39°.

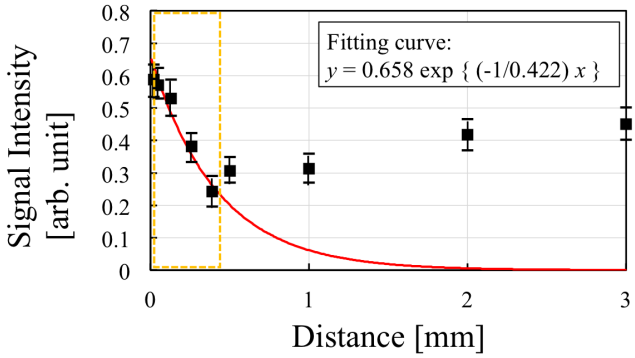

Figure 3.11: Sample-height dependence of dispersed wave signals at 104 GHz and a detection angle of 39.5°.

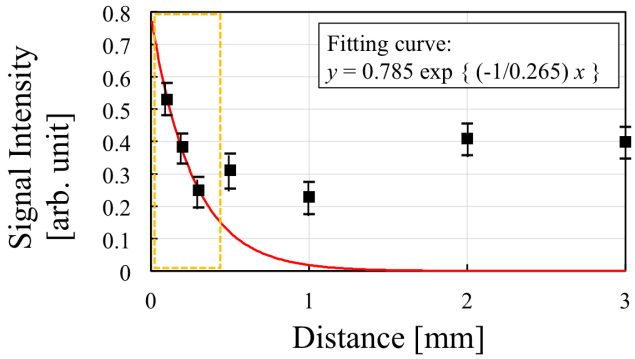

Figure 3.12: Sample-height dependence of dispersed wave signals at 104.5 GHz and a detection angle of 39°.

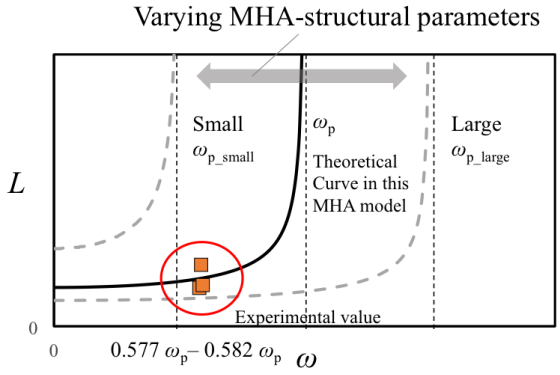

Skin depth	At 103.5 GHz	At 104 GHz	At 104.5 GHz
Theoretical	0.327 mm	0.328 mm	0.329 mm
Experimental	0.283 mm	0.422 mm	0.265 mm
Error	13.5 %	28.6 %	19.4 %

Figure 3.13: Comparison of theoretical curves and experimental results for the dependence of skin depth on angular frequency.

determined the sample-height dependences of the detected signals and have found that they exhibit exponential attenuation. Finally, using dispersed waves from the MHA, we have shown that our theoretical expression for the skin depth is consistent with experimental results in a specific frequency band.

References

[1] H. Sugai, I. Ghanashev, and M. Nagatsu, Plasma Sources Sci. Technol. **7**, 192 (1998).

[2] M. Moisan, A. Shivarova, and A. W. Travelpiece, Plasma Phys. **24**, 1331 (1982).

[3] V. O. Girka, Plasma Phys. Controlled Fusion **42**, 999 (2000).

[4] E. A. Stern and R. A. Ferrell, Phys. Rev. **120**, 130 (1960).

[5] M. Moisan, Z. Zakrzewski, and R. Pantel, J. Phys. D: Appl. Phys. **12**, 219 (1979).

[6] A. A. Strashko and V. M. Agranovich, Opt. Commun. **332**, 201 (2014).

[7] S. A. Maier, *Plasmonics: Fundamentals and Applications* (Springer, 2007).

[8] O. Kostiucenko, J. Fiutowski, T. Kawalec, V. Bordo, H. G. Rubahn, and L. Jozefowski, Opt. Commun. **331**, 77 (2014).

[9] Z. Yang, D. Gu, and Y. Gao, Opt. Commun. **329**, 180 (2014).

[10] J. Katyal and R. K. Soni, Plasmonics **9**, 1171 (2014).

[11] K. Tiwari and S. C. Sharma, Sens. Actuators A **216**, 128 (2014).

[12] Q. G. Zhu, W. Tan, and Z. G. Wang, J. Phys.: Condens. Matter **26**, 255301 (2014).

[13] T. W. Ebbesen, H. J. Lezac, H. F. Ghaemi, T. Thio, and P. A. Wolff, Nature **391**, 667 (1998).

[14] D. S. Lee, O. Sakai, and K. Tachibana, Jpn. J. Phys. **48**, 062004 (2009).

[15] K. Ooi, T. Okada, and K. Tanaka, Phys. Rev. B **84**, 115405 (2011).

[16] E. K. Stone and E. Hendry, Phys. Rev. B **84**, 035418 (2011).

[17] H. F. Ma, X. Shen, Q. Cheng, W. X. Jiang, and T. J. Cui, Laser Photonics Rev. **8**, 146 (2014).

[18] D. Woolf, M. A. Kats, and F. Capasso, Opt. Lett. **39**, 517 (2014).

[19] Y. Yuan, J. Liu, and J. Yao, Opt. Commun. **332**, 132 (2014).

[20] A. Pors, E. Moreno, L. M. Moreno, J. B. Pendry, and F. J. G. Vidal, Phys. Rev. Lett. **108**, 223905 (2012).

[21] B. Ng, S. M. Hanham, J. Wu, A. I. F. Dominguez, N. Klein, Y. F. Liew, M. B. H. Breese, M. Hong, and S. A. Maier, ACS Photonics **1**, 1059 (2014).

[22] L. Shen, X. Shen, Y. Zhong, and K. Agarwal, Phys. Rev. B **77**, 075408 (2014).

[23] A. I. F. Dominguez, L. M. Moreno, F. J. G. Vidal, S. R. Andrews, and S. A. Maier, IEEE J. Sel. Top. Quantum Electron. **14**, 1515 (2008).

[24] X. Wan, J. Y. Yin, H. C. Zhang, and T. J. Cui, App. Phys. Lett. **105**, 083502 (2014).

[25] J. B. Pendry, L. M. Moreno, and F. J. G. Vidal, Science **305**, 847 (2004).

[26] F. J. G. Vidal, L. M. Moreno, and J. B. Pendry, J. Opt. A: Pure Appl. Opt. **7**, S97 (2005).

[27] F. Miyamaru, M. Kamijyo, N. Hanaoka, and M. W. Takeda, App. Phys. Lett. **100**, 081112 (2012).

[28] F. Miyamaru, S. Hayashi, C. Otani, K. Kawase, Y. Ogawa, H. Yoshida, and E. Kato, Opt. Lett. **31**, 1118 (2006).

[29] F. Miyamaru and M. Hangyo, App. Phys. Lett. **84**, 2742 (2004).

[30] F. Miyamaru, M. Tanaka, and M. Hangyo, Phys. Rev. B **74**, 153416 (2006).

[31] S. Bhattacharya and K. Shah, Opt. Commun. **328**, 102 (2014).

[32] Y. Wu, M. Li, G. Yan, L. Deng, Y. Liu, and Z. Ghassemlooy, AIP Adv. **6**, 105110 (2016).

[33] H. T. Chen, H. Lu, A. K. Azad, R. D. Averitt, A. C. Gossard, S. A. Trugman, J. F. O'Hara, and A. J. Taylor, Opt. Express **16**, 7643 (2008).

[34] S. A. Kuznetsov, M. N. Cia, V. V. Kubarev, A. V. Gelfand, M. Beruete, I. Campillo, and M. Sorolla, Opt. Express **17**, 11730 (2009).

[35] M. J. Lockyear, A. P. Hibbins, and J. R. Sambles, Phys. Rev. Lett. **102**, 073901 (2009).

[36] F. Medina, F. Mesa, and R. Marques, IEEE Trans. Microw. Theory Tech. **56**, 3108 (2008).

[37] M. Beruete, I. Campillo, J. S. Dolado, L. M. Moreno, J. B. Abad, F. J. Vidal, IEEE Trans. Antennas Propag. **53**, 1897 (2005).

[38] S. Jahani and Z. Jacob, Nature Nanotechnol. **11**, 23 (2016).

[39] A. Vora, J. Gwamuri, A. Kulkami, J. M. Pearce, and D. O. Guney, Sci. Rep. **4**, 4901 (2014).

[40] T. Li, H. Liu, F. M. Wang, Z. G. Dong, and N. Zhu, Opt. Express **14**, 11155 (2006).

[41] F. Miyamaru and M. Hangyo, Phys. Rev. B **71**, 165408 (2005).

[42] S. Jahani and Z. Jacob, J. Opt. Soc. Am. B **32**, 7 (2016).

[43] G. Itami, O. Sakai, and Y. Harada, Electronics **8**, 239 (2019).

Chapter 4

Two-Dimensional Imaging of Permittivity Distribution by an Activated Meta-Structure with a Functional Scanning Defect

4.1 Introduction

Electromagnetic waves have huge potential for various applications such as wireless communication, micro processing, and sensing, and as a result, they will become indispensable in our daily lives. In recent years, millimeter waves or terahertz waves, with wavelengths shorter than microwaves and longer than infrared, have been attracting considerable attention. One of the features of these waves is their combination of high resolution and non-destructiveness. Therefore, a number of imaging methods that use these waves have been reported [1–3]. However, since these waves generally propagate in straight lines and attenuate immediately in lossy media, such methods frequently encounter technical issues due to the deterioration of information-carrying detection signals and their physical separation due to multipath propagation. From a microscopic point of view, an electromagnetic wave includes two components: electric and magnetic fields with their spatial distributions varying in time. This is significantly different from

other waves, like sonic waves, which can be interpreted in terms of single-variable wave propagation.

When we impose specific boundary conditions on electromagnetic waves, there is a wave component with a wavenumber vector that does not propagate spatially and concentrates around the boundaries or interfaces with exponential attenuation. This phenomenon corresponds to an evanescent wave, and in classical cases it has only been observed in the optical region [4]. In a microscopic view, when the evanescent waves get close to a conductive plate, oscillations are excited in the free electrons in the plate surface. This phenomenon is called a surface plasmon polariton (SPP) or simply, a surface wave [5–8], and it has been used in applications such as biosensors, chemical sensors and field enhancement in spectroscopy [9–11]. As described above, although an SPP can be excited only in the optical region, a similar phenomenon, with the concentration and oscillation of electric fields on the surface of a conductive plate, has also been confirmed at lower frequencies than optical bands. These are called spoof surface plasmon polaritons (SSPP) [12–16], and are broadly considered to be a unique phenomenon involving a metamaterial. One of the features of SSPPs that is not observed in other propagating modes, is the concentration of its electric field at interfaces, so that it has the potential to give us significant information about objects near such surfaces without complex signal processing. The standard example of an SSPP structure is a metal hole array (MHA), which is a conductive plate with periodic holes [17–20]. An MHA is considered to be a macroscopic effective medium in terms of controlling relative permittivity by the structural parameters of its holes. Since its structure has only a few parameters, an MHA is expected to serve as a ready-to-use functional and practical medium as well as a readily available sample for experiments [21]. Therefore, many studies of SSPPs on MHAs have been reported, although so far, they have focused on static properties as SSPP applications.

In this study, a two-dimensional imaging method using an MHA as a dynamic functional material is proposed for permittivity imaging, mainly aimed at a non-invasive medical diagnostic. Specifically, the proposed method uses the intentional formation of electromagnetic defects in the uniform electric distributions of SSPPs on an MHA, where

the defect is formed by scanning a metallic needle across the surface of the MHA. Viewed another way, the proposed method is also a non-destructive diagnostic method used as a dynamic dielectric sensor for an MHA, which is sensitive to the side opposite the needle-scanned surface. Compared to other non-destructive diagnosis tools such as confocal microscopy and near-field optical microscopy, an advantage of the proposed method is that the electromagnetic properties of subsurface tissues can be measured because surface waves in millimeter or terahertz wave bands have deeper skin penetration depths than those in optical frequency bands [22–24]. At present, the imaging of inner issues is typically achieved using a destructive method such as CT (Computer Tomography) or some other high-cost technique such as MRI (Magnetic Resonance Imaging). Actually, conventional imaging methods face difficulties arising from these issues [25–27]. Biomedical imaging based on the electromagnetic properties of biomedical tissues is considered to be an effective method because the electromagnetic properties of a malignant tumor and normal breast tissue are different [28].

In Sec. 4.2, the excitation mechanism of SSPPs on an MHA is described. In Sec. 4.3, the numerical analysis of the electromagnetic properties of an MHA, such as transmittance and reflectance, and the localized distortion of the electric fields of the SSPP mode around the MHA with a conductive probe (a needle-like conductor) is demonstrated. In Sec. 4.4, we report one- and two-dimensional imaging experiments including the experimental demonstration of biomedical diagnosis in the case of a rat lung that apply the localized distortion mechanism, with the use of an MHA targeting conductive, dielectric, and biomedical samples.

4.2 The Basis of Spoof Surface Plasmon Generation

The SSPP phenomenon was discovered by Pendry *et al.*, who also derived the theory of its generation. Here, SSPP is used for imaging by detecting the local deformation of its propagation modes. Therefore, in order to explain the proposed imaging method, we begin with the theoretical derivation of SSPP generation as its basis. First of all, the mechanism of SSPP generation on an MHA is explained. In order to describe SSPP generation on an MHA, the electromagnetic model of the process is introduced. In this

study, the MHA has holes whose size is the same order of magnitude as the wavelengths of incident waves. The model is shown in Fig. 4.1. In this model, the MHA is treated as a uniform, effective medium with a frequency-based response to incident waves. As shown in Fig. 4.1, we consider that with the incidence of optimized millimeter waves, electric fields concentrate in and around an MHA that has two-dimensional waveguide arrays (period d, cross section $p \times q$, depth w,) extended to infinity. It is assumed that the incident waves are TM-polarized optimal waves. Note that the electric field-vector of the wave has only x- and z- components, and the magnetic field-vector has only y-component in the situation. In the derivations, the coupling phenomenon between the dispersion relation of the incident waves and the waveguide modes is considered. That is, the electric fields are considered to be concentrated on the surface, and this distribution forms longitudinal waves. Thus, the SSPP modes are generated on the MHA.

Before beginning the derivation of SSPP generation, the definitions of the electric and magnetic properties in two regions are introduced. In Fig. 4.1, Region 1 indicates the space on the upper side of the MHA, and Region 2 indicates the space inside the holes of the MHA. Since Region 1 is filled with vacuum, the permittivity and the permeability in Region 1 are ϵ_0 and μ_0 respectively. On the other hand, as described above, since the MHA is presumed to be a macroscopically uniform medium, the MHA has to have an effective relative permittivity of ε m and a relative permeability μ m that is frequency dependent [12]. When electromagnetic waves whose frequency is below a cut-off frequency are introduced to an MHA, waves are attenuated with fundamental mode [29]. Therefore, the electric fields of incident waves are expressed as below.

$$E_x = E_0 \sin(\frac{\pi y}{a}) \tag{4.1}$$

Note that in this manuscript, time oscillation terms are omitted for convenience of formulation if necessary. Here, E_0 is a constant value, and Eq. 4.1 indicates that $E_x = 0$ at the edges of the holes. Therefore, the x-component and z-component of an incident wavevector k_x and k_z can be expressed as

$$k_x = \frac{\pi}{a} \tag{4.2}$$

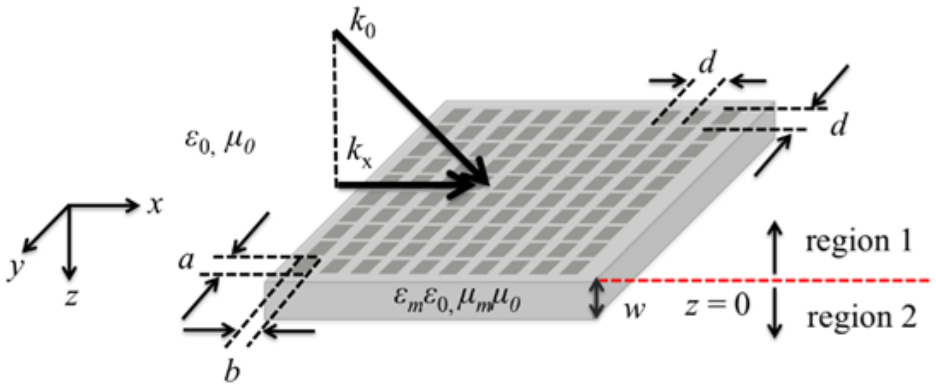

Figure 4.1: The theoretical model of the metal hole array (MHA) with TM incident waves. Region 1 is the space above the MHA. Region 2 is the space in the holes of the MHA.

$$k_z = \sqrt{\left(\frac{\pi}{a}\right)^2 - \omega^2 \epsilon_{\mathrm{h}} \mu_{\mathrm{h}} \epsilon_0 \mu_0} \tag{4.3}$$

where ϵ_{h} and μ_{h} are respectively, the relative permittivity and relative permeability in the holes of the MHA. At this point, remembering the precondition that the MHA is a macroscopic medium and has an effective relative permittivity, for example, when focused on a unit cell of the MHA (shown in Fig. 4.2), the macroscopic wave vector only has a component in the z-direction $k_z{}'$ because the waveguide mode occurs only in the holes and provides no propagation in the x- and y- directions. From the above discussions, $k_z{}'$ can be expressed as below.

$$k_z{}' = k_0 \sqrt{\epsilon_x \mu_y} = k_0 \sqrt{\epsilon_{\mathrm{m}} \mu_{\mathrm{m}}}, k_0 = \frac{\omega}{c_0}. \tag{4.4}$$

where c_0 is the velocity of light in a vacuum. The wave number of $k_z{}'$ and that of k_z should be essentially the same value, because the unit cell in Fig. 4.2 has one waveguide and there is no propagation in the conductive medium of the MHA. Therefore, the equation below is obtained by using the expression $k_z = k_z{}'$.

$$\frac{\omega}{c_0} \sqrt{\epsilon_{\mathrm{m}} \mu_{\mathrm{m}}} = \sqrt{\left(\frac{\pi}{a}\right)^2 - \omega^2 \epsilon_{\mathrm{h}} \mu_{\mathrm{h}} \epsilon_0 \mu_0} \tag{4.5}$$

On the other hand, in the matching procedure at $z = 0$, the instantaneous flow of energy

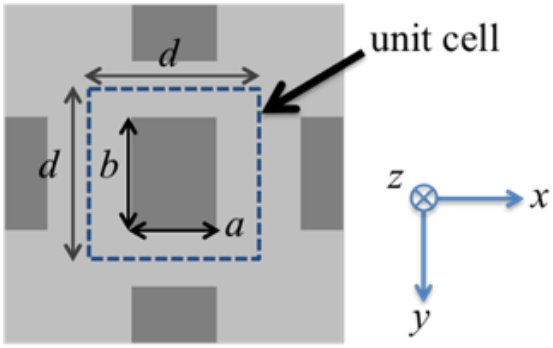

Figure 4.2: The unit cell of the MHA.

across the surface has to be considered by treating the unit cell as both a microscopic and a macroscopic medium. With the average electric fields of the unit cell regarded as a macroscopic medium

$$\overline{E_0} = E_0 \frac{a}{d^2} \int_0^b \sin\left(\frac{\pi y}{a}\right) dy = \frac{2ab}{\pi d^2} E_0. \tag{4.6}$$

$$(\boldsymbol{E} \times \boldsymbol{H})_{z,\mathrm{mic}} = \frac{-k_z {E_0}^2}{\omega \mu_\mathrm{h} \mu_0} \frac{a}{d^2} \int_0^b \sin^2\left(\frac{\pi y}{a}\right) dy = \frac{-k_z}{\omega \mu_\mathrm{h} \mu_0} {E_0}^2 \frac{ab}{2d^2}. \tag{4.7}$$

$$(\boldsymbol{E} \times \boldsymbol{H})_{z,\mathrm{mac}} = \frac{-k_z \overline{E_0}^2}{\omega \mu_\mathrm{h} \mu_0}. \tag{4.8}$$

Since Eq. 4.7 and Eq. 4.8 for the instantaneous flow of energy across the surface must have the same value, the equation $(\boldsymbol{E} \times \boldsymbol{H})_{z,\mathrm{mic}} = (\boldsymbol{E} \times \boldsymbol{H})_{z,\mathrm{mac}}$ is always useful. With this equation and Eqs. 4.5–4.8, the effective relative permittivity ϵ_m and relative permeability μ_m can be obtained as below.

$$\mu_\mathrm{m} = \mu_\mathrm{h} \frac{8ab}{\pi^2 d^2} \tag{4.9}$$

$$\epsilon_\mathrm{m} = \frac{\pi^2 d^2}{8ab} \left[1 - \left(\frac{\omega_\mathrm{p}}{\omega}\right)^2\right], \omega_\mathrm{p} = \frac{\pi c}{\sqrt{\epsilon_\mathrm{h} \mu_\mathrm{h} a}} \tag{4.10}$$

where ω_p is a cutoff frequency, and ϵ_h is the relative permittivity and μ_h is the relative permeability in the holes of the MHA. Eq. 4.10 confirms that the effective relative

permittivity of the MHA is frequency dependent. Thus, the MHA can be treated as an electromagnetic functional material.

On the other hand, remembering the magnetic field of the incident waves, this can be also solved by a wave equation for the value of Hy. Here, in discussing the generation of SSPPs in the MHA, we start by considering the magnetic field near the MHA. First, the wave equation for Hy is obtained by considering the Maxwell equations.

$$(\frac{\partial^2}{\partial x^2} + \frac{\partial^2}{\partial z^2})H_y = -\omega^2 \epsilon_{\mathrm{r}} \mu_{\mathrm{r}} \epsilon_0 \mu_0 H_y \tag{4.11}$$

where ϵ_{r} and μ_{r} are the relative permittivity and the relative permeability. With the precondition that the TM wave is incident to the MHA, it is considered that if SSPPs occur on the surface of the MHA, they must propagate along the x-direction. Also, since the incident magnetic field has the propagation constants of x and z, the y component of the magnetic field vector H_y can be expressed thus,

$$H_y = h(z) \exp\left[\mathrm{j}(k_{||} x - \omega t)\right]. \tag{4.12}$$

where $k_{||}$ is the wavenumber of an SSPP, and $h(z)$ is the amplitude of the magnetic field, depending only on the value of z. Substituting Eq. 4.12 into Eq. 4.11, the equation for $h(z)$ is obtained. It has the form

$$\frac{\partial^2}{\partial z^2} h(z) = ({k_i}^2 - \omega^2 \epsilon_{\mathrm{r}} \mu_{\mathrm{r}} \epsilon_0 \mu_0) h(z). \tag{4.13}$$

where k_i is the wavenumber of the magnetic field. In Region 1, $k_1 = \sqrt{{k_{||}}^2 - \omega^2 \epsilon_0 \mu_0}$, in Region 2, $k_2 = \sqrt{-\omega^2 \epsilon_{\mathrm{m}} \mu_{\mathrm{m}} \epsilon_0 \mu_0}$. In Region 2, when regarding the MHA as a macroscopic medium, there is no propagation of the EM waves in x-y directions, and k_1 and k_2 are required to have positive values. Considering the solution of Eq. 4.13, as the value of $|z|$ increases, the value of the amplitude $h(z)$ is supposed to decrease exponentially. From these assumptions, the relative equation obtained is:

At $z < 0$

$$h(z) = h_1 \exp\left(k_1 z\right). \tag{4.14}$$

On the other hand, at $z \geq 0$

$$h(z) = h_2 \exp(-k_2 z). \tag{4.15}$$

When considering the boundary condition of the electromagnetic field and magnetic field between Region 1 and Region 2 (at $z = 0$), the tangent components of the electric field and the magnetic field in Region 1 and Region 2 must have the same value. This condition corresponds to the condition of conventional surface plasmon generation, that is

$$k_1 = -\frac{k_2}{\epsilon_{\mathrm{m}}}, (h_1 = h_2). \tag{4.16}$$

The above expression is often used to derive the dispersion relation of a surface plasmon. However, Eq. 4.16 can also be used to derive the dispersion relation of the SSPP. By squaring Eq. 4.16 and using Eq. 4.10 and the values of k_1 and k_2, the dispersion relation that is fundamental to comprehending the results in this paper is obtained. That is,

$${k_{||}}^2 {c_0}^2 = \omega^2 + \frac{\omega^4}{{\omega_{\mathrm{p}}}^2 - \omega^2} \left(\frac{8ab}{\pi^2 d^2}\right)^2. \tag{4.17}$$

Note that the formula ${c_0}^2 = 1/\omega^2 \epsilon_0 \mu_0$ is used when deriving Eq. 4.17. The above expression is called the SSPP dispersion relation. The curve of the dispersion relation is shown in Fig. 4.3. If an angular frequency ω is close to the cutoff frequency ω_{p}, the wavenumber $k_{||}$ diverges to infinity. In other words, the SSPP modes stop propagating then. On the other hand, as the value of ω approaches zero, the dispersion relation curve comes close to a light line, although they do not cross each other, as shown in Fig. 4.3. Therefore, if an actual dispersion relation corresponds to this curve, SSPP modes are not generated. However, since the MHA is a periodic structure, it has to be treated as a two-dimensional crystal. Therefore, it should be considered that lattice scattering effects are occurring in the MHA. Here, introducing the reciprocal lattice of its structure, the definition of the wavenumber $k_{||}$ can be replaced as

$$\boldsymbol{k}'_{||} = \boldsymbol{k}_{||} - \mathrm{i}\boldsymbol{G_x} - \mathrm{j}\boldsymbol{G_y}, |\boldsymbol{G_x}| = |\boldsymbol{G_y}| = \frac{\pi}{d} \tag{4.18}$$

where $\boldsymbol{G_x}$ and $\boldsymbol{G_y}$ are the reciprocal lattice vectors in the x-direction and y-direction, respectively. So, the dispersion relation of the MHA in infinite space is also replaced by one with the spatial periodicity shown in Fig. 4.4. Fig. 4.4 confirms that there are intersection points between the actual dispersion relation and a light line. Therefore, SSPPs are indeed generated in the MHA, especially when the angular frequency ω is close to the cutoff frequency ω_{p}. If the SSPPs are generated on the surface of the incidence side of the MHA, the waves are also generated on the opposite side because the waves transmitted through the waveguides of the MHA also couple with the SSPP mode in the same way as with the incident waves. The important feature of an SSPP mode is the concentration of the electric field on the MHA. Therefore, we focused on a modification of the concentrated electric fields for a novel use as an imaging method.

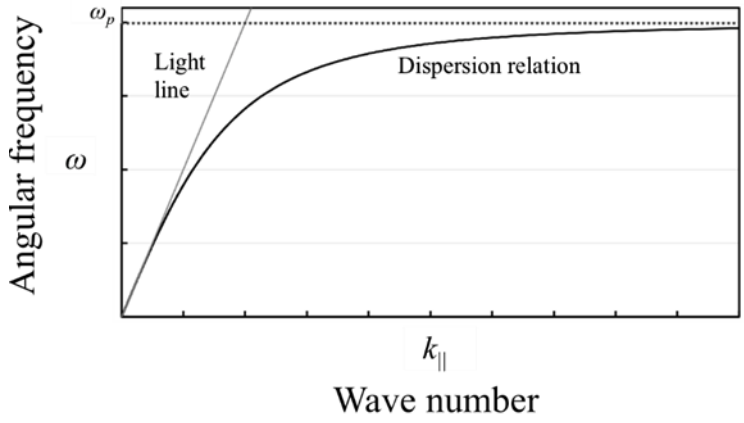

Figure 4.3: The dispersion relation of spoof surface plasmon polaritons (SSPP).

4.3 Electromagnetic Numerical Analyses of The MHA and Electromagnetic Distortion

In Sec. 4.2, we overviewed the physical basis of SSPP propagation and its dispersion, which showed that its frequencies are in fact caused and assured by the MHA. The concentration of its fields around the propagation interface was also pointed out, leading

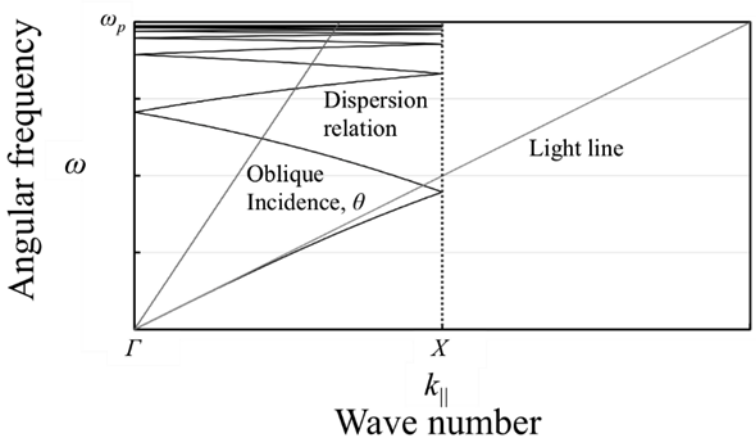

Figure 4.4: The real dispersion relation of SSPP with lattice scattering effects.

to potential applications of this propagation mode to 2D permittivity imaging that requires field uniformity over the area to be surveyed. However, the SSPP itself cannot provide us with local information on its responses to an electric field or permittivity, so in this section we confirm the effects of defect introduction on SSPP propagation.

Electromagnetic numerical analyses were performed to reconfirm the electromagnetic properties of the MHA predicted in Sec. 4.2 and to specify the electromagnetic field distortion on the MHA by a needle-like conductor. Fig. 4.5 shows the analytical model using an electromagnetic simulator (HFSS R18, Ansys, Canonsburg, PA, USA). In this simulation model, the MHA is made of copper and its thickness is 2 mm. The size of the embedded waveguide is 2 mm $\times$ 1.5 mm and the period in both the x- and y- directions is 3 mm. The coordinate notations used here correspond to those in Sec. 4.2. Periodic boundary conditions applied to the sides of the model yield a hypothetical infinite area of SSPP propagation, and the incident surface (underside, port 1) is on the side opposite the receiving surface (topside, port 2) along the long side of the model, which explains the macroscopic wave propagation; they are defined as a Floquet port. Assuming the dispersion relation shown in Fig. 4.4 for the MHA, SSPP modes exhibit resonant frequencies in a range lower than the cutoff frequency. To confirm this prediction, S-parameters (S_{11} and S_{21}) are analyzed under the above conditions in our numerical calculation, as shown in Fig. 4.6 and Fig. 4.7.

In Fig. 4.6 and Fig. 4.7, the frequency spectrum of the transmission rate has peaks

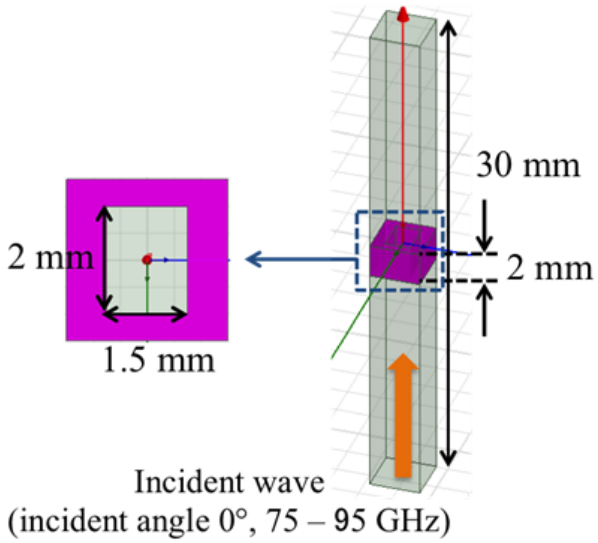

Figure 4.5: The MHA model for numerical analysis of the frequency characteristics of reflectance and transmittance.

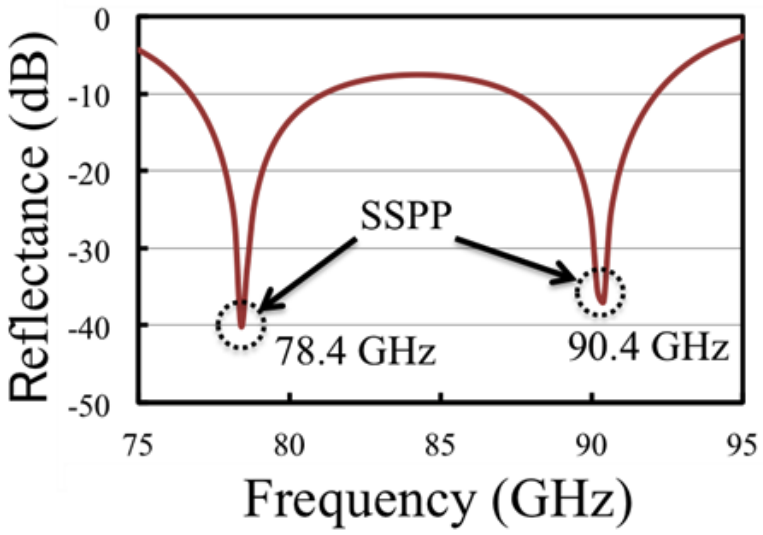

Figure 4.6: The frequency dependence of the reflectance of the MHA.

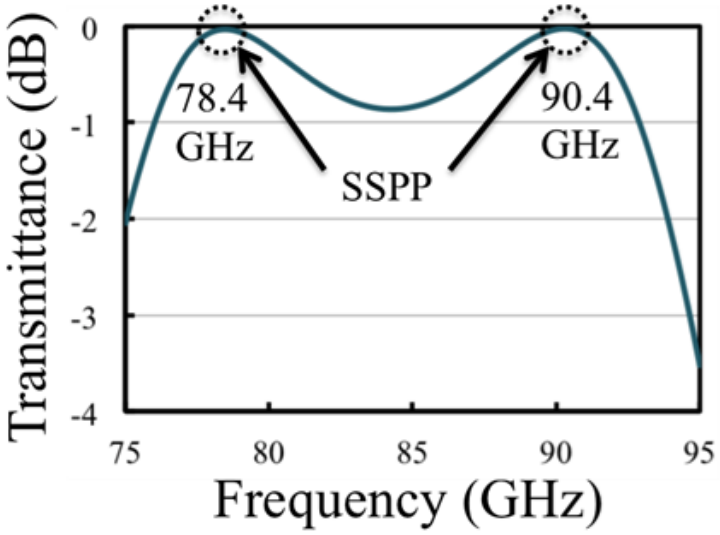

Figure 4.7: The frequency dependence of the transmittance of the MHA.

around 78.4 GHz and 90.4 GHz. This indicates the existence of at least two resonant frequencies in the MHA. These two resonances coincide with the intersection points of the dispersion relation of the SSPP and the light line in Fig. 4.4; at these frequencies, energy conversion from the mode in free space propagation to the SSPP mode is smooth, thanks to good wave matching conditions. This phenomenon was termed extraordinary transmission as one of the features of an MHA [17–21]. In other words, at 78.4 GHz and 90.4 GHz, SSPP generation/propagation is possible where SSPP modes are able to uniformly concentrate electric fields on and in the vicinity of MHAs due to the multiple lattice scattering described in Eq. 4.18.

In this uniform 2D field, localized distortion is induced by inserting a needle-like conductor into a hole of the MHA. Electric fields are distorted strongly at sharp conductive boundaries, a phenomenon known as the near field effect [30], unlike wave propagation that includes a dispersion relation. Such distorted electric fields decay spatially with a wavelength-order attenuation constant. For this reason, another set of two analytical models (shown in Fig. 4.8) was tested in our simulation runs. One has the MHA equipped with a conductive probe, and the other has only the MHA with its periodic 2D structure. That is, although the shape of both MHAs is the same as that in the model in Fig. 4.5, the model has 5×5 holes in order to observe the difference in electric field distributions

between case 1, insertion of a conductive probe in the MHA, and case 2, removal of the conductive probe. Note that the model of a conductive probe is positioned in or near a center hole. The probe has a cone shape, with a radius at the bottom plane of 0.5 mm and a height of 6 mm. Under these conditions, by using the model as shown in Fig. 4.8, the electric field distributions of the two cases were monitored at 78.4 GHz, which is a candidate for the SSPP frequency near the resonant frequency observed in Fig. 4.6. The results of the distributions in the two cases and their numerical comparison at $z = +0.5$ mm and -0.5 mm, are shown in Fig. 4.9.

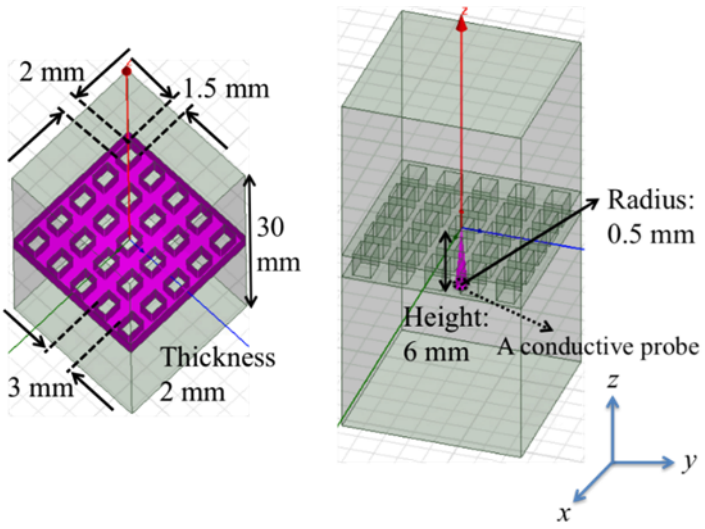

Figure 4.8: The two models for numerical analyses of the electric field distribution around the MHA.

From Fig. 4.9a, in the case on the left, electric fields are concentrated around the MHA, which is unlike the electric fields of the waveguide mode because those fields are concentrated not around holes but in holes. However, the results indicate that the fields are like compression waves, strongly affected by existing holes. Since the distribution of the fields around the MHA is symmetrical in the y-z plane, the electric-field distributions are partial components of an SSPP. This fact is consistent with a feature of SSPPs in which the mode expands its field on the side opposite the incident side when the mode is excited at an incident side. This result shows that the fields distribute by a coupling phenomenon between the SSPP mode and transmission waves. On the other hand, in the case on the right, looking at the electric distribution in the red circle, it was found that

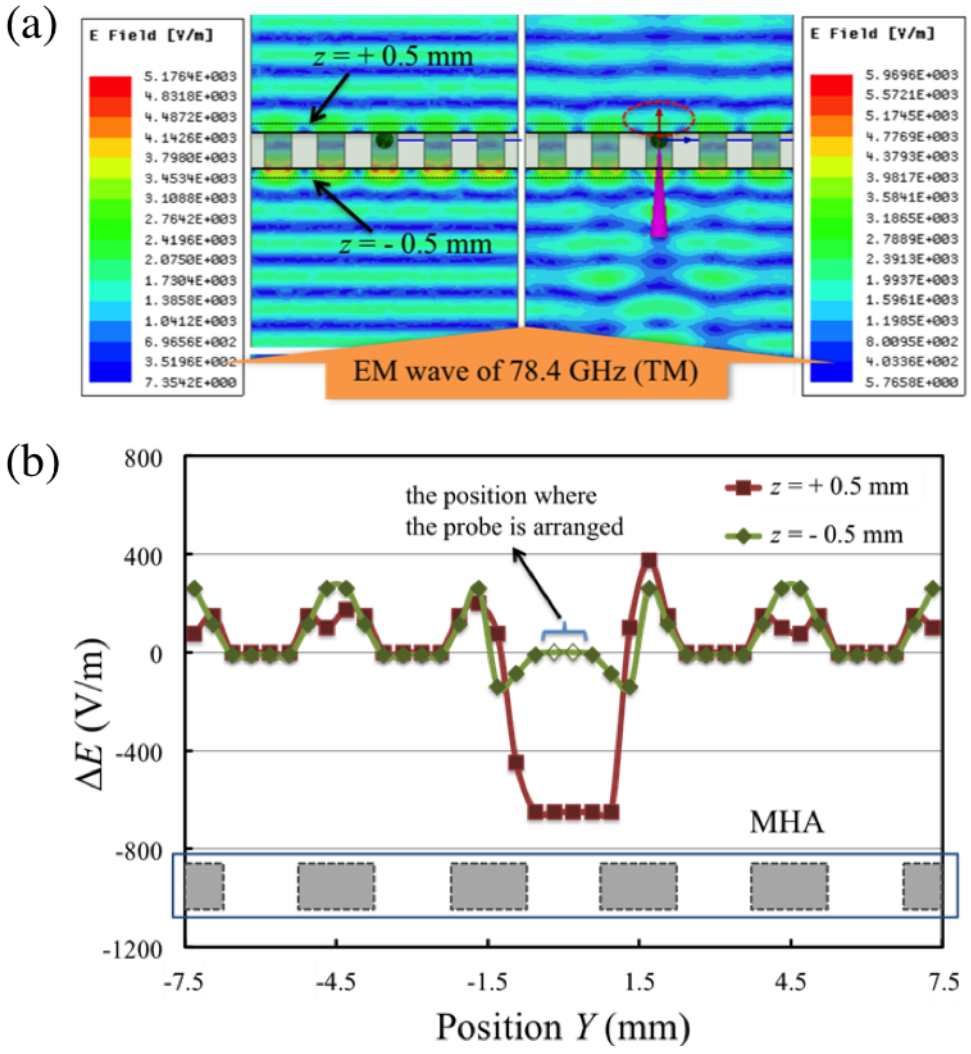

Figure 4.9: (a) The two electric field distributions around the MHA without (left) and with (right) a conductive probe; (b) the numerical results of the two cases ($z = +0.5$, -0.5 mm), which is the difference between the distributions with and without a conductive probe.

the electric field distributions are less concentrated than the distributions at the same region in the case on the left, while field distributions of the other holes in the case on the right are at the same level as those in the case on the left. These facts indicate that the electric fields in the region with the red circle are locally distorted by a conductive probe. Consequently, the results specifically show that localized electromagnetic distortions can be generated by inserting a conductive probe in a hole of an MHA.

From Fig. 4.9b, as shown in the numerical results in the case of $z = +0.5$ mm in Fig. 4.9a, it was found that there are significant differences in the region around a conductive probe. This is because the electric field distribution on the MHA is deformed by the insertion of a conductive probe, as displayed in Fig. 4.9a. On the other hand, from the numerical results in the case of $z = -0.5$ mm, it was found that the difference between the two electric field distributions under the MHA is much smaller than the one on the MHA. This might be explained by the suggestion that the field distributions around the MHA are only distorted by a near-field effect. From these results, the differences in the two cases are potentially sufficient to detect the information in the deformed distributions because in practice, these differences are detected as signal intensities related to the square of the electric field.

The discussion above suggests that by taking the difference between the electric-field distributions of the holes when a conductive probe is inserted, and when not, local signals in the limited vicinity of each hole of the MHA can be obtained with detectable intensities and enhanced spatial resolution.

4.4 Two-Dimensional Imaging Experiments Using MHA and a Conductive Probe

In Sec. 4.3, the numerical results showed that an SSPP propagates in the MHA when electromagnetic waves at optimal frequencies enter the plate, and that its propagation can be locally deformed by a conductive metallic probe. To detect wave media information at the deformation point where electromagnetic waves enter the MHA, scattered waves generated apart from reflected waves play important roles in the frequency range,

which includes the incidence of optimal waves. In the experiments discussed in this section, we used scattered waves, which exhibit the characteristics of local electromagnetic distribution [31]. Transmitter and receiver antennae, and a conductive probe are the main diagnostic tools manipulated for signal detection.

We performed experiments on one- and two-dimensional imaging using an MHA with structural parameters that were the same as those in the analytical model, and the MHA was equipped with a scanning conductive probe. After the one-dimensional imaging experiments, two-dimensional imaging experiments were performed using conductive and dielectric samples. Finally, we demonstrated a biomedical diagnosis in the case of a rat lung by using the system. The experimental system is shown in Figs. 4.10 - 4.12, with a schematic view of the corresponding MHA and the conductive probe.

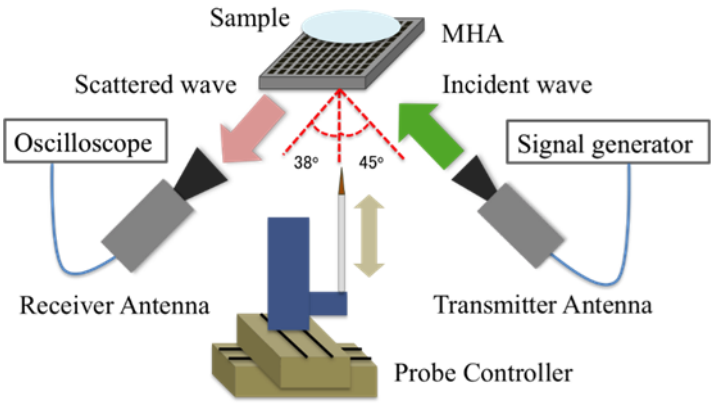

Figure 4.10: The experimental system for one- and two- dimensional imaging experiments.

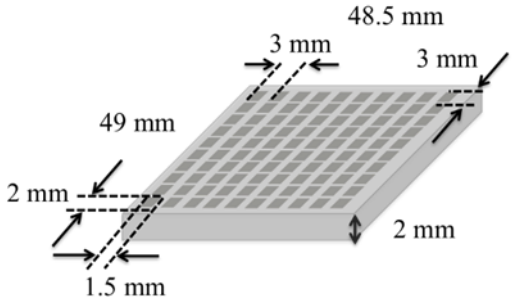

Figure 4.11: MHA of the imaging experiments.

As suggested by the above analyses, we searched for the most appropriate frequency

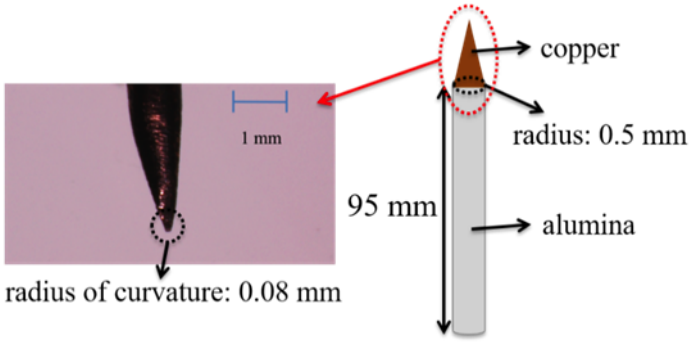

Figure 4.12: The conductive probe for localized electromagnetic distortion.

for electromagnetic-wave experiments in the optimal bands for SSPP propagation, by using one-dimensional imaging experiments, which gave us simple and straightforward evidence as the conductive probe scanned along one line. With the incidence of electromagnetic waves at 78-86 GHz from a transmitter antenna into the structure shown in Fig. 4.11 , SSPPs form on the MHA and scattered waves are emitted, partly at the reflection angle of 38 degree. For a specific diagnostic sequence, two signals detected by a receiver antenna were recorded; in case 1: the conductive probe is inserted into a hole of the MHA, and in case 2: the conductive probe is removed from the MHA. By repeating the process, the signals in case 1 and case 2 of all the used holes shown in Fig. 4.13 were obtained. Subtracting the signal of case 2 from that of case 1 for each hole, the differential signals of all the holes create one signal data set with a spatial profile. The processes described above were conducted for the following two series; for data set A; a sample (cylindrical aluminum stick, radius 1.6 mm, height 110 mm) on the MHA and for data set B; the sample was removed from the MHA. Finally, the one-dimensional imaging map was completed by subtracting the signals of data set A from those of data set B. The sample, and the results as an example are shown in Fig. 4.13.

Fig. 4.13 shows that the detected signals of a conductive sample obtained at $x \sim 8$ mm, which corresponds to the location of the sample, are remarkable when electromagnetic waves in the frequency range of 78-80 GHz and around 83 GHz are incident. It also indicated that other waves cannot detect significant signals. Since the incident angle at each hole of the MHA differs slightly from the reflective angle in the system, detection capacity might depend on the frequency of incident waves to some degree. For this rea-

son, using a longer distance from the MHA to the transmitter and receiver antennas may provide greater uniformity in SSPPs generated on the MHA. From the results shown in Fig. 4.13, we fixed the operation frequency at 83 GHz.

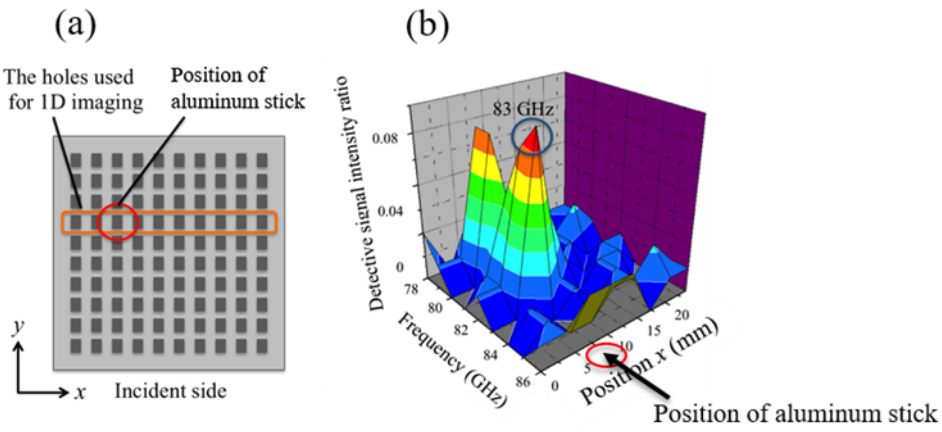

Figure 4.13: (a) The holes used for one-dimensional imaging; (b) the result of one-dimensional imaging for incident waves of 78-86 GHz.

After the selection of the wave frequency based on the one-dimensional experiment, we performed experiments for two-dimensional permittivity imaging. Three samples with different permittivity values were provided, and we used them for two-dimensional imaging experiments, using an experimental system similar to that shown in Figs. 4.10 - 4.12. Similar to the one-dimensional imaging experiments, the samples were set up on the MHA, and optimal signals were assured by executing the process described above (two procedures for data sets A and B in which cases 1 and 2 are for profiling). The samples included one conductive material, copper sticks, and a dielectric solid and liquid, an alumina stick and DMSO (dimethyl sulfoxide). The values of relative permittivity of alumina and DMSO are 9.9 and $43 - j10.9$, respectively, in the millimeter-wave band. DMSO works as a biomaterial phantom in our experiment, since its permittivity is nearly equal to that of the human body [32]. To contain the liquid DMSO in the setup, an acrylic capsule array was used as a supporting experimental tool. Therefore, when comparing signals, in data set A the sample was on and in; in data set B, the sample was removed from the MHA and an acrylic capsule array was set up in the same position on the MHA in both cases. The results of the two-dimensional imaging experiments for

these three types of sample are shown in Figs. 4.14 - 4.17.

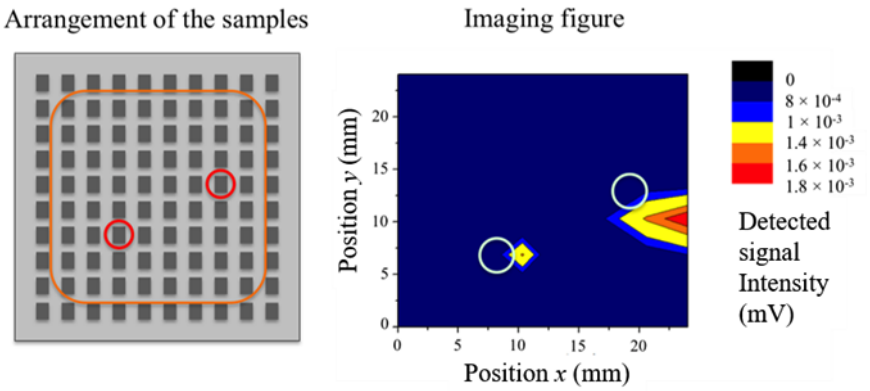

Sample: **two copper sticks (2 mm × 2 mm × 30 mm)**

Figure 4.14: Two-dimensional imaging of conductive samples (two copper sticks).

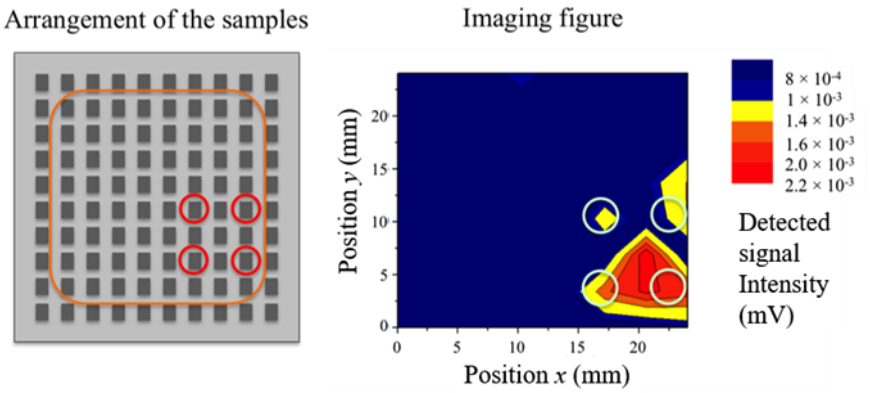

Sample: **four copper sticks (2 mm × 2 mm × 30 mm)**

Figure 4.15: Two-dimensional imaging of conductive samples (four copper sticks).

In Figs. 4.14 and 4.15, although the positions of the detected signals are slightly different from the actual positions of the samples, the existence of the conductive samples was clearly detectable and related to their position. Also, in Figs. 4.16 and 4.17, the results confirm the detection of dielectric samples at almost their proper positions even when the positions of the samples varied, though DMSO is a lossy material. These results show the effectiveness of the use of concentrated electric distributions for permittivity signal detection in this scheme, which differs from conventional methods of signal detection in the microwave band. Also, comparing the results of the conductive samples (Figs. 4.14 and 4.15) to those of the dielectric samples (Figs. 4.16 and 4.17), the

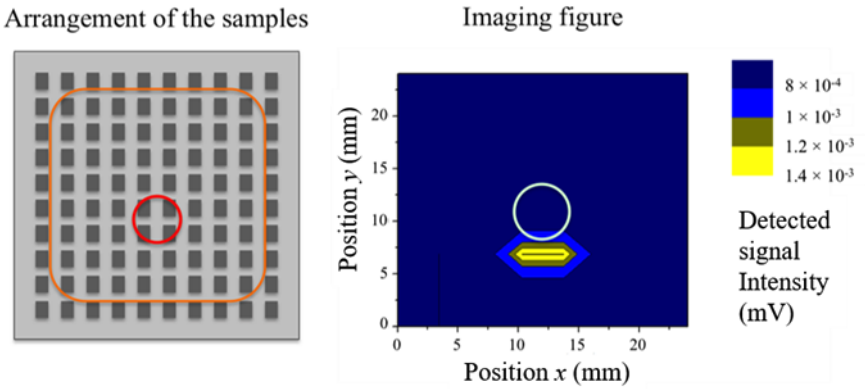

Sample: **an alumina stick (radius: 3 mm, height: 61 mm)**

Figure 4.16: The two-dimensional imaging of dielectric samples (an alumina stick).

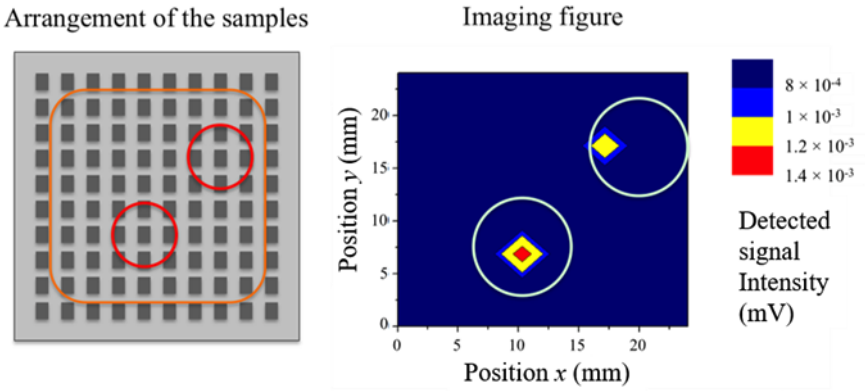

Sample: **DMSO (liquid, 150 µL ×2, in an acrylic case)**

Figure 4.17: Two-dimensional imaging of dielectric samples (DMSO).

positions of the detected signals of the former are less accurate than those of the latter. Considering the fact that the electric distributions of SSPPs are distorted to a greater extent by conductors than by dielectrics, the detection accuracy in the latter case may be superior to that in the former case. Furthermore, Figs. 4.14 and 4.15 suggest that the detection accuracy for samples near corners is low in comparison with that of samples on inner locations. Since, in these experiments, the MHA has a limited size and SSPPs on the MHA are reflected at its corners, the electric distribution of SSPPs near corners tends to be non-uniform. Therefore, the distributions in the vicinity of its corners are not stable, and the detection accuracy of samples on corners tends to be low. By using an MHA with a larger number of holes, the detection capacity might be sufficiently accurate for practical use. On the other hand, the maximum values of the detected signal intensities of conductive samples are more intense than those of dielectric samples. In general, electric fields are affected more by conductors than dielectrics because of the boundary condition on the surface of conductors. Since DMSO has the large value of the imaginary part, it is consistent with the fact that the average value of the detected signal intensities in the case of the alumina sample was larger than that of DMSO. However, sufficient signal intensities were monitored in both cases for practical imaging, since the intensities satisfied the dynamic ranges of dB-order in the experiments. The results in all the cases confirm that the proper signals are obtainable at a mm-order distance by using the proposed method. This is an advantage over the conventional sensing method in which lasers or other strong light sources are required in the optical range.

The above discussions support the feasibility of a biomedical diagnosis that uses the proposed system. Finally, the result of the biomedical diagnosis in the case of a rat lung is reported. As shown in Fig. 4.18, the results confirm a detection of the sample in more than half of the area. Although there is some slight signal misdetection, it shows that two-dimensional dialectic responses of the biomedical sample can be obtained in the proposed system.

The above discussions and results indicate that the proposed method can be used for 2D imaging of permittivity distribution, and may be useful for biomedical diagnosis after optimization as a medical facility tool.

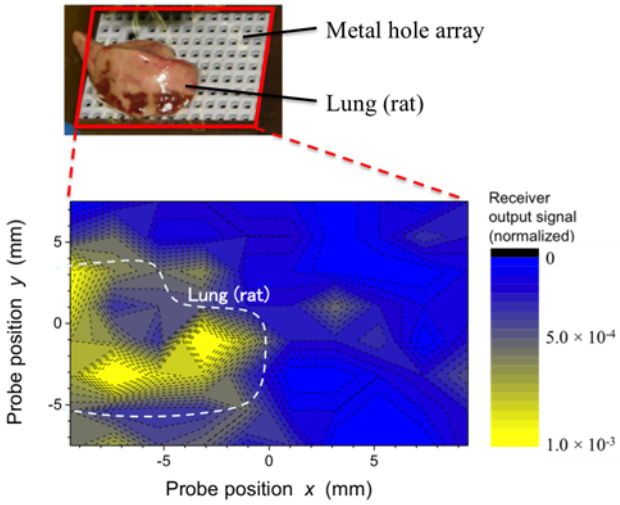

Figure 4.18: The result of biomedical diagnosis by using an MHA with rectangular holes (the size is 1.8 mm × 1.4 mm, the periods of each direction are 2.5 mm, 2 mm and the thickness is 2.3 mm) in the case of a rat lung.

4.5 Conclusions

A 2D imaging method is proposed in this study, based on a meta-structure with a scanning defect, using a metal hole array (MHA) and a conductive probe (a needle-like conductor) in the millimeter-wave range. In order to validate the proposed method, a theoretical model of SSPP generation on an MHA was introduced, numerical electromagnetic analyses of localized distortions of the electric fields on and around the MHA were conducted, and one- and two-dimensional imaging experiments using conductive and dialectic samples verified the theoretical predictions.

In Sec. 4.2, the dispersion relation of SSPPs in the case where the MHA has rectangular holes with oblique incidence of sampling waves was derived, which indicated the physical phenomenon of SSPP generation on an MHA. In Sec. 4.3, with the use of HFSS, the transmission and reflection properties of an MHA were analyzed when millimeter waves were injected into the structure, and this analysis implied that SSPP modes exist under the cut-off frequency in our MHA model. In addition, the electromagnetic distributions around an MHA with an inserted conductive probe were compared with those of an MHA without the probe, confirming the difference in the electric distributions around the MHA in the two cases. Specifically, insertion of a conductive probe into an

MHA can be useful for localized electromagnetic distortion. In Sec. 4.4, using an MHA and a conductive probe, a one-dimensional experiment was performed and confirmed the frequency dependency of the detected signal intensity in the range of 78-86 GHz. This showed that a wave at 83 GHz can be monitored, producing the most intense level of detected signals. Then, two-dimensional imaging experiments with conductive samples (copper sticks) and dielectric samples (an alumina stick and DMSO (liquid)) were performed with the use of optimal waves at 83 GHz. Consequently, it was confirmed that the proposed measurement system allows the detection of the positions of conductive and dielectric samples by comparing the intensity levels of reflected signals with and without the samples. Finally, we demonstrated a biomedical diagnosis in the case of a rat lung by using the system. The result shows that although there is slight signal misdetection, two-dimensional dialectic responses of the biomedical sample can be obtained using the proposed method. Therefore, the proposed method has the potential for use in the two-dimensional imaging of permittivity distribution, such as in the biomedical task of localized tumor detection.

References

[1] J. Hasch, E. Topak, R. Schnabel, T. Zwick, R. Weigel, and C. Waldschmit, IEEE Trans. Microw. Theory Tech. **60**, 845 (2012).

[2] P. C. Theofano and G. C. Trichopolous, IEEE Antennas Wirel. Propag. Lett. **17**, 213 (2018).

[3] M. T. Ghasr, M. J. Horst, M. R. Dvorsky, and R. Zoughi, IEEE Trans. Antennas Propag. **65**, 258 (2017).

[4] F. long, M. He, H. C. Shi, and A. N. Zhu, Biosens. Bioelectron. **23**, 952 (2008).

[5] J. Katyal and R. K. Soni, Plasmonics **9**, 1171 (2014).

[6] K. Tiwari and S. Sharma, Sens. Actuators A **216**, 128 (2014).

[7] Q. Zhu, W. Tan, and Z. Wang, J. Phys. Condens. Matter **26**, 255301 (2014).

[8] A. A. Strachko and V. M. Agranovich, Opt. Commun. **332**, 201 (2014).

[9] J. N. Anker, W. P. Hall, O. Lyandres, N. C. Shah, J. Zhao and R. P. V. Duyne, Nat. Mater. **7**, 442 (2008).

[10] L. E. Kreno, K. K. Leong, O. K. Farha, M. Allendorf, R. P. V. Duyne and J. T. Hupp, Chem. Rev. **112**, 1105 (2012).

[11] J. P. Camden, J. A. Dieringer, J. Zhao, and R. P. V. Duyne, Acc. Chem. Res. **41**, 1653 (2008).

[12] J. B. Pendry, L. M. Moreno, and F. J. G. Vidal, Science **305**, 847 (2004).

[13] D. Woolf, M. A. Kats, and F. Capasso, Opt. Lett. **39**, 517 (2014).

[14] S. Bhattacharya, K. Shah, Opt. Commun. **328**, 102 (2014).

[15] L. Shen, Phys. Rev. B **77**, 075408 (2008).

[16] B. Ng, S. M. Hanham, J. Wu, A. I. F. Domoonguez, N. Klein, Y. F. Liew, M. B. Breese, M. Hong, and S. A. Maier, ACS Photonics **1** 1059 (2014).

[17] F. Miyamaru and M. Hangyo, Phys. Rev. B **71**, 165408 (2005).

[18] F. Miyamaru, S. Hayashi, C. Otani, and K. Kawase, Opt. lett. **31**, 1118 (2006).

[19] F. Miyamaru, M. Kamijyo, N. Hanaoka, and M. W. Takeda, Appl. Phys. Lett. **100**, 081112 (2012).

[20] F. Miyamaru and M. Hangyo, Appl. Phys. Lett. **84**, 2742 (2004).

[21] F. Miyamaru, Phys. Rev. B **74**, 153416 (2006).

[22] M. Brissova, M. J. Fowler, W. E. Nicholson, A. Chu, B. Hirshberg, D. M. Harlan, and A. C. Powers, J. Histchem. Cytochem. **53**, 1087 (2005).

[23] A. E. Klein, N. Janunts, M. Steinert, A. Tunnermann, and T. Pertsch, Nano Lett. **14**, 5010 (2014).

[24] G. Itami and O. Sakai, J. Appl. Phys. **125**, 213101 (2019).

[25] C. C. Meltzer, J. C. Prlce, C. A. Mathis, P. J. Greer, M. N. Cantwell, P. R. Houck, B. H. Mulsant, D. B. Loprestl, and S. T. Dekosky, Am. J. Psychiatry **156**, 1871 (1999).

[26] S. B. Haim, V. L. Murthy, C. Breault, R. Allie, A. Sitek, N. Roth, J. Fantony, S. C. Moore, M. A. Park, and M. Kijewski, J. Nucl. Med. **54**, 873 (2013).

[27] M. F. Juette, T. J. Gould, M. D. Lessard, M. J. Mlodzianoski, B. S. Nagpure, B. T. Bennett, S. T. Hess, and J. Bewrsdorf, Nat. Methods **5**, 527 (2008).

[28] S. Kubota, X. Xiao, N. Sasaki, Y. Kayaba, K. Kimoto, W. Moriyama, T. Kozaki, M. Hanada, and T. Kikkawa, Jpn. J. Appl. Phys. **49**, 097001 (2010).

[29] F. J. G. Vidal, L. M. Moreno, and J. B. Pendry, J. Opt. A Pure Appl. Opt. **7**, S97 (2005).

[30] K. Sekimoto and M. Takayama, Eur. Phys. J. D **60**, 589 (2010).

[31] G. Itami, T. Akiyama, O. Sakai, and Y. Harada, Proc. Asia-Pacific Microw. Conf. (APMC), Miyagi, Japan, Nov. (2014).

[32] M Urata, S. Kimura, K. Wakino, T. Kitazawa, Proc. IEEE Int. Symp. Antennas Propag. (APSURSI), WA, USA, July (2011).

Chapter 5

Direction-of-Arrival Estimation from Scattering Patterns in a Subwavelength Periodic Structure of a Conductive Scatterer

5.1 Introduction

Unintentional electromagnetic radiation from electric devices, and other electromagnetic interference, can cause quality deterioration in wireless communications. The expansion of mobile networks such as 5G and IoT is increasing the use of communication devices such as laptops and smart phones, making the deterioration of wireless communication quality a source of increasing concern. Therefore, it is necessary to rapidly and effectively detect the causes of such interference with wireless communications. This has led to many studies of direction-of-arrival (DOA) estimation methods and 2D imaging methods, using microwave lenses, array antennas, and electromagnetic absorbers that use electromagnetic band gap (EBG) structures [1–3]. However, these techniques still require significant development effort to achieve adequate versatility and portability. Many problems remain, including bandwidth coverage, as well as device size and complexity. In microwave bands, the relatively long wavelength compared to the visible spectrum

makes the miniaturization of lenses difficult. Furthermore, in the cases without lens, i.e., with array antenna, they require to detect phases of incident waves in order to estimate the incident angles. Such requirements tend to make these devices expensive.

Electromagnetic-wave control about propagation and scattering has been actively studied in microwave bands and optical wave-bands. Typical applications include frequency-selective surfaces (FSS) for microwave bands, and photonic crystals for optical wave-bands [4, 5]. Their common feature is the use of periodic structures of conductive or dielectric materials, which demonstrates the utility of periodic structures for manipulating or controlling electromagnetic waves. Since the aim of these studies is mainly to control intentional waves and reduce scattered waves, periodic structures have been used to construct resonating or other mechanisms to control the radiation of intentional waves. However, scattered waves are generated by the interaction of incident waves and scatterers such as periodic structures, so scattered waves naturally carry information about incident waves. Thus is it reasonable to consider the uses of scattered waves, and since their capture does not require the rigorous adjustment of resonating structures designed for intentional waves, there is a possibility for information capture of broadband waves.

In this study, a novel DOA estimation method is proposed, which is based on formation of electromagnetic scattering patterns. Specifically, electromagnetic scattering patterns of incident waves are created by using subwavelength periodic structures of conductive scatterers (SPCS), with the scattering patterns extracted as sensor-detected spatial distributions of signal intensity. Finally, the incidence angles and frequencies of the waves are estimated by analyzing the spatial distributions as inverse problems. The proposed technique has the potential to realize miniaturized, low cost, and broadband devices. Periodic structures of subwavelength-size make the device miniaturized. And the device is simplified by using only spatial distributions of the signal intensities detected by sensors. Since the device requires no rigorous structural optimizations for a specific wave such as resonator, its available bandwidths consequently broaden.

On the other hand, periodic structures of subwavelength size are also used for super lenses, negative refractive index media, and spoof surface plasmon-structures, and

such structures are known as metamaterials, which has attracted much attention and have been actively studied recently [3, 4, 6, 7]. As described above, metamaterial is also based on resonance mechanism, and has the feature of structural optimization for intentional waves. However, when focused on not resonance structure but scattering pattern forming, it has the potential of acquisition of information about electromagnetic-wave parameters by controlling scattering patterns with the use of periodic structures of subwavelength size. Actually, it is the confirmed phenomenon that the standing waves which are different from the case of diffraction grating are generated around periodic structures of subwavelength size.

In this report, first, the generation mechanism of the scattering patterns in SPCS is described. Then, analytical studies are presented that show the formation of scattering patterns like standing waves for each frequency and each incidence angle. Finally, experimental results of spatial distributions of signal intensities of the corresponding wave are reported.

5.2 Scattering Production of Subwavelength Periodic Structure of a Conductive Scatterer

To describe the electromagnetic scattering phenomena of SPCS, the electromagnetic propagation model shown in Fig. 5.1 is considered. In this study, the electromagnetic propagation model in Fig. 5.1 is provided as a 2D space. And for simplicity, there is a one-dimensional SPCS of rectangular scatterers with the incidence of TM-polarized waves. Assume that incident electric field $\boldsymbol{E}$ and magnetic field $\boldsymbol{H}$ in Region 1 are defined as $\boldsymbol{E} = [E_x, 0, E_z]$ and $\boldsymbol{H} = [0, H_y, 0]$ respectively, and wavenumber vector of incident waves is defined as $\boldsymbol{k} = [k_x, 0, k_z] = [k_0 \sin\theta, 0, k_0 \cos\theta]$. Note that $\boldsymbol{k}$ is an incident wavenumber vector, k_0 is a scalar value of a free space wavenumber vector, and θ is an incident angle.

In this case, the x-component and z-component of a wavenumber vector in Region 2 k'_x and k'_z can be expressed as below from a periodic boundary condition based on Floquet's theorem,

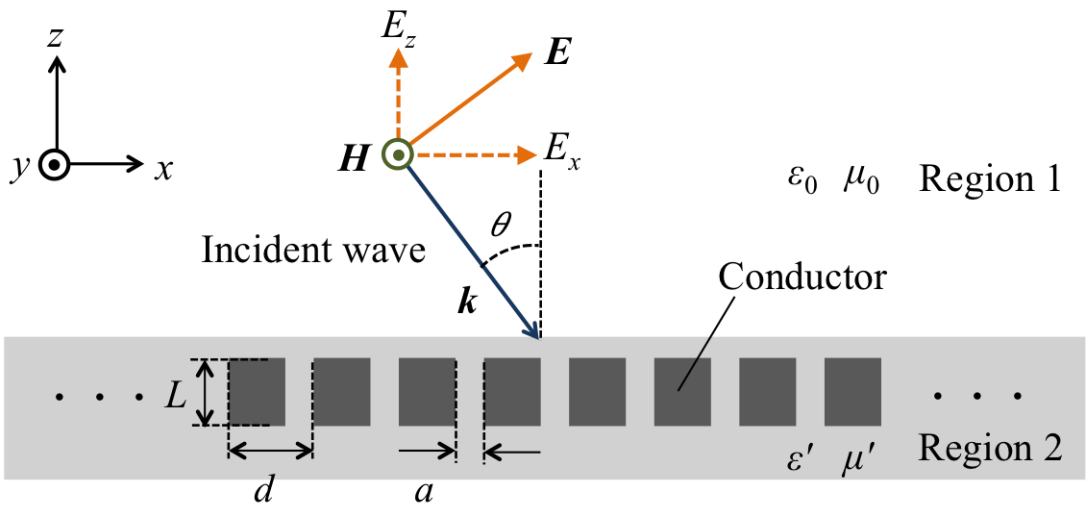

Figure 5.1: Schematic view of a theoretical model of electromagnetic propagation in an SPCS.

$$k_x' = k_x'(m) = k_x + \frac{2m\pi}{d}\,(m = 0, 1, 2, ...) \tag{5.1}$$

$$k_z' = \sqrt{{k_0}^2 - {k_x'}^2} \tag{5.2}$$

Where d is the period of SPCS. From [7], the SPCS has the potential to be used as an artificial lens with a high refractive index. In order to derive the effective refractive index, the TEM incidence condition ($E_z = 0$) is considered. Also, the average electric and magnetic fields in the unit cell are expressed as $\boldsymbol{E'} = (a/d)\boldsymbol{E}$, and $\boldsymbol{H'} = \boldsymbol{H}$. Therefore, assuming effective permittivity ϵ', permeability μ', and refractive index n', the quantitative relationship between electric and magnetic fields can be derived as

$$\frac{|\boldsymbol{E}|}{|\boldsymbol{H}|} = \sqrt{\frac{\mu_0}{\epsilon_0}}, \tag{5.3}$$

$$\frac{|\boldsymbol{E'}|}{|\boldsymbol{H'}|} = \sqrt{\frac{\mu'}{\epsilon'}}, \tag{5.4}$$

$$n' = \sqrt{(\frac{\epsilon'}{\epsilon_0})(\frac{\mu'}{\mu_0})}, \tag{5.5}$$

Where ϵ_0 and μ_0 are permittivity and permeability in free space. Then, since the instantaneous energy flows of actual electromagnetic fields and the average electromagnetic fields must be the same value, the following equation is obtained,

$$(\boldsymbol{E} \times \boldsymbol{H})_z \times L \times a = (\boldsymbol{E'} \times \boldsymbol{H'})_z \times L' \times d \tag{5.6}$$

Here L is the thickness of the SPCS, and L' is the effective thickness when SPCS is treated as an effective medium, and a is the width of a slit. By solving Eq. 5.6, the effective permittivity and permeability are obtained as below,

$$\frac{\epsilon'}{\epsilon_0} = (\frac{d}{a})^2 \tag{5.7}$$

$$\frac{\mu'}{\mu_0} = 1 \tag{5.8}$$

$$n' = \frac{d}{a} \tag{5.9}$$

From Eq. 5.9, it is found that the effective refractive index n' can be enhanced by reducing the value of a. In this model, although the SPCS works as an artificial lens only in the z-direction, when the shape of the scatterer is replaced with a circle, it is considered that SPCS of a circle can work as an artificial lens for both x- and z-directions of TM incidence. Therefore, each scattering pattern can be generated in a closed area by the SPCS in accordance with the frequency and incidence angle of incident waves.

5.3 Electromagnetic Analyses of Scattering Patterns

In order to examine the frequency and angular dependencies of the scattering patterns of electric fields in an SPCS, the analysis model shown in Fig. 5.2 is provided by using HFSS. In the model, the SPCS is composed of 9 cylindrical aluminum scatterers, with conductive plates set near the side of the model to avoid the invasion of other waves. It is assumed that incident waves are plane waves and propagate in the direction of the red arrow shown in Fig. 5.2. Under these analytical conditions, the electric field

intensity distributions in the red dotted area in Fig. 5.2 are analyzed as the frequency and incidence angle of the waves are changed. Note that the electric field intensities are calculated by taking a time average. These analyses were conducted for these four cases: (2 GHz, $\theta = 30°$, $r = 10$ mm), (4 GHz, $\theta = 30°$, $r = 10$ mm), (2 GHz, $\theta = 45°$, $r = 10$ mm), (2 GHz, $\theta = 30°$, $r = 15$ mm) to compare the different scattering patterns produced by waves of different frequency and incidence angle, and scatterers of different radius. Here r is the radius of scatterers and θ is the incidence angle. The analytical results are shown in Fig. 5.3.

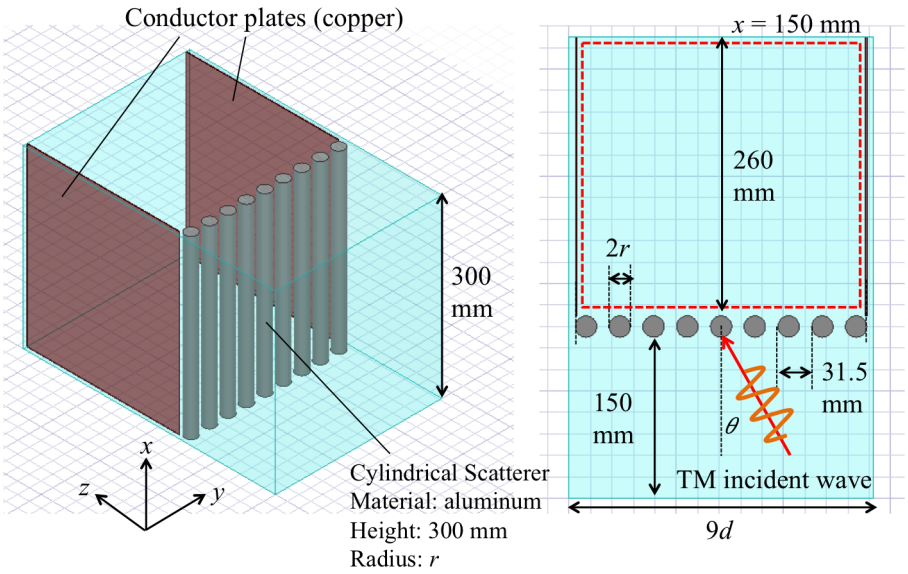

Figure 5.2: Analyzed model of scattering pattern.

In Fig. 5.3, comparing (a) with (b) shows that the scattering pattern of electric fields in (b) is more apparent than that in (a), and the number of entire patterns in (b) is also larger than that in (a). However, a number of scattering patterns is considered not to be proportional to the wavenumbers of the incident waves. And comparing (a) with (c), the number of entire patterns in (c) is seen to be smaller than that in (a). The contrast in the scattering patterns in (c) is higher than those in (a) especially in the y-direction. This effect is due to the wavenumbers in the y-direction, because that wavenumber is larger in case (b) than in case (a). The contrast in the scattering patterns of (d) is much larger than that in case (a). This is consistent with the theoretical model of SPCS explained in Sec. 5.2 because the effective refractive index is increased as the radius

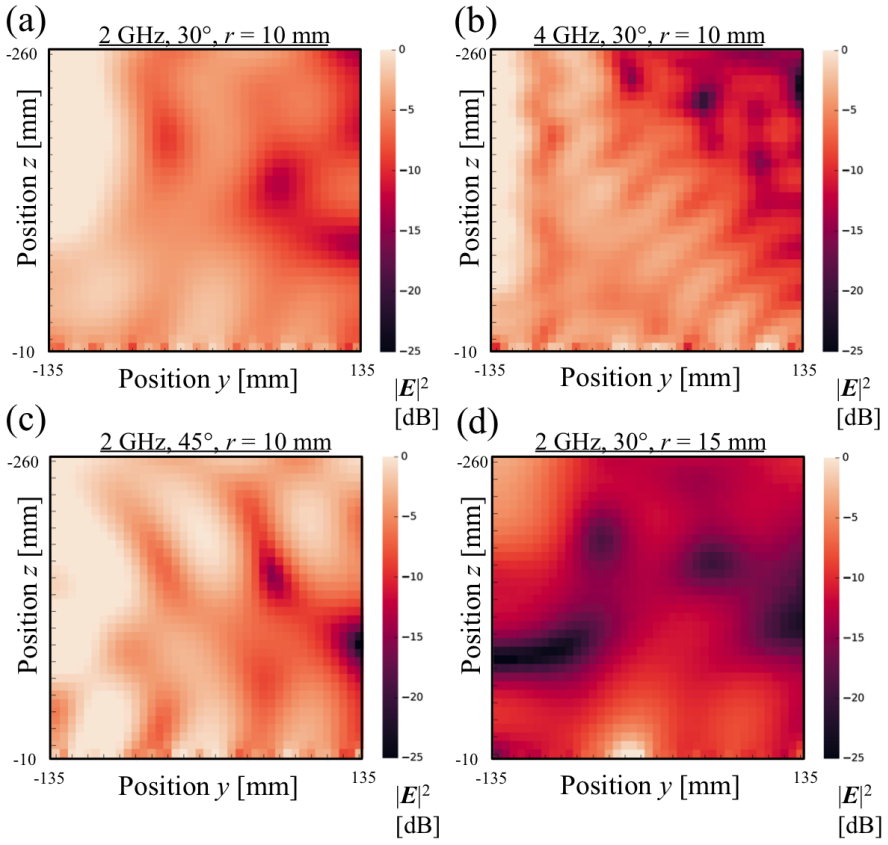

Figure 5.3: Frequency, structural-parameter, and angular characteristics of scattering patterns.

of the scatterers increases, and more striking scattering patterns are also thought to be generated as the effective refractive index increases. These observations confirm the expectation from metamaterial theory that the scattering patterns generated by SPCS will display non-linear frequency and angular dependency [6, 7].

5.4 Scattering Pattern Detection Experiments

To detect the spatial distribution of signal intensities in scattering patterns, the experimental system shown in Fig. 5.4 was used. The transmitter antenna (double ridged horn antenna), emits electromagnetic waves into the SPCS with the two parallel plates. The scattering patterns generated in the SPCS are detected by the sensor (monopole antenna) as spatial distributions of electric signal intensities. Note that the SPCS used here is composed of cylindrical aluminum scatterers (N = 9) placed between two parallel plates. The two dielectric spacers are 3-mm thick, and are inserted in the spaces between the SPCS and the parallel plates. Electromagnetic absorbers are inserted on both sides of the SPCS to avoid invasion by other incident waves. The distance between the transmitter antenna and the SPCS is 3 m. The signals produced are measured by using a vector network analyzer, with the transmitter antenna considered Port 1 and the sensor Port 2. As the sensor is moved, signal intensities are obtained at (x, y, z) = (150, 0, 50) - (150, 0, 250) unites of mm at 10-mm increments as a sampling of the spatial distribution of S_{21}. The spatial distribution of various scattering patterns was obtained by changing frequencies in the range of 2 - 4 GHz, the incidence angle in the range of 0 - 30°, and the structural parameter of r/d. Frequency and angular dependencies of the spatial distributions are shown in Figs. 5.5 - 5.7.

Fig. 5.5 shows how the number of waves in the spatial distributions increases with increasing input signal frequency. On the other hand, in Fig. 5.6, it can also be seen that the number of waves in the spatial distributions decreases with increasing incidence angle. However, in both results, the number of waves in the spatial distributions are considered not to be proportional to the wavenumbers of incident waves. This fact indicates that the scattering phenomena generated by SPCS are singular phenomena, different from general diffractions. These tendencies are in good agreement with the

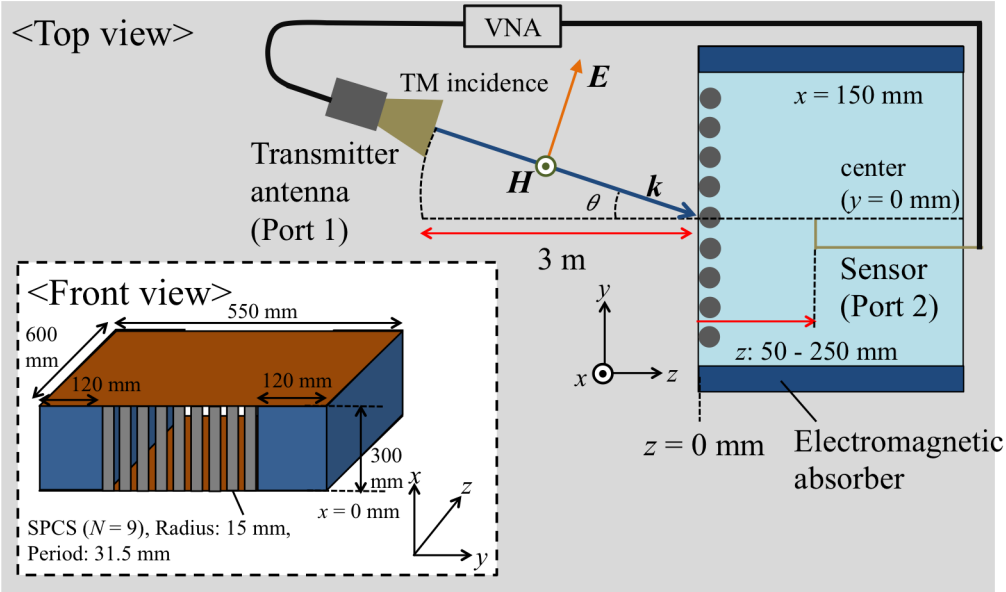

Figure 5.4: Experimental set up.

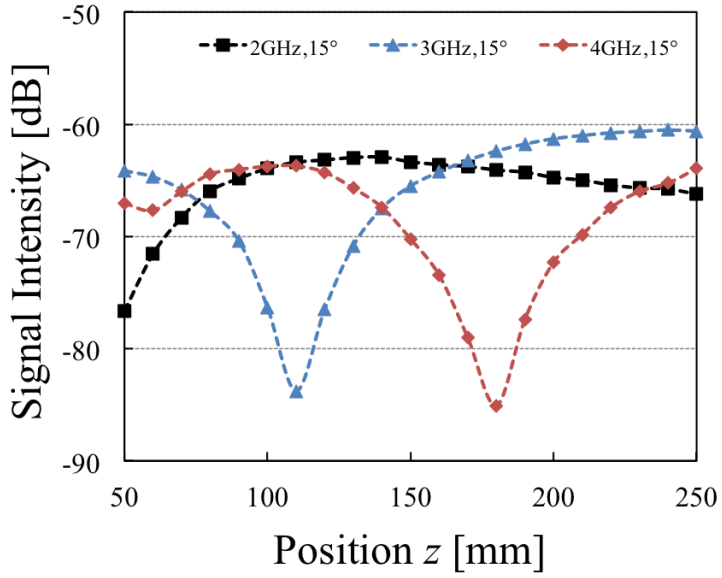

Figure 5.5: Frequency dependency of 1D spatial distributions of the scattering patterns.

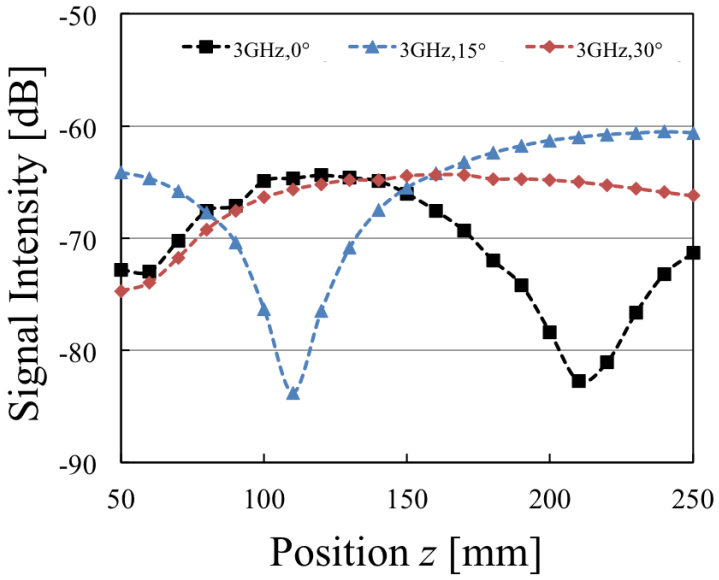

Figure 5.6: Angular dependency of 1D spatial distributions of the scattering patterns.

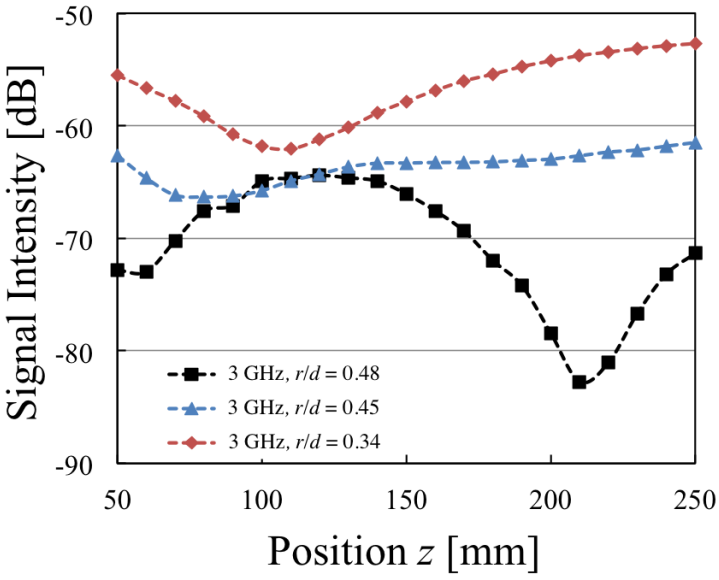

Figure 5.7: Structural parameter r/d dependencies of 1D spatial distributions of the scattering patterns.

analytical results. Although the contrast of the experimental spatial distributions is influenced by propagation losses, the maximum contrast of 25 dB is confirmed in the case of 3 GHz, 15° and this result shows that scattering patterns can be detected by sensors even in practical situations. Fig. 5.7 confirms that the contrast of the spatial distributions in the case of $r/d = 0.48$ is largest in these results. The results indicate that more scattering patterns are generated by SPCS as its effective refractive index increases, a fact that is consistent with the theoretical model.

5.5 Conclusions

A novel direction-of-arrival (DOA) estimation method that uses subwavelength periodic structures generated in conductive scatterers (SPCS) is proposed. In analytical studies, it is confirmed that significant scattering patterns are generated when a subwavelength periodic structure is used, and the patterns display frequency and angular dependencies. In experimental studies, the 1D spatial distributions of the scattering patterns in the SPCS are measured. Together with the analytical studies, this confirms that the spatial distributions also display frequency and angular dependencies that can be controlled by the structural parameters of the periodic structures. This indicates that the proposed method has the potential for use in a miniaturized, low cost, broadband DOA estimation device.

References

[1] M. Liang, X. Yu, R. S. Garcia, W. R. Ng, M. E. Gehm, and H. Xin, Proc. 2012 IEEE/MTT-S Int. Microw. Symp. Digest (IMS), QC, Canada, June (2012).

[2] R. Mueller and R. Lorch, Proc. 2015 9th Eur. Conf. Antennas Propag. (EuCAP), Lisbon, Portogal, April (2015).

[3] S. Yagitani, K. Katsuda, M. Nojima, Y. Yoshimura, and H. Sugiura, IEICE Trans. Commun. **E94-B**, 2306 (2011).

[4] G. Itami, Y. Toriumi, and Y. Akiyama, Proc. Int. Symp. Antennas Propag. (ISAP), Phuket, Thailand, Nov. (2017).

[5] Y. Tsuji, Y. Morita, and K. Hirayama, IEEE Photonics Tech. Lett. **18**, 2410 (2006).

[6] J. T. Shen, P. B. Catrysse, and S. Fan, Phys. Rev. Lett. **94**, 197401 (2005).

[7] F. J. G. Vidal, L. M. Moreno, and J. B. Pendry, J. Opt. A Pure Appl. Opt. **7**, S97 (2005).

Chapter 6

A Three-Layered Adjustable Frequency Selective Surface for Wireless Applications

6.1 Introduction

A frequency selective surface (FSS) is a two-dimensional periodic structure of conductive unit cells and works as a spatial filter; a surface that can select frequencies of transmitted or reflected waves. FSSs are expected to be widely used in wireless communication and EMC technologies, such as reflector antennas, radomes, and electromagnetic absorbers [1–3]. In recent years, since wireless communications have been developed and diversified in services like the fifth-generation mobile communication system (5G) and the Internet of Things (IoT), the frequency bands used and the number of communications devices such as mobile phones and laptop computers have increased rapidly. These devices often use multiple communication standards such as 4G, Wi-Fi, and 5G. Even when they use only one standard, multiple frequency bands are used for wireless communication. To improve their communication qualities, it is useful to employ reflectors with frequency selectivity in any specified wireless communication, because they can avoid disturbing other wireless communication environments as shown in Fig. 6.1.

In order to apply FSSs to such practical situations, they must be designed appropri-

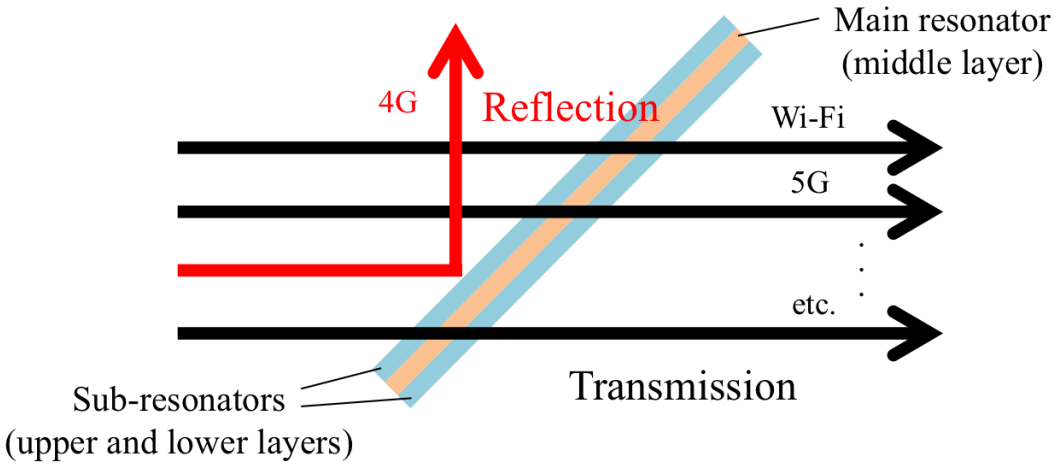

Figure 6.1: An example of the utility of a frequency selective surface as a reflector for complex wireless communication environments with multiple wireless standards.

ately in terms of simplicity and reproducibility. Therefore, equivalent circuit approaches have been studied and developed to express their electromagnetic behavior more simply and with higher precision [4–13]. Their angular stability is also essential for use in practical situations and has been studied as well in the above approaches. Conventional work has found that the angular stability is closely related to the size of an FSS unit cell in terms of its operating wavelength [14–20]. This indicates the importance of FSS-miniaturization [10–20].

However, in practice, since the frequency bands used vary with location and situation, a single-band FSS cannot deal with such variety. Therefore, various types of single-band FSS or a multiband FSS are required, when we use conventional techniques. If various single-band FSSs are used for communication, more different designs must be used, adding to the cost and effort. On the other hand, if a multiband FSS is used, disturbance of other wireless communication environments becomes a concern, since the FSS may act as an unintentional reflector of untargeted frequency bands in another wireless network.

As one of the advanced techniques to deal with these situations, a tunable FSS has already attracted significant attention and research. Most common tuning techniques focus mainly on inserting active circuit elements such as varactor diodes and micro electro mechanical systems (MEMS) to vary the capacitance components of FSSs by

applying an optimal voltage [21–32]. And as methods with no active elements required, the technique of combining an FSS with a conductive liquid in the dielectric tube array in multilayers or with liquid metal and a carrier fluid [33,34], and the technology to bend an FSS into an origami-like structure [35, 36]have both been reported.

However, using the above techniques in active elements presents practical disadvantages in terms of running cost due to the need for an external power supply. The above techniques that do not use active elements also suffer from several disadvantages, especially for mass production application, since they are costly to fabricate. Furthermore, real-time tuning based on the above techniques is not necessarily required, depending on the situation [37–39]. However, there is an alternate and simpler method, which is to change capacitance by varying the overlap ratio of two or more layers of FSSs. Although this can adjust the resonant frequency without requiring a complicated configuration or a power supply, the FSS characteristics in vertical and horizontal polarizations cannot be guaranteed because of structural variations in the frequency-adjustment.

In this study we propose a three-layered adjustable frequency selective surface as a simple adjusting method that keeps the characteristics of vertical and horizontal polarized waves the same. The FSSs are composed of a main resonator as the middle layer and two sub-resonators as the upper and lower layers, all overlaid on each other. By shifting the layers symmetrically, the operating frequency can be controlled over a broad range while keeping the polarization-equivalence. Also the FSSs can be fabricated easily and don't require electronic elements such as a varactor diode for the frequency-adjustment. Furthermore, the FSSs preserve angular stability because of their miniaturized design.

The proposed FSS is designed and fabricated as a single-band reflector, the operating frequency of which can be varied from 2.1 GHz to 3.6 GHz, giving it a wide range of applications. Although the frequency band used is different for each situation, the FSS does not require restructuring in order to adjust its frequency, as it adjusts optimally for each frequency band simply by altering the operating frequency by shifting its layers appropriately. Thus it enables us to reduce the cost and effort otherwise required for redesigning, while limiting the influence on the different waves used for other wireless communications.

In the following sections, the technical concepts of the FSS are introduced and the analytical and experimental results on the frequency characteristics of the FSS are reported. In Sec. 6.2, the operating principle of the FSS is described with the use of an equivalent circuit applied to a miniaturized-element FSS. In Sec. 6.3, electromagnetic analyses are conducted to examine the adjustment capability and polarization-equivalence and angular stabilities. In Sec. 6.4, we use FSSs fabricated by simply stacking and shifting three-layered films made with a silver ink printer, in experimental demonstrations to confirm their adjustment capability and angular dependencies.

6.2 Operational Principle of Adjustable Frequency Selective Surfaces

In this study, the adjustment capability of the proposed FSS is based on the variability of capacitance in its unit cell as well as on conventional studies [21–39]. Therefore, the operating principle of the FSSs can be expressed by considering the correspondence between the structure and an equivalent circuit.

One design of the FSS is shown in Fig. 6.2. The FSS consists of a loop-like main resonator in the middle layer, and two patch-like sub-resonators in the upper and lower layers. The equivalent circuit model involving only the main resonator is expressed as the simple LC resonant circuit shown in Fig. 6.3a. In this circuit, the inductance comes from the sides of the loop and the capacitance comes from the gap between the loops. However, when the patch of a sub-resonator is placed above and below the four corners of the square loops of the main resonator, more capacitors are formed, originating in the gaps between layers as shown in Fig. 6.3b, corresponding to the FSS ' s circuit. The resonant frequency of the FSS is expressed as below by using the lumped parameters shown in Fig. 6.3b [5].

$$L_{\mathrm{m}} = \mu_0 \frac{p}{2\pi} \log \frac{1}{\sin\left(\frac{\pi w}{2p}\right)} \tag{6.1}$$

$$C_{\mathrm{m}} = \epsilon_0 \frac{2(p-g)}{\pi} \log \frac{1}{\sin\left(\frac{\pi g}{2p}\right)} \tag{6.2}$$

$$f_{\mathrm{t}} = \frac{1}{2\pi\sqrt{L_{\mathrm{m}}(C_{\mathrm{m}} + C_{\mathrm{s}})}} \tag{6.3}$$

Where L_{m} and C_{m} are an inductance and a capacitance of a unit cell in a main resonator, C_{s} is an additional synthetic capacitance formed by the sub-resonators in upper and lower layers. And C is the total capacitance of the unit cell, ϵ_0 and μ_0 are respectively the permittivity and permeability in free space. As shown in Fig. 6.4a and Fig. 6.4b, by shifting the upper and lower layers relative to the middle layer in mutually opposite directions by the same distance d (for x- and y- directions), the value of C_{s} can be changed while retaining the circuit-equivalency for both vertical and horizontal polarizations. The correspondence between the parameters and the FSS unit cell is shown in Fig. 6.4a, and the correspondence between the three additional capacitances (C_{s1}, C_{s2}, and C_{s3}) in the FSS unit cell and its equivalent circuit is shown in Fig. 6.4b. Since the equivalent circuit model is the same for both polarizations, the resonant frequency of both polarizations can be controlled while keeping the same value. This mechanism is realized by a construction that maintains the symmetrical movement of the two sub-resonators. The additional capacitances can be expressed as follows by using a value of d. Note that the following expressions of the capacitances are varied in accordance with the variation of d because the outer corner of a sub-resonator exceeds the inner corner of the main resonator if d takes a value larger than the threshold. Also, the value of d is varied by keeping the condition that the inner corner of a sub-resonator must not move beyond the inner corner of the main resonator.

In the range of $d < c - \frac{1}{2}(a - g)$,

$$C_{\mathrm{s1}}(d) = \epsilon_{\mathrm{r}}\epsilon_0 \frac{1}{t}\left[\frac{1}{2}(a - g) - d\right]^2, \tag{6.4}$$

$$C_{\mathrm{s2}}(d) = \epsilon_{\mathrm{r}}\epsilon_0 \frac{1}{t}\left[\frac{1}{2}(a - g) + d\right]\left[\frac{1}{2}(a - g) - d\right], \tag{6.5}$$

$$C_{\mathrm{s3}}(d) = \epsilon_{\mathrm{r}}\epsilon_0 \frac{1}{t}\left[\frac{1}{2}(a - g) + d\right]^2, \tag{6.6}$$

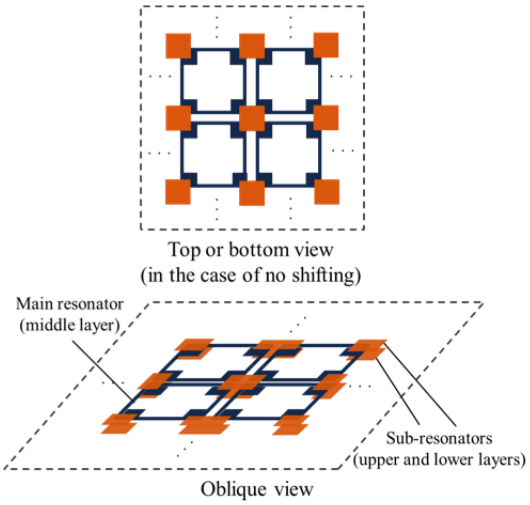

Figure 6.2: Design of the proposed FSS, which is composed of the main resonator in the middle layer and the sub-resonators in the upper and lower layers.

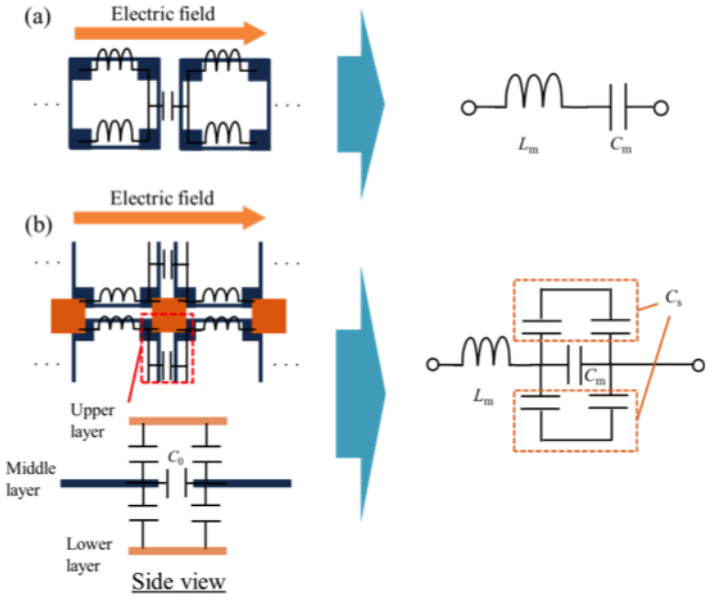

Figure 6.3: Operating principle of the proposed FSS when using only the main resonator (a) and the main and sub-resonators.

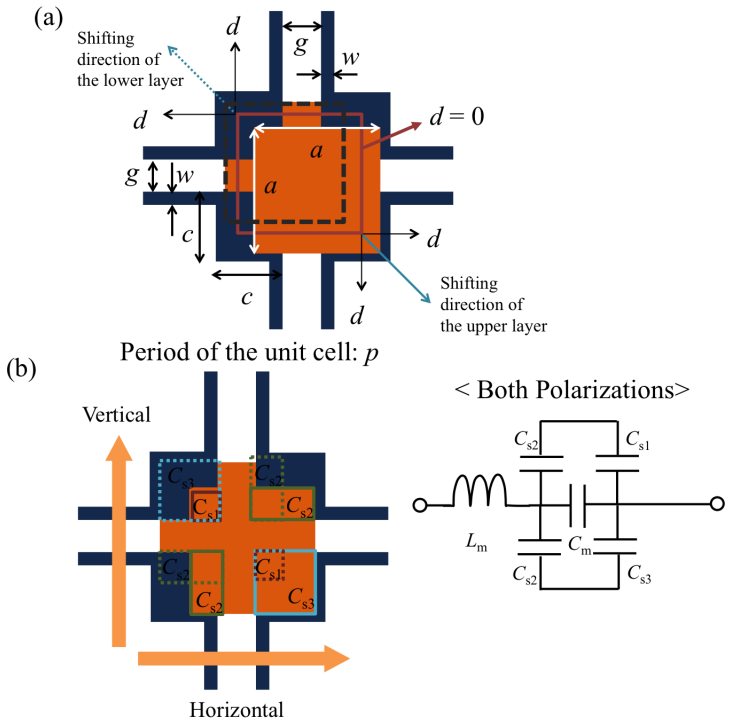

Figure 6.4: Correspondences between (a) the parameters and the FSS structure, and (b) the FSS structure and the equivalent circuit for both polarizations.

$$C_{\mathrm{s}}(d) = (C_{\mathrm{s1}}//C_{\mathrm{s2}}) + (C_{\mathrm{s2}}//C_{\mathrm{s3}}) = \epsilon_{\mathrm{r}}\epsilon_0 \frac{1}{t}[\frac{1}{2}(a-g)+d][\frac{1}{2}(a-g)-d]. \tag{6.7}$$

In the range of $c - \frac{1}{2}(a-g) \leq d \leq \frac{1}{2}(a-g)$,

$$C_{\mathrm{s1}}(d) = \epsilon_{\mathrm{r}}\epsilon_0 \frac{1}{t}[\frac{1}{2}(a-g)-d]^2, \tag{6.8}$$

$$C_{\mathrm{s2}}(d) = \epsilon_{\mathrm{r}}\epsilon_0 \frac{1}{t}c[\frac{1}{2}(a-g)-d], \tag{6.9}$$

$$C_{\mathrm{s2}}(d) = \epsilon_{\mathrm{r}}\epsilon_0 \frac{1}{t}c^2, \tag{6.10}$$

$$C_{\mathrm{s}}(d) = (C_{\mathrm{s1}}//C_{\mathrm{s2}}) + (C_{\mathrm{s2}}//C_{\mathrm{s3}}) = \epsilon_{\mathrm{r}}\epsilon_0 \frac{1}{t}c[\frac{1}{2}(a-g)-d]. \tag{6.11}$$

Here ϵ_{r} and t are the relative permittivity and the thickness of the FSS substrate, respectively. Eqs. 6.3 - 6.11 indicate that the resonant frequency f_{t} can be controlled by the distance d. In other words, although these FSSs are composed of one type of main resonator and sub-resonator, they can be used as different spatial filters with variable operating frequencies without re-designing, if a mechanism is provided to vary the distance d.

6.3 Analytical Studies of an Adjustable Frequency Selective Surface

In order to examine the operating principles of the FSS discussed in Sec. 6.2, numerical analyses are conducted by using an electromagnetic simulator (HFSS, R19). The model of the FSS analyzed is shown in Fig. 6.5. To compare the analysis with experimental results, it is assumed that the conductive material used for the FSS is silver from inkjet printing (conductivity: 2230000 Ω^{-1} m^{-1}), and that conductive patterns with thickness $m = 1.3$ μm are set on PET-substrates with thickness $t = 0.125$ mm. The parameters of the analyzed model are shown in Table 1. As shown in Fig. 6.5, the FSS unit cell is composed of the three layer-substrates, with a periodic boundary condition applied to the sides of the analyzed model. Incident waves are assumed to enter the top side (Port 2) from the bottom side (Port 1) with an incident angle θ. Note that the direction of the incident electric field at normal incidence is the y-direction, and the incident angle is changed in an x-z plane (TE) or a y-z plane (TM) in the model. Under the above conditions, transmission characteristics (S_{21}) are analyzed by changing the values of d and θ at the different polarizations (vertical and horizontal, or TE and TM).

First, the distance dependency of resonant frequency f_{t} is investigated in two cases: vertical and horizontal at normal incidence. These results are shown in Fig. 6.6.

Note that the theoretical curve is derived by substituting the structural parameters of the FSS model into Eqs. 6.3, 6.7, and 6.11, and the analytical values of resonant frequencies f_{t} are obtained from the analytical results of S_{21}. The adjustment capability is defined as the ratio between the minimum and maximum resonant frequencies of the

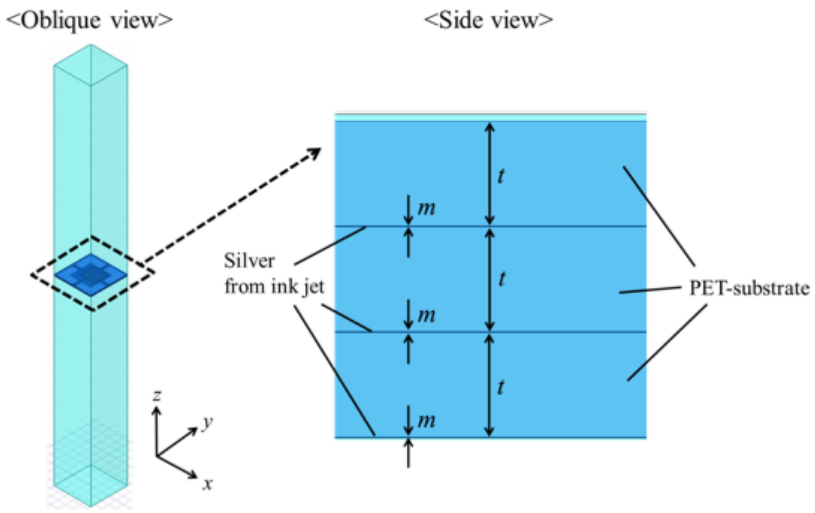

Figure 6.5: Analyzed model of the FSS which possesses three conductor parts with thickness m and three PET substrates with thickness t.

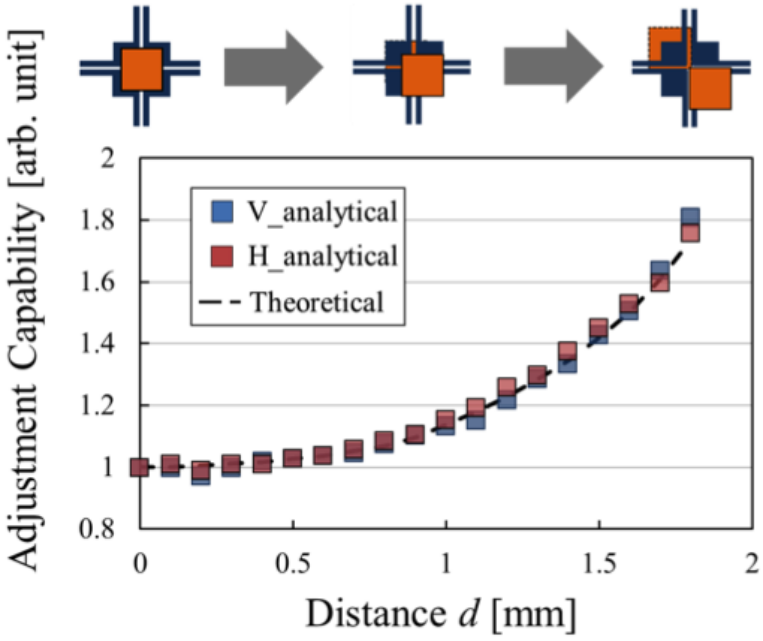

Figure 6.6: Distance dependence of the adjustment capability of the FSS.

Table 6.1: Parameter Settings

Parameter	Value
p	10 mm
c	2.75 mm
a	4 mm
g	0.2 mm
w	0.2 mm
t	0.125 mm
m	1.3 μm
d	0 – 1.8 mm
θ	0 – 60 degree (TE, TM)

proposed FSS achievable by adjustment, and is obtained by determining the ratio of each value and the fundamental value corresponding to the case of $d = 0$ in both the theoretical and analytical cases. In Fig. 6.6, the result confirms that the analytical results for both polarizations are in good agreement with the theoretical curve. These results show that the FSS can be operated by equivalent circuits as shown in Fig. 6.4b. Specifically, the resonant frequency can be changed from f_0 to approximately 1.7 f_0 by varying the capacitance C_s from 0.060 pF to 0.793 pF. Note that f_0 is defined as the lowest resonant frequency, and the values of the inductance L_m and the capacitance C_m are fixed as 6.476 nH and 0.302 pF, respectively. This adjustment capability is comparable or superior to that in conventional studies [21–39]. Also, this is considered to be an optimal range, since if the area of the sub-resonator is larger, the range of distance-variation is narrowed, and if the area of the sub-resonator is smaller, the adjustment capacity of C_s is less effective. In designing the FSS, to retain its adjustment capability it is best to use thin substrates. In this study, considering the workability and cost, substrates 0.125 mm thick were used. Here, it should be emphasized that the requirements of the FSS can be realized by any dielectric substrate and any conductor.

The analytical results in the case of vertical polarization and the circuit simulation results of transmission characteristics (S_{21}) were compared, as shown in Fig. 6.7. Note that the equivalent circuit model shown in Fig. 6.8 is used for the circuit simulation. The inductance L_m and C_m in the cases of $d = 0$ - 1.8 mm are set as the fixed values

of 3.0 nH and 0.5 pF respectively, to best match the analytical results. Quantitative consistency between the analytical results and the results of circuit simulations is difficult because the structural interaction between inductances and capacitances in the FSS cannot be derived strictly [5]. The values of the variable capacitance C_s in all the cases are respectively 1.4 pF, 1.32 pF, 0.96 pF, 0.438 pF, and 0.15 pF. The results shown in Fig. 6.7 show good agreement in all cases, indicating that the proposed equivalent circuit model is qualitatively consistent with the electromagnetic behavior of the analytical FSS model. The analytical result also confirms that the attenuation is kept at around 30 dB over the full range of d. Another point of view suggests that no other resonant mode exists in each curve. This indicates that since the unit cell does not have long wires and bent lines such as meander lines, unintentional resonant modes are considered not to be significantly excited.

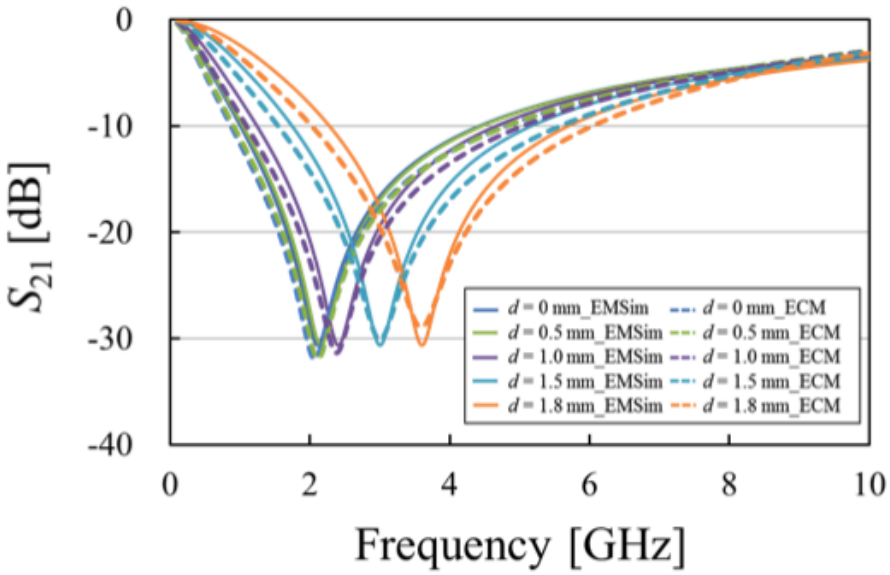

Figure 6.7: Distance d dependence of S_{21} of the FSS in the case of normal incidence (vertical) compared to the corresponding numerical simulation results in the equivalent circuit model.

The angular dependence of the FSS was also investigated in TE and TM polarizations. The model values of $d = 0$ mm and $d = 1.8$ mm are used, and the incident angle θ is changed from 0 to 60 degrees in both polarizations. The results are shown in Figs. 6.9 - 6.12.

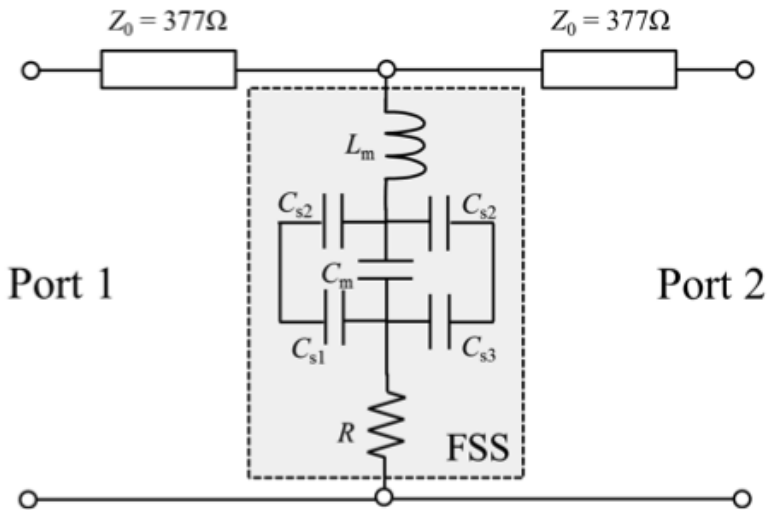

Figure 6.8: Equivalent circuit model for numerical simulation of frequency responses of S_{21} for comparison with the results of the electromagnetic analyses.

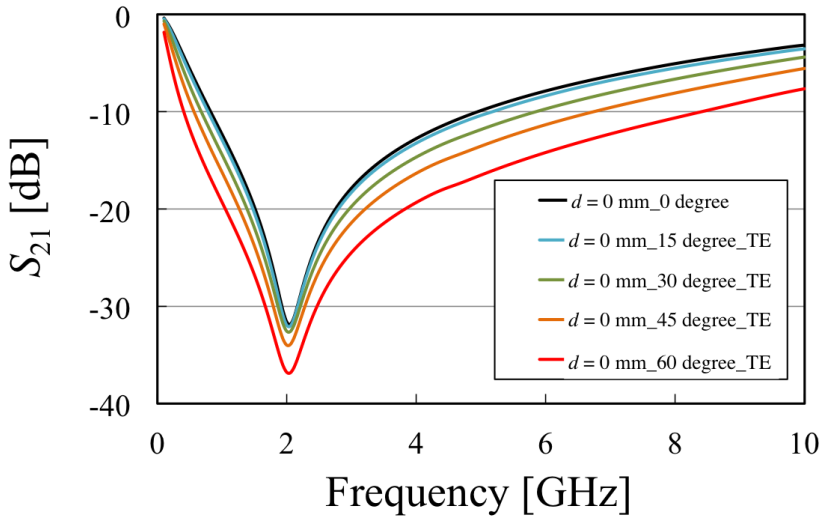

Figure 6.9: Angular dependence of S_{21}-frequency characteristics of the FSS with $d = 0$ mm and TE incidence.

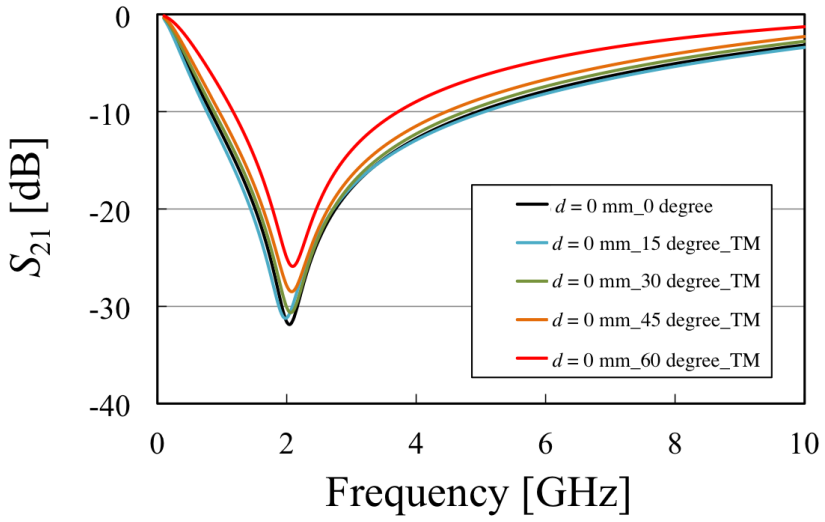

Figure 6.10: Angular dependence of S_{21}-frequency characteristics of the FSS with $d = 0$ mm and TM incidence.

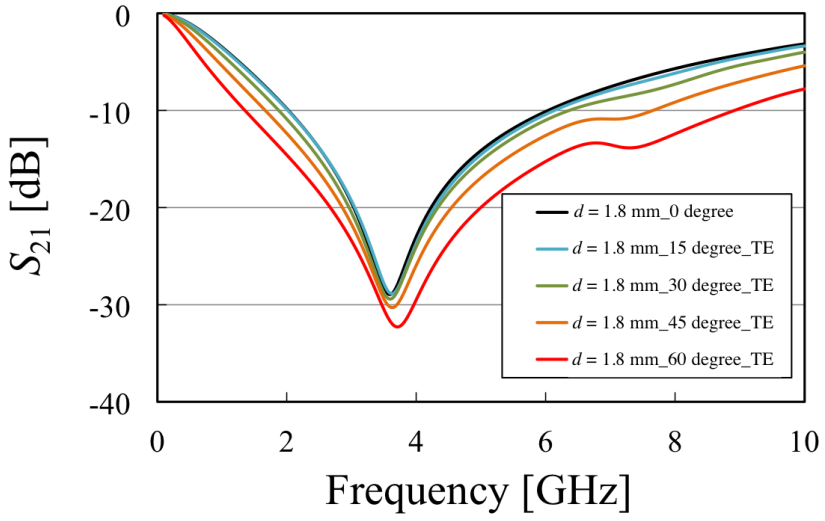

Figure 6.11: Angular dependence of S_{21}-frequency characteristics of the FSS when $d = 1.8$ mm and TE incidence.

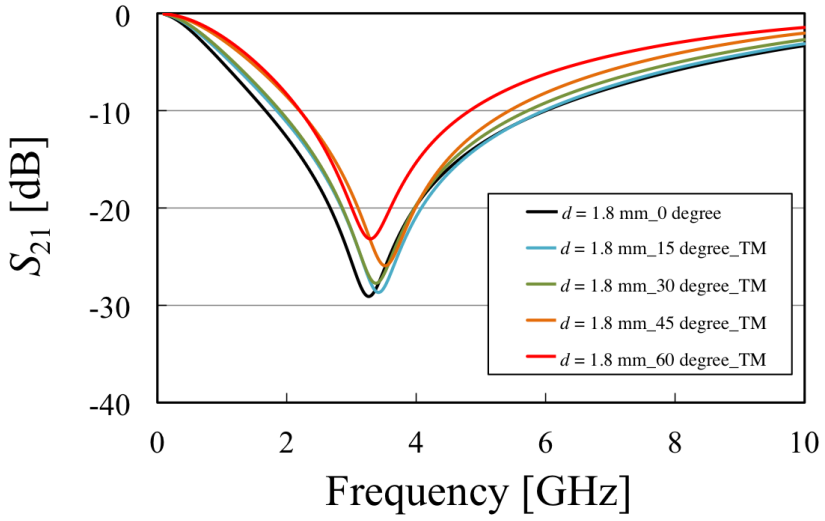

Figure 6.12: Angular dependence of S_{21}-frequency characteristics of the FSS when d = 1.8 mm and TM incidence.

In Figs. 6.9 - 6.12, these results confirm the angular stability of the FSS for both polarizations. The angular stability is considered to originate in the size of the FSS relative to its resonant wavelength. The resonant wavelengths of the FSSs in the two cases are 0.066 λ and 0.125 λ respectively. Thus, since their unit cells are sufficiently small compared to their resonant wavelengths, good angular stability can be obtained, and other modes such as grating lobes are considered to be suppressed, as is indicated in related studies [14–20]. And since the thickness of the FSS is an essential factor in retaining its angular stability, thinner substrates are more desirable in FSSs.

6.4 Experimental Studies on an Adjustable Frequency Selective Surface

In this section, the adjustment capability and angular stability of the FSS are demonstrated experimentally. The FSS samples were fabricated by stacking three PET substrates on which the resonator patterns were printed with a silver ink printer. The substrates were A4-size (210 mm $\times$ 297 mm) and the main parameters such as resonator size are the same as the analytical model in Sec. 6.3. The fabricated samples and experimental setup are shown in Fig. 6.13 and Fig. 6.14, respectively. Measurements

were conducted in a shielded room, and electromagnetic absorbers were set around the aperture and behind the two antennae in the room to prevent multiple reflections. Electromagnetic waves in the range of 1 - 9 GHz were introduced to the samples by the transmitter antenna (double ridged horn antenna, 3115, ETS-Lindgren), and the transmitted waves were detected by the receiver antenna (the same product as the transmitter antenna). Thus, S_{21} measurements were made with a VNA (E8364B, Agilent Technologies) and transmission coefficients were calculated by taking the difference between the S_{21} result and the reading without the samples. The incident angle of the entering waves was changed by rotating the aperture and the transmitter antenna. Note that the antenna was rotated around the radiating direction only when the polarization condition was changed (TE polarization: 0 degrees, TM polarization: 90 degrees). The experimental transmission coefficients were compared to the analytical S_{21}-results at normal incidence in order to examine the adjustment capability by varying the value of d in the experimental samples. This result is shown in Fig. 6.15. Also, their incident angle dependencies were examined by changing the incident angle of TE and TM polarizations. These results are shown in Figs. 6.16 - 6.19.

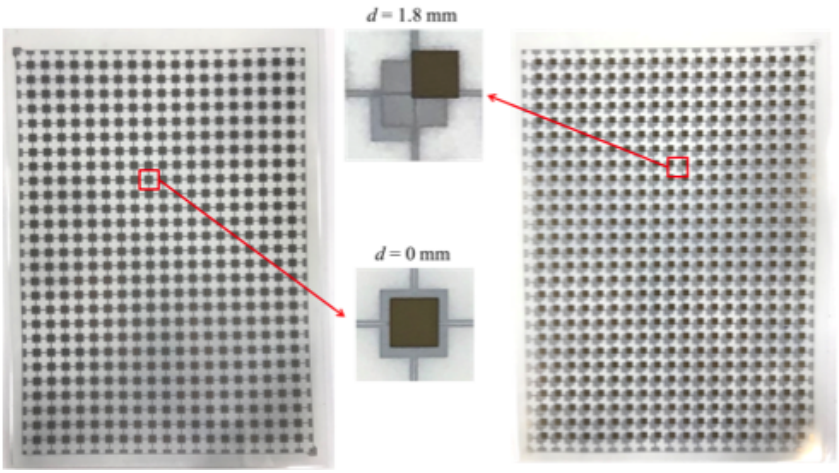

Figure 6.13: The fabricated FSSs ($d = 0.1$ mm and 1.8 mm) consisted of three conductor parts with thickness m =1.3 μm and three PET substrates with thickness $t = 0.125$ mm.

In Fig. 6.15, the experimental results display good agreement with the analytical results. Although the differences between experimental and analytical results are considered to be caused by the error of shifted distance d in fabrication, the experimental

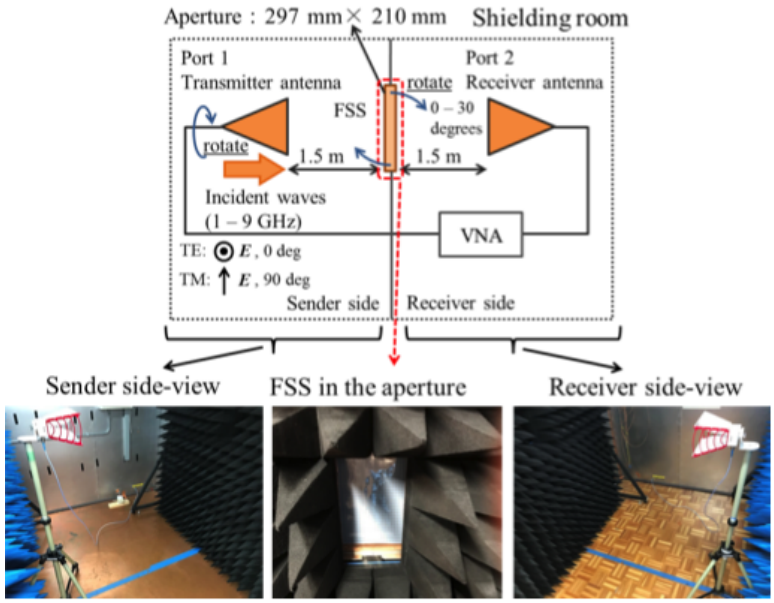

Figure 6.14: Experimental setup in a shielded room, with electromagnetic absorbers near the FSS and around both antennae.

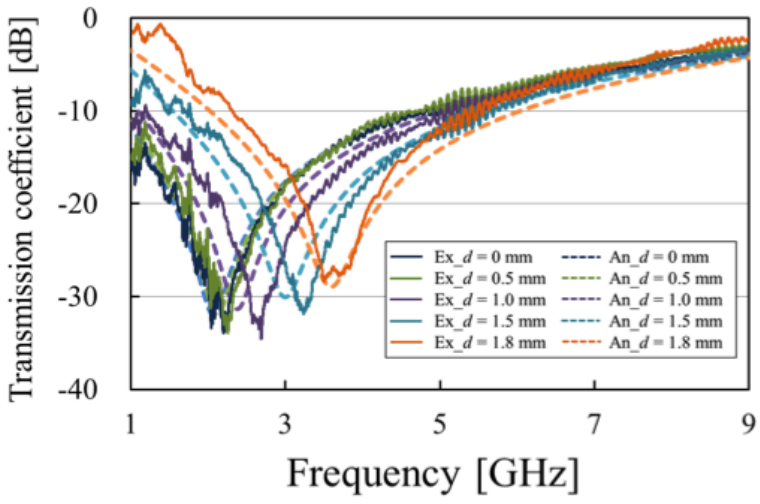

Figure 6.15: Comparison of experimental and analytical results for transmission coefficients of the proposed FSS with normal incidence.

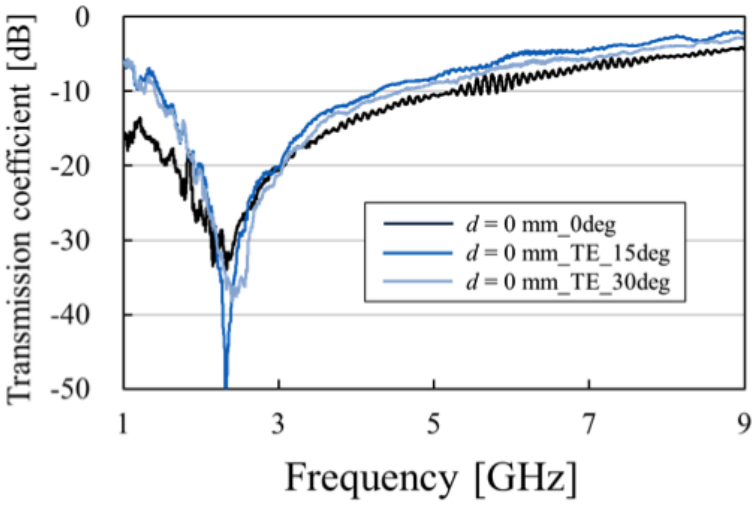

Figure 6.16: Angular dependence of transmission coefficients of the proposed FSS for $d = 0$ mm and TE incidence.

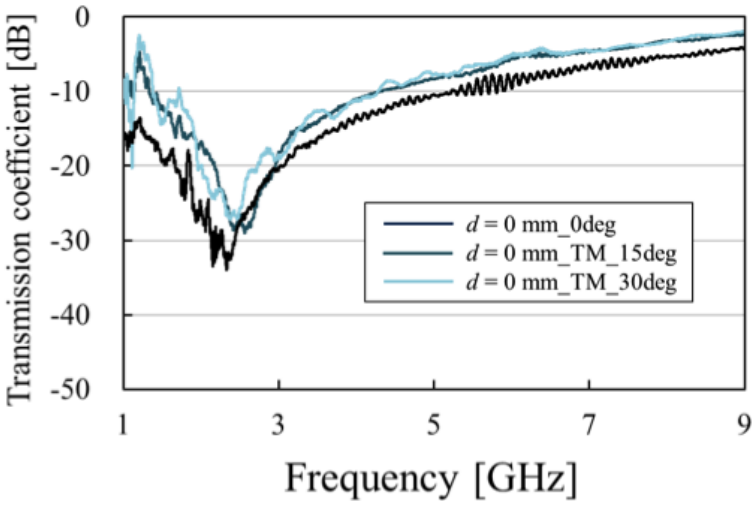

Figure 6.17: Angular dependence of transmission coefficients of the proposed FSS for $d = 0$ mm and TM incidence.

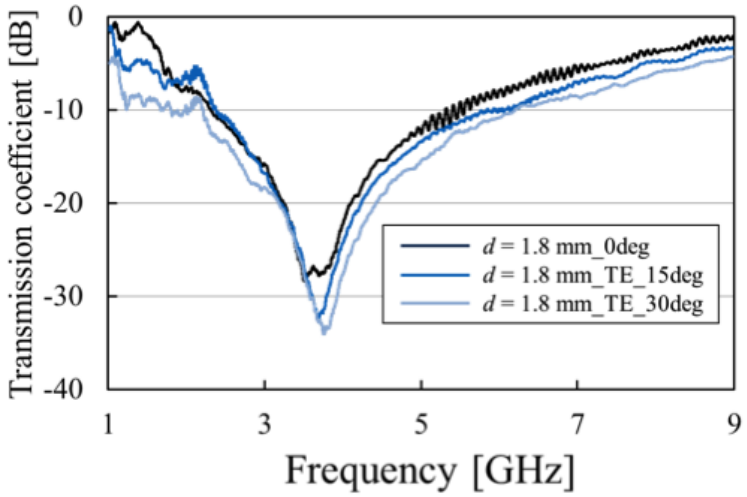

Figure 6.18: Angular dependence of transmission coefficients of the proposed FSS for $d = 1.8$ mm and TE incidence.

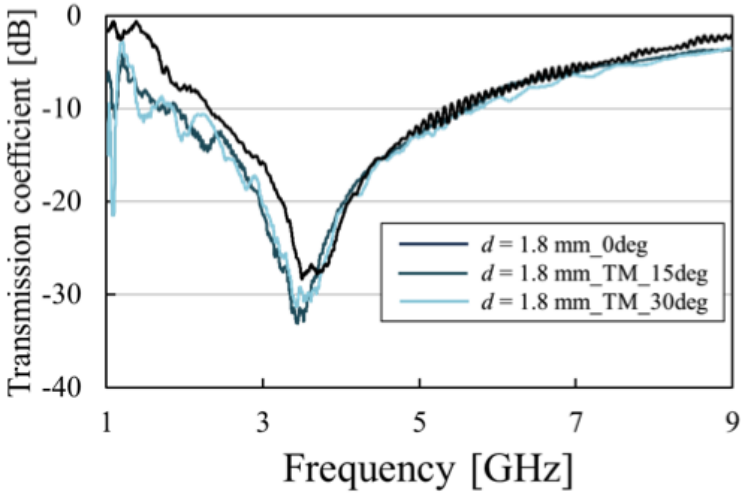

Figure 6.19: Angular dependence of transmission coefficients of the proposed FSS for $d = 1.8$ mm and TM incidence.

results show that the operating frequency of the FSS can actually be controlled by changing the distance d. Since the resonant frequency is varied from approximately 2.1 GHz to 3.6 GHz, the experimental adjustment capability is from f_0 to approximately 1.7 f_0, a range that is almost consistent with the theoretical curve shown in Fig. 6.6. Therefore, if the lowest resonant frequency f_0 is set to 1.5 GHz, the operating frequency bands that the FSS can actually cover include GPS, Wi-Fi, and LTE bands, since the covered frequencies range from 1.5 GHz to approximately 2.55 GHz. Also, the result confirms that all the samples have sufficient attenuation of around 30 dB at the resonant frequency bands. And the distance-dependencies of the attenuation at the resonant frequencies expected from the analytical results are also demonstrated, in that the attenuation is decreased slightly as the distance d increases. From Figs. 6.16 - 6.19, all the samples show angular stability in TE and TM polarizations over a range of 0 - 30 degrees. Since the experimental results are consistent with the analytical results, the samples are considered to have angular stability over a range of 0 - 60 degrees. In Fig. 6.16 and Fig. 6.17, although the attenuation varies significantly with the change of incidence angle, the tendency of each polarization condition is consistent with the analytical results as shown in Fig. 6.9 and Fig. 6.10. Namely, the attenuations with TE polarization are larger than with normal incidence, and with TM polarization, they are smaller than that with normal incidence. Also, in Fig. 6.18 and Fig. 6.19, the tendency in the attenuation of each polarization condition is consistent with the analytical results as shown in Fig. 6.11 and Fig. 6.12 in terms of the small variance of the attenuations.

From the discussion in the experimental results, in practical situations, the demonstrated FSS can be applied as a functional reflector, the operating frequency of which can be adjusted to different wireless communication bands by placing marks in the upper and lower substrates to include the distance corresponding to each of the targeted frequency bands. If the targeted wireless communication standard with multiple frequency bands is in the range from 2.1 GHz to 3.6 GHz in a specified use situation, the FSS can be adjusted to the optimal frequency band regardless of the location used, without re-designing.

6.5 Conclusions

A three-layered adjustable frequency selective surface is proposed. The proposed FSS is composed of a main resonator in the middle layer and two sub-resonators in the upper and lower layers. In the FSS, its resonant frequencies for vertical and horizontal polarizations can be controlled while keeping the same resonant frequency in both, by shifting the upper and lower layers symmetrically. Therefore, the FSS can be fabricated easily and achieves frequency adjustment capability without using electronic elements such as varactor diodes although the FSS is not suitable for a situation that requires real-time tuning.

The analytical results confirm that the resonant frequency can be varied from f_0 to approximately 1.7 f_0 with polarization-equivalence and that there is good angular stability in the range of 0 - 60 degrees.

In the experiments, FSS samples with the same profiles as the analytical models were fabricated simply by using a silver ink jet printer, and their adjustment capability and angular stability were demonstrated. The experimental results also confirm the analytical results by showing that almost the same adjustment capability and good angular stability are realized in TE and TM polarizations. Therefore, the FSS has usability potential in wireless applications such as a frequency-selective reflector for various wireless communication bands.

References

[1] S. M. Amin, M. H. Abadi, K. Ghaemi, and N. Behdad, IEEE Trans. Antennas Propag. **63**, 534 (2015).

[2] J. H. Kim, H. J. Chun, I. P. Hong, Y. J. Kim, and Y. B. Park, IEEE Trans. Antennas. Wireless Propag. Lett. **13**, 868 (2014).

[3] K. Zhang, W. Jiang, and S. Gong, IEEE Trans. Antennas. Wireless Propag. Lett. **16**, 2856 (2017).

[4] G. Itami, Y. Toriumi, and Y. Akiyama, Proc. Int. Symp. Antennas Propag. (ISAP), Phuket, Thailand, Nov. (2017).

[5] K. Sarabandi and N. Behdad, IEEE Trans. Antennas Propag. **55**, 1239 (2007).

[6] A. R. Varkani, Z. H. Firouzeh, and A. Z. Nezhad, IET Microw. Antennas Propag. **12**, 749 (2018).

[7] A. K. Zadeh and A. Karlsson, IEEE Trans. Antennas Propag. **57**, 2307 (2009).

[8] G. H. Dadashzadeh, M. H. Amini, and A. R. Mallahzadeh, J. Commun. Eng. **3**, 23 (2014).

[9] B. A. Munk, *Frequency-Selective Surfaces: Theory and Design* (Wiley, 2000).

[10] M. Moallem and K. Sarabandi, IEEE Trans. Antennas Propag. **2**, 333 (2012).

[11] S. Mohamad, A. M. H. Abani, and N. Bahdad, IEEE Trans. Antennas Propag. **63**, 4766 (2015).

[12] P. C. Zhao, Z. Y. Zong, W. Wu, and D. G. Fang, IEEE Trans. Antennas Propag. **64**, 2963 (2016).

[13] P. C. Zhao, Z. Y. Zong, W. Wu, B. Li, and D. G. Fang, IEEE Trans. Antennas Propag. **65**, 4693 (2017).

[14] G. Itami, Y. Toriumi, and J. Kato, Proc. Asia-Pacific Microw. Conf. (APMC), Kyoto, Japan, Nov. (2018).

[15] S. N. Azemi, K. Ghorbani, and W. S. T. Rowe, IEEE Microw. Wireless Compon. Lett. **25**, 454 (2015).

[16] C. N. Chiu and K. P. Chang, IEEE Trans. Antennas. Wireless Propag. Lett. **8**, 1175 (2009).

[17] M. A. A. Joumayly and N. Behdad, IEEE Trans. Antennas Propag. **58**, 4033 (2010).

[18] R. Natarajan, M. Kanagasabai, S. Baisakhiya, R. Sivasamy, S. Palaniswamy, and J. K. Pakkathillam, IEEE Trans. Antennas. Wireless Propag. Lett. **12**, 718 (2013).

[19] Z. Zhao, H. Shi, J. Guo, and A. Zhang, IEEE Trans. Antennas. Wireless Propag. Lett. **16**, 553 (2016).

[20] T. Hong, W. Xing, Q. Zhao, Y. Gu, and S. Gong, IEEE Trans. Antennas. Wireless Propag. Lett. **17**, 547 (2018).

[21] F. Bayatpur and K. Sarabandi, IEEE Trans. Antennas Propag. **57**, 1433 (2009).

[22] X. Zeng, L. Zhang, G. Wan, B. Hu, B. Huang, and J. Shen, Proc. Int. Symp. Antennas Propag. EM Theory (ISAPE), Gulin, China, Oct. (2016).

[23] A. Tennant and B. Chambers, IEEE Microw. Wireless Compon. Lett. **14**, 46 (2004).

[24] M. Bouslama, M. Traii, T. A. Denidni, and A. Gharsallah, IEEE Trans. Antennas. Wireless Propag. Lett. **15**, 1159 (2015).

[25] D. F. Sievenpiper, J. H. Schaffner, H. J. Song, R. Y. Loo, and G. Tangonan, IEEE Trans. Antennas Propag. **51**, 2713 (2003).

[26] F. Costa, A. Monorchio, S. Talarico, and F. Michele, IEEE Trans. Antennas. Wireless Propag. Lett. **7**, 676 (2008).

[27] A. Munir and A. M. Huring, Proc. Int. Conf. Info. Tech. Comp. EE. (ICITACEE), Semarang, Indonesia, Oct. (2015).

[28] L. Zhang, T. Ding, and T. Zhao, Proc. Int. Conf. Electromagn. Adv. App. (ICEAA), Velona, Italy, Sept. (2017).

[29] X. G. Huang, Z. Shen, Q. Y. Feng, and B. Li, IEEE Trans. Antennas Propag. **63**, 3297 (2015).

[30] W. Hu, R. Dickie, R. Cahill, H. Gamble, Y. Ismail, V. Fusco, D. Linton, N. Grant, and S. Rea, IEEE Microw. Wireless Compon. Lett. **17**, 667 (2007).

[31] B. Schoenlinner, A. A. Tamijani, L. C. Kempel, and G. M. Rebeiz, IEEE Trans. Microw. Theory Tech. **52**, 2474 (2004).

[32] A. Ebrahimi, Z. Shen, W. Withayachumnankul, S. F. Al-Sarawi, and D. Abbott, IEEE Trans. Antennas Propag. **64**, 1672 (2016).

[33] M. Li, B. Yiu, and N. Behdad, IEEE Microw. Wireless Compon. Lett. **20**, 423 (2010).

[34] B. J. Lei, A. Zamora, T. F. Chun, A. T. Ohta, and W. A. Shiroma, IEEE Microw. Wireless Compon. Lett. **21**, 465 (2011).

[35] S. A. Nauroze, L. Novelino, M. M. Tentzeris, and G. H. Paulino, Proc. IEEE MTT-S Int. Microw. Symp (IMS), Hawaii, USA, June (2017).

[36] K. Fuchi, J. Tang, B. Crowgey, A. R. Diaz, E. J. Rothwell, and R. O. Ouedraogo, IEEE Trans. Antennas. Wireless Propag. Lett. **11**, 473 (2012).

[37] X. J. Sheng, J. J. Fan, N. Liu, and C. B. Zhang, IEEE Microw. Wireless Compon. Lett. **27**, 915 (2017).

[38] B. Doken and M. Kartal, IEEE Trans. Antennas. Wireless Propag. Lett. **16**, 2979 (2017).

[39] K. Payne, K. Xu, and J. H. Choi, IEEE Trans. Microw. Theory Tech. **66**, 4783 (2018).

Chapter 7

Conclusions

In the thesis, electromagnetic control of the propagation condition on subwavelength periodic structures are discussed and their applications for various devices are reported, based on the theoretical concept of metamaterials. Specifically, first electromagnetic controls of propagation conditions in complementary subwavelength periodic structures are discussed, and the advanced technologies of SSPP, FSS, and artificial medium based on the discussion are applied to high-frequency devices for skin depth engineering, biomedical diagnosis and wireless communication.

In the study of electromagnetic controls of propagation conditions in the subwavelength periodic structures, the change of the propagation characteristics in accordance with the thickness of the structures is discussed by using the complementary structures of MHAs and MPAs. As a result, it finds that when the structures are treated as boundaries their propagation characteristics follow to Babinet ' s principle and MHAs and MPAs show the band-pass effects and band-stop effects, respectively. On the other hand, when the structures are treated as propagation media their propagation characteristics follow to the SSPP theorem and both structures show the band-pass effects. Therefore, the breakdown of Babinet ' s principle is demonstrated in the condition that the thickness is about a wavelength, analytically and experimentally. The studies give us a physical insight of electromagnetic behaviors in a subwavelength periodic structure in terms of the propagation control between a boundary surface, and an effective medium.

As a first application, a theoretical estimation method of skin depth of SSPPs in

millimeter or terahertz wavebands for suppressing near fields around transmission lines is proposed and examined theoretically and experimentally. Specifically, the formula of a skin depth of an SSPP is derived and the values at different frequencies are compared with the experimental values by measuring the skin depth of SSPPs with the use of an MHA and a conductor plate. As a result, it finds that the theoretical values of the skin depth of SSPPs are in good agreement with the experimental values.

Second, a novel imaging method of a simple biomedical diagnosis focusing on a dynamic control of SSPP modes on an MHA is proposed and examined analytically and experimentally. Specifically, first, the feasibility of detecting dielectric responses on an MHA is examined by an active control of local fields of SSPP modes intensified by a needle-like conductor. And two-dimensional imaging experiments of conductive, dielectric and biomedical samples by using the method are conducted. The results find that the permittivity distributions of all the samples including a lung of a rat can be obtained by using the method without requiring complex signal processing.

As wireless applications, a broadband and miniaturized devices for DOA estimations and a simplified adjustable FSS whose resonant frequency can be controlled in broadband, are proposed and examined.

As a DOA device, the subwavelength periodic structure of conductive scatterers for formations of scattering patterns of 2 - 6 GHz is designed and fabricated. The spatial distributions of the patterns in it at various frequencies and incident angles are analyzed and detected experimentally. Both results confirm the fact that the scattering patterns can be generated as standing waves near the SPCS, and find that the patterns show the variances responding to frequencies and angles of incident waves due to changes of tangential components of incident waves.

Finally, a three-layered adjustable FSS which resonates at various frequencies in accordance with its stacked conditions is designed and fabricated. The operating principle is based on the functional capacitances formed between the adjacent layers that can be varied by shifting the layers of each other. And the resonant frequency can be controlled using the designed value of the capacitances. This operating principle and the angular dependencies in the various cases are examined analytically and experimentally by ana-

lyzing and measuring the transmission characteristics. It confirms the good agreements between the analytical and experimental results in all the samples. And the FSS also shows good angular stability which is important in practical use.

Through these studies, the applicable potential of metamaterial technologies is expanded and the application targets of metamaterials are clarified. In other words, the studies revealed that metamaterial technologies can be applied to various devices used for high-frequency analog devices, biomedical diagnoses, and supporting methods of wireless communications. And as followed to the future direction of metamaterial-studies (Fig. 7.1), they enrich our future lives by innovating devices.

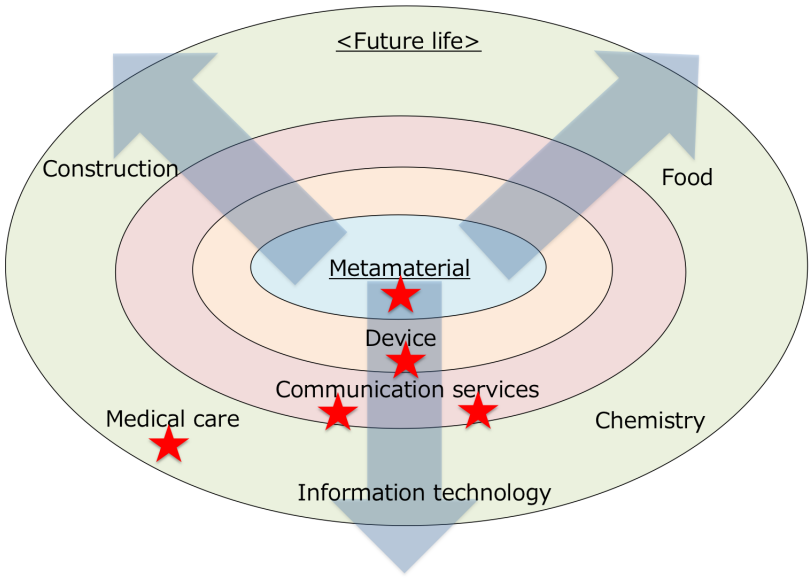

Figure 7.1: The future direction of metamaterial-studies

List of publications

Publications

- Journal papers
  - G. Itami and O. Sakai, "Analysis and Observation of the Breakdown of Babinet's Principle in Complementary Spoof Surface Plasmon Polariton Structures", Scientific Reports, under review, 2019: described in Chapter 2.
  - G. Itami and O. Sakai, "Symmetrical estimation method for skin depth control of spoof surface plasmon polaritons using dispersed waves from a metallic hole array", Journal of Applied Physics, Volume 125, Issue 21, 213101, 2019: described in Chapter 3.
  - G. Itami, O. Sakai, and Y. Harada, "Two-Dimensional Imaging of Permittivity Distribution by an Activated Meta-Structure with a Functional Scanning Defect", Electronics, Volume 8, Issue 2, 239, 2019: described in Chapter 4.
  - G. Itami, Y. Toriumi, and J. Kato, "A Three-Layered Adjustable Frequency Selective Surface for Wireless Applications", IEEE Transactions on Antennas and Propagation, Volume 67, Issue 12, 7407, 2019: described in Chapter 6.
- Proceeding of international conference (Refereed)
  - G. Itami, T. Iizuka, Y. Toriumi, J. Kato and O. Sakai, "Direction-of-Arrival Estimation from Scattering Patterns in a Subwavelength Periodic Structure of a Conductive Scatterer", International Symposium on Elec-

tromagnetic Theory (EMTS2019), San Diego, CA, USA, May 27-31 2019: described in Chapter 5.

Related publications

- Proceedings of international conference (Refereed)
  - O. Sakai, G. Itami, T. Akiyama and Y. Harada, "Two-Dimensional Metamaterial for Surface Wave Propagation with Scanning Metallic Defect for Permittivity Imaging", International Symposium on Electromagnetic Theory (EMTS2013), Hiroshima, Japan, May 20-24 2013: related to Chapter 4.
  - G. Itami, T. Akiyama, O. Sakai and Y. Harada, "Localized electromagnetic distortion in 2D metal hole array and its application to imaging of permittivity distribution", 2014 Asia-Pacific Microwave Conference (APMC2014), Sendai, Japan, November 4-7 2014: related to Chapter 4.
  - G. Itami, Y. Toriumi, and Y. Akiyama, "A Novel Design Method for Miniaturizing FSS Based on Theory of Meta-materials", 2017 International Symposium on Antennas and Propagation (ISAP2017), Phuket, Thailand, October 30- November 2 2017: related to Chapter 6.
  - G. Itami, Y. Toriumi, and J. Kato, "The Angular Stability of a Minituarized Frequency Selective Surface Wi-Fi Protection Shield", 2018 Asia-Pacific Microwave Conference (APMC2018), Kyoto, Japan, November 6-9 2018: related to Chapter 6.
- Abstract of international conference
  - G. Itami, T. Iizuka, Y. Toriumi, J. Kato and O. Sakai, "Direction-of-Arrival Estimation Method Using Scattering Patterns Formed by Subwavelength Periodic Structures of Conductive Scatterers", Joint International Symposium on Electromagnetic Compatibility and Asia-Pacific International Symposium on Electromagnetic Compatibility (EMCSapporo

and APEMC2019), Sapporo, Japan, June 3-7 2019: related to Chapter 5.

Acknowledgments

I would like to acknowledge sincerely all the people listed below who are remarkable for establishment of this work.

First, I would like to express my highest gratitude to Professor O. Sakai at The University of Shiga Prefecture for encouraging me to engaged in this work and discussing how academic researches should be.

I am very grateful to Y. Akiyama, Project Manager, Network Technology Laboratories, Nippon Telegraph and Telephone Corporation (NTT), who guided the direction of my work in the company (included in Chapter 5 and 6).

I would like to thank J. Kato, Group Leader, Network Technology Laboratories, NTT who supported and encouraged me to conduct this work.

I wish to express my gratitude to Y. Toriumi, Senior Researcher, Network Technology Laboratories, NTT who supported this work and discussed how practical researches should be.

I also wish to express my gratitude to the members of EMC Technology Group at NTT, especially my colleagues of F. Mahmood, N. Arai and T. Iizuka.

I would like to thank the members of Plasma Science and Engineering Laboratories at Kyoto University, especially my colleagues of Y. Nishio, A. Iwai, N. Kihara, Specially Appointed Researcher K. Saito, and Secretary R. Nakanishi.

This work was supported in part by a Grant-in-Aid for Scientific Research from the Japanese Ministry of Education, Culture, Sports, Science and Technology, Japan (JSPS KAKENHI Grant Numbers JP18H03690 and JP18K18756) and was partly funded by Project for Kyoto Bio-industry Creation and Support.